Analysis of tremor at the San Andreas Fault at Parkfield

Zur Erlangung des akademischen Grades eines
DOKTORS DER NATURWISSENSCHAFTEN
von der Fakultät für Physik des
Karlsruher Instituts für Technologie (KIT)

genehmigte

DISSERTATION

von

Dipl.-Geophys. Tobias Horstmann
aus Leimen

Tag der mündlichen Prüfung:	25. Oktober 2013
Referent:	Prof. Dr. Friedemann Wenzel
Korreferent:	Prof. Dr. Thomas Bohlen
Korreferentin:	Asst. Prof. Dr. Rebecca M. Harrington

"*The poetry of the earth is never dead.*"

John Keats (1795-1821)

Abstract

Along plate boundaries, major earthquakes cause repeatedly high damage, and sadly, human losses. Moreover, recent major earthquakes illustrate the social and economical importance of seismic hazard analyses and risk mitigation, which require, among other things, detailed information on the underlying structure of the earth crust. The analysis of seismic observations leads to knowledge about faults and stresses within the earth's crust, however, only the determination of earthquake source mechanisms can reveal information within the seismogenic zone of the crust, limiting what is known about the deep crust.

Recent observations suggest that non-volcanic tremor occurs in the transition zone between the seismogenic zone, and the creeping asthenosphere below. Thus, tremor has the potential to shed light on dynamic regions in the earth crust which have been difficult to study before. The emergent phase arrivals, low amplitude waveforms, and variable event durations make detection and location of tremor a non-trivial task. Due to the difficulties associated with an automated detection of tremor and the need for precise source locations, the present thesis focuses on the detection and localization of tremor.

I employ a new method to identify tremor in large datasets using a semi-automated technique. The method first reduces the data volume with an envelope cross-correlation technique, followed by a Self-Organizing Map (SOM) algorithm to identify and classify event types. The method does not rely on *a priori* information such as event templates and is capable of identifying tremor bursts of variable duration, assuming some variation in tremor amplitude within the length of the noise window (420 sec). Moreover, the sensitivity of the method can be adjusted by a set of normalization factors. I apply the semi-automated detection algorithm to a newly acquired data set of waveforms from a temporary deployment of 13 seismometers near Cholame, California from May 2010 to July 2011. In the 13-month time period the method detects 2606 tremor events with a cumulative signal duration of nearly 55 hours and in the first three weeks tested detection accuracy of 79.5%.

Furthermore, I present a new tremor localization method based on time-reversal imaging techniques. The modified TRI method searches for phase coherence over a short time period instead of the maximum amplitude of a superpositioned wavefield. The advantage of the modified TRI method is the independence of amplitude and the inclusion of temporal information, making the method more robust. Moreover, in theory the modified TRI method does not rely on any *a priori* information such as phase arrival times given a high enough signal to noise ratio. A synthetic test shows that the modified TRI method is capable of locating a double-couple source and the successful localization of a recorded M 1.4 earthquake indicates a feasible application to real data. However, rebroadcasted S-phase pulses reveal a shift of more than one wavelength at the determined source position, evidencing inaccuracies of the velocity model and causing large uncertainties in the frequency band of 1 - 5 Hz. The uncertainties can be decreased significantly by tapering around the S-phase pulse with a 3 s long cosine taper in the seismogram. In order to locate tremor, I apply the modified TRI method with the tapering technique to a 34 individual LFE events within tremor episodes. To evaluate the calculated source positions I use the stacked LFE family locations by Shelly and Hardebeck (2010) for reference, indicating reasonable individual LFE source locations.

Contents

List of Figures

List of Tables

Abbreviations

ANSS Advanced National Seismic System. 26, 27, 30, 37, 44, 45, 47, 85

BDSN Berkeley Digital Seismic Network. 9, 10, 54

DB index Davies-Bouldin index. 22–25, 34

ETS episodic tremor and slip. 4

FD finite-difference. 52

HRSN Berkeley High Resolution Station Network. 9, 54

JMA Japan Meteorological Agency. 4

KABBA KArlsruhe BroadBand Array. 9–11, 53

LFE low frequency events. 4, 8, 47, 49, 50, 66, 67, 69–84, 86, 87

NCSN Northern California Seismic Network. 10, 54

NVT non-volcanic tremor. 2

PBO Plate Boundary Observatory. 54

PGV peak ground velocity. 27, 44–46

PML perfectly matched layer. 52

PSD power spectral density. 14, 15

SAF San Andreas Fault. 4–6, 83

SAFOD San Andreas Fault Observatory at Depth. 6

SNR signal-to-noise ratio. 1, 3, 4, 30–33, 40, 41, 55–60, 66, 67, 69, 73–77, 80, 82, 83, 85–87

SOM Self-Organzing Map. 10, 11, 13–17, 19–26, 28, 30, 31, 34, 35, 37–40, 44, 45, 47, 86

STA/LTA short term average / long term average. 26–28, 34, 37, 39, 45

TRI time-reversal-imaging. 50, 58–60, 63, 64, 66, 70, 72, 74, 75, 82–84, 86

1. Introduction

Instead of a static entity, the earth is a dynamic system that has been studied for a long time. Mantel convection inside the earth drives plate motion in the earth crust.At the edge of the moving crustal plates, friction induces stress and strain within the crust, which is often released by earthquakes. Along plate boundaries, especially along subduction zones, major earthquakes cause repeatedly high damage, and sadly, human losses. Furthermore, the increasing earth population and the growth of densely populated areas due to urbanization raise seismic risks worldwide, especially close to major fault systems. Some examples of seismic high risk areas include the densely populated area around Cascadia subduction zone, the north Anatolian fault near Istanbul, and the subduction zone beneath Japan. Recent major earthquakes such as the M9.0 Tohoku earthquake in Japan in 2011 and the M7.0 earthquake in Haiti illustrate the social and economical importance of seismic hazard analyses and risk mitigation.

A profound knowledge about the dynamics of an earthquake and detailed information of the underlying structure of the earth crust plays an important role in seismic hazard analyses. With the application of different geophysical methods, geodetic observations, and analyses of in-situ rock samples, scientists have gathered valuable information about the earth structure and developed many dynamic earthquake rupture models. In particular, the analysis of seismic observations lead to knowledge about faults and stresses within the earth crust. However, the determination of earthquake source mechanisms reveal only information within the seismogenic zone of the crust and thus less is known about the deep crust.

The seismogenic zone defines the area in the earth crust, which is capable of initiating earthquakes by brittle failure. Recent observations suggest that a previously unknown phenomena, non-volcanic termor, occur in the transition zone between the seismogenic zone, and the creeping asthenosphere. The recently discovered examples of non-volcanic tremor in subduction zones and deep strike-slip settings occur therefore likely below the seismogenic zone and thus have the potential to shed light on dynamic regions in the earth crust. Tremor is more difficult to study than earthquakes are, because of the low signal-to-noise ratio (SNR). By determining the physical conditions such as the depth, temperature,

mineralogy and metamorphic state in which tremor occurs it may be possible to extract information about the conditions that are essential for tremor and thereby learn about the source process (Rubinstein et al., 2010). Therefore, "from a hazards perspective, near-real time tremor detection and location may serve in forecasting the threat of megathrust earthquakes (Rogers and Dragert, 2003) by inferring the temporal and spatial extent of the possible loading of the seismogenic zone" (Wech and Creager, 2008). Due to the difficulties associated with an automated detection of tremor and the need for precise source locations, the present thesis focuses on the detection and localization of tremor.

The thesis is structured as follows: chapter 1 gives a brief introduction to tremor and the tectonic setting and geology at the San Andreas Fault. Next, I present a new method to identify tremor in large datasets using a semi-automated technique based on neural networks and cross-correlation. The technique and the results are presented in chapter 2, which is based on the publication of Horstmann et al. (2013). In the second half of the thesis, I introduce a modified time reversal imaging technique to locate tremor in chapter 3. Finally, I summarize the main results and give a outlook on future work in chapter 4.

1.1. Tectonic tremor

In contrast to volcanic tremor that has been observed at volcanoes for decades, tremor in subduction zones and strike slip setting is a newly discovered phenomena. In order to distinguish both, such tremor is named as tectonic tremor or non-volcanic tremor (NVT). However, the source of tremor at volcanoes result from fluid transport through cracks and crevices. Non-volcanic tremor is not though to directly result from fluid flow through cracks, because the harmonic signature in the frequency band observed in volcanic tremor is not present in non-volcanic tremor. Thus, non-volcanic tremor is generated by a different source mechanism, which is supported by other evidence (Rubinstein et al., 2010). For the sake of simplicity, I refer in the following to non-volcanic tremor simply as tremor.

Since Obara (2002) first observed tremor along the southwest Japan subduction zone, tremor has been detected in many other subduction zones, such as Cascadia (Rogers and Dragert, 2003; McCausland et al., 2005), Costa Rica (Brown et al., 2009; Walter et al., 2011), Alaska (Peterson and Christensen, 2009) and Mexico (Payero et al., 2008). Many studies have also shown that tremor occurs outside of subduction zones; for example, Nadeau and Dolenc (2005) detected tremor along the San Andreas fault, a transform plate boundary, and Peng and Chao (2008) observed tectonic tremor in Central Range in Taiwan, an arc-continental type collision environment.

The seismic signal of tremor is different than from regular earthquakes, as it is a long -duration, low-amplitude signal with slowly emergent phase arrivals. The lack of distinct body wave arrival phases and easily identifiable features makes it difficult to distinguish it from cultural noise and is only recognized by the common shape of envelopes at widely spaced stations (Brown et al., 2008; Rubinstein et al., 2010). Tremor also differs in the spectral content from regular earthquakes. Compared to local earthquakes tremor has much lower corner frequencies and thus it has often its main energy concentrated around the 2-8 Hz band (Obara, 2002; Schwartz and Rokosky, 2007; Beroza and Ide, 2011; Zhang et al., 2011). Furthermore, the duration of the tremor signal is highly variable. Active

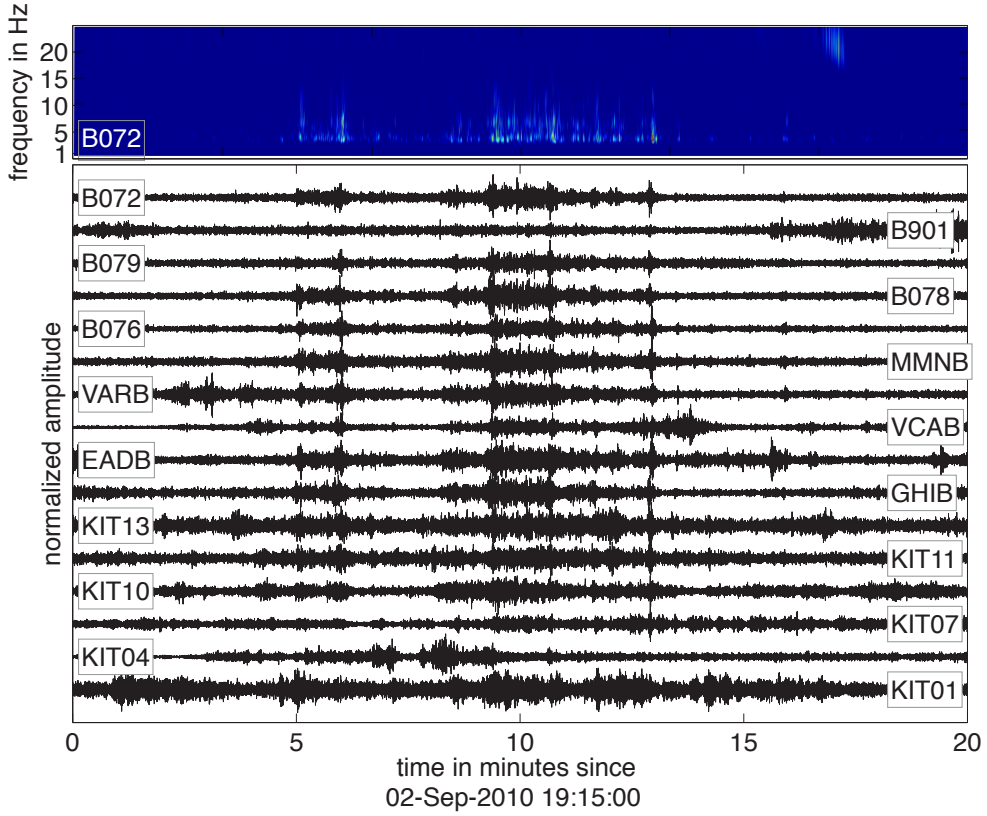

Figure 1.1.: Example of a tremor episode with a good signal-to-noise ratio filtered between 2-8 Hz. The figure shows the north component of 16 recorded seismograms of the KABBA deployment in Cholame. The upper panel shows the spectrogram of the raw seismogram of station B072 in the frequency band of 0.1-25 Hz. Please note the main energy of the tremor signal concentrated in the frequency band of 2-8 Hz.

periods of tremor lasted for a week or more, while individual tremor episodes ranges from short bursts of a few seconds up to several tens of minutes or hours (Obara, 2002; Ryberg et al., 2010; Beroza and Ide, 2011). An example of a tremor episode with a good SNR recorded partially by the KABBA deployment in Cholame shows figure 1.1.

Tremor can occur spontaneously, in which case it is denoted as “ambient“ tremor, or it can be “triggered“, by small stress changes. Triggered tremor can be excited by surface waves of large distant earthquakes or other static or dynamic stress changes such as tidal forces (Ghosh et al., 2009; Gomberg et al., 2008; Peng et al., 2008, 2009; Wang et al., 2013).

Despite the missing distinct body wave phase arrival, tremor is believed to be dominated by shear waves as the propagation velocity is similar to S- waves, which is supported by observations of higher amplitudes on horizontal components and polarization analysis of tremor revealing tremor consisting largely of shear waves (La Rocca et al., 2005; Wech and Creager, 2007; Payero et al., 2008; Miyazawa and Brodsky, 2008).

A remarkable discovery was the observation of low frequency events (LFE) within tremor episodes by Shelly et al. (2006). LFE's are small, slow earthquakes with short duration previously identified by Japan Meteorological Agency (JMA) (Katsumata and Kamaya, 2003; Ide et al., 2007b; Brown et al., 2008). LFE's occur in event families with similar waveforms, indicating that members of an individual family are located in close proximity to each other. Shelly et al. (2007) searched for repeating LFE's in Japan with a systematic cross-correlation-based approach and showed that a significant portion of the tremor seismograms could be explained by multiple occurrences of LFE's. Moreover, the good SNR of the master templates allowed for picking of S-phase and the application of a combination of cross-correlation and double-difference technique to locate event families more precisely than previous studies (Shelly et al., 2006). However, in regions of low amplitude tremor, such as the San Andreas Fault, the master templates have a much lower SNR. Therefore, Shelly and Hardebeck (2010) stacked up to 400 LFE's to obtain P- and S-phase arrivals to locate individual LFE families.

Another interesting observation is the link of tremor to slow slip events (Rogers and Dragert, 2003; Obara et al., 2004). Geodetic observations showed slow slip events, which were accompanied by active tremor episodes and have a semi-regular recurrence intervals of 13-16 months for example in Cascadia, which lead to the term episodic tremor and slip (ETS) for the phenomena (Miller et al., 2002). Furthermore, studies have shown that both tremor and slow slip events are related to shear slip on the plate boundary (Ide et al., 2007a). Slow slip events rupture very slowly and take place over many hours/days, and do not radiate observable seismic energy. Thus, Shelly (2010) suggested that tremor could provide a method to indicate slip that is too small to be detectable geodetically. In fact Smith and Gomberg (2009) find that a fairly large (∼M5) slow slip event below the seismogenic zone on the San Andreas Fault (SAF) near Parkfield would be undetected geodetically.

1.2. Tectonic setting and geology

The SAF defines the plate boundary between the oceanic Pacific plate and the continental North American plate at a length of approximately 1300 km through California, USA. The SAF features a extended fault system with a complex structure and reaches from the Salton Sea in Imperial county in the south to Cape Mendocino in Humboldt county in the north. From the south the SAF system strikes about N.60°W and bends sharply to the east just northwest of Los Angeles to a striking of N.35°-40°W, which is referred to as the Big Bend reach of the fault (Wallace, 1990). The SAF and major faults in California are illustrated in figure 1.2a).

The relative local movement of the oceanic Pacific plate and the continental North American plate is approximately 53mm per year in the southern Gulf of Mexico, from which the SAF accommodates as much as 35 mm per year (DeMets and Dixon, 1999; Loveless and Meade, 2011). Due to the northwest-southeast plate motion direction the SAF is a transform fault with mainly right-lateral strike-slip motion, although individual fault branches feature left-lateral strike-slip motion (e.g. Garlock fault), thrust faulting (e.g. San Fernando fault zone), and even normal faulting is present in some places (Wallace, 1990). Based on the seismicity and other properties, such as the slip rate or the probability of

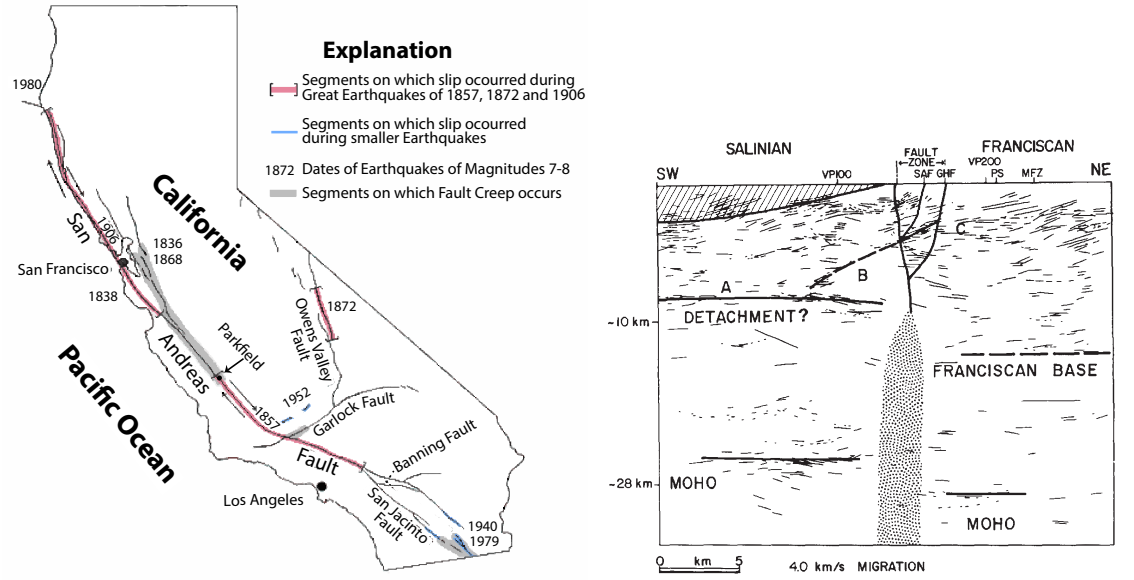

(a) (b)

Figure 1.2.: Geometry of the San Andreas Fault. Figure a) shows the SAF system and major faults in California. Image is taken and modified from Schulz and Wallace (1997). Figure b) was taken from McBride and Brown (1986) and shows seismic reflections across the SAF at the Parkfield segment and their possible interpretation.

major earthquakes, the SAF is divided into different segments (Steinbrugge et al., 1960; Aviles et al., 1987). Reoccurring ruptures of the segments in the past have caused major earthquakes as for example the 1812 $M_W = 7.5$ Wrightwood and 1857 $M_w = 7.9$ Fort Tejon earthquakes (Sieh et al., 1989). Furthermore, paleoseismic studies by Weldon et al. (2004) revealed 14 earthquakes with an average slip of 3.2 m along the central-southern SAF within the past 1500 years with inhomogeneous spatial distribution and recurrance intervals.

The thesis focuses on the region of the SAF around Cholame near Parkfield, which has become well-known by the Parkfield Earthquake Prediction Experiment (Bakun and Lindh, 1985; Kanamori, 2003): moderate-sized earthquakes with M≈6 occurred at the Parkfield segment in 1922, 1934, and 1966 and further studies revealed additional earthquakes in 1857, 1881 and 1901 in the same area. The fairly regular time interval of approximately 22 years and similarities in the pattern of foreshocks in 1934 and 1966 led to the prediction of a moderate-sized earthquake in the area occurring around 1988, which finally happened 16 years later in June, 2004. Despite the failure of the prediction, many interesting results on seismicity, velocity structures, wave propagation characteristics, and fault slip patterns have been obtained from the data of the experiment and today the area around Parkfield is well instrumented.

Parkfield is situated in the 35 km long Cholame valley on a relatively straight section of the SAF with right-lateral strike-slip motion. The Parkfield segment marks the the tran-

sition zone between two segments of the fault and is accompanied by seismic activity (Unsworth et al., 1997). On the one hand, the creeping central segment of the SAF to the north which releases the stress by a constant slip rate of 25-30mm per year at the surface and by a longterm slip rate of 31-35mm per year at depth of the fault (Titus et al., 2005; Rolandone et al., 2008; Tong et al., 2013). Uniquely, the strike-slip motion occurs nearly aseismically as fault creep over a distance of about 170 km. On the other hand, the portion south of Parkfield is locked, and little fault movement or seismicity since the Fort Tejon earthquake in 1857 have been observed at the locked Fort Tejon earthquake segment to the south (Harris and Archuleta, 1988).

The basement bedrock beneath Parkfield is very different on each side of the fault. The Pacific plate in the southwest is composed mainly of oceanic crust. Its basement rock is Salinian granite, which is overlain by Quaternary and Tertiary sediments (Unsworth et al., 1997). On the other side of the SAF to the northeast is the Francisean basement rock, a heterogeneous assemblage that consists largely of dismembered sequences of graywacke, shale, and lesser amounts of mafic volcanic rocks, thin-bedded chert, and rare limestone. The sedimentary and volcanic Francisean rocks were formed in a marine environment and are probably Late Jurassic and Cretaceous in age (Wallace, 1990). A detailed characterization of minerals has been carried out by Solum et al. (2006) on in-situ samples directly from the fault zone at 3 km depths which were obtained at the San Andreas Fault Observatory at Depth (SAFOD). SAFOD is part of the EarthScope initiative (www.earthscope.org) and a borehole was drilled into the hypocentral zone of repeating M≈2 earthquakes on the SAF (Hickman et al., 2004).

Deep seismic reflection analysis by McBride and Brown (1986) revealed a 5km wide and 10 km deep flower structure of the SAF at the surface, shown in figure 1.2b). Furthermore, the crustal thickness confined by the Moho discontinuity is determined for the Parkfield area between a depth of 25 km and 30 km (McBride and Brown, 1986). The absence of coherent reflectors suggests a zone of heavily fractured material in the fault zone (Unsworth et al., 1997). Moreover, a direct evidence for a fractured low velocity zones provides fault-zone guided waves within a wedge of low seismic velocity material along the fault (Li et al., 1990; Lewis and Ben-Zion, 2010).

The different geological units at both sides of the fault and the damaged rock in the fault zone differ in their properties, which impacts to the seismic wave propagation velocities. Moreover, anisotropy in the the crust of the Parkfield segment has been observed, influencing the wave propagation as well (Cochran et al., 2006; Liu et al., 2008).

The SAF is nearly vertical strike-slip fault and both, shallow seismicity as well as tremor below the seismogenic zone of the fault, accommodate shear displacement. In the present work, I account for the velocity contrasts across the fault by using a 3D velocity model of Thurber et al. (2006), particular at the localization of tremor in chapter 3.

2. Tremor detection

2.1. Introduction to tremor detection

The emergent phase arrivals and low amplitudes make automated tremor detection a difficult task. In attempts to overcome difficulties associated with detection, a variety of detection methods have been developed, many of which are based on one of two techniques: 1) a cross-correlation of envelope waveforms (Obara, 2002) or 2) searching for low-frequency earthquakes (LFEs) (Katsumata and Kamaya, 2003). Additional techniques which do not rely on cross-correlation of envelopes or templates include those used by Brudzinski and Allen (2007), Ghosh et al. (2009) and Walter et al. (2011).

Three of the most common methods include a method by Brudzinski and Allen (2007) based on an increase of the mean amplitude values, a method by Wech and Creager (2008) analyzing network coherence with envelope cross-correlation, and a method by Shelly et al. (2007) which uses a template matching, cross-correlation technique. Brudzinski and Allen (2007) use the mean amplitude values of filtered data as an indicator for tremor activity. They calculate a time series of the mean value of continuous waveform envelopes on an hourly basis. The time series is restricted to data recorded during the night hours in order to avoid high amplitude cultural noise. They neglect time windows with a high ratio between the maximum and mean values in order to reduce the influence of large noise transients. After applying a moving average and normalizing the time series, peaks in the time series are identified as tremor. The method is computationally efficient and can therefore be performed rapidly on large datasets without requiring a dense network of stations. However, the disadvantage of their method is that the amplitude of tremor activity must be significantly higher than the recorded noise, and must increase the mean amplitude envelope over a timespan of one hour in order to be detected.

In contrast to the single station method by Brudzinski and Allen (2007), Wech and Creager (2008) introduced a method analyzing network coherence through epicentral reliability and spatial repeatability. They first calculate envelope functions for 5-minute time windows that are low-pass filtered between 1 and 8 Hz. Next, they use a grid search over

all possible source locations based on S-wave lag times calculated from the correlation values of the envelope functions. Source locations with estimated epicentral error estimates exceeding 5 km are rejected. Tremor activity is then detected when at least 2 locations occur within a 0.1 x 0.1 degree area per day. The advantage of the method is its ability to detect and locate tremor at the same time, and that it provides robust results even when an individual station has a poor signal-to-noise ratio. A limitation of the method is that it is restricted to detection of extended tremor episodes.

Shelly et al. (2007) introduced a different detection method using LFEs in combination with a template matching, cross-correlation technique. The set of LFEs from a number of different event families function as master templates in the detection algorithm which then identifies tremor events in continuous waveform data. The advantages of the method are that it is very precise in event time determination and it can be applied using individual stations. The shortcoming of the method is the required *a priori* knowledge of the master event templates which restricts detection to LFEs which correlate highly with the defined templates. Brown et al. (2008) modified the LFE template technique to overcome the disadvantage of requiring *a priori* knowledge of the master templates by eliminating the requirement that master templates be predefined. They remove the need for using predefined master templates by applying a running auto-correlation technique to identify the event families and average the repeating events to create master templates. However, the method is computationally expensive and thus difficult to apply to large datasets.

Here I introduce a new method using a neural network algorithm based on frequency content and motion products of tremor waveforms. The fundamental advance of the method is that it does not rely on master templates and is not based on any assumptions about a minimum signal length. Many tremor detection methods employ a minimum time window length, limiting event detection to those tremor episodes with duration exceeding the minimum window length (e.g., Wech and Creager (2008)). Removing such restrictions on duration permits the detection of a wider range of event types than present methods, thereby increasing the potential for discovering tremor at different depths within the fault zone. Detecting tremor at shallow depths, particularly in subduction zones, could have potential implications for seismic and tsunami hazard; therefore, methods capable of detecting a wider variety of events have the potential to advance our understanding the role of tremor in fault slip. By detecting a larger variety of events, I increase the observations available for analysis and interpretation, and advance our understanding of tremor sources. Here, I describe a new method for tremor detection, while the detailed analysis of the tremor will be the subject of forthcoming work. The method detects tremor in an automated fashion, however, calibration of the method is required for use with a specific data set, so I refer to the method as "semi-automated."

The chapter is structured as follows: I first present the data set and methods description in sections 2.2 and 2.3, followed by a method performance evaluation in section 2.4 using a three-week test data set. Finally, I apply the method to over one year of continuously recorded waveform data to identify all tremor events within that time span.

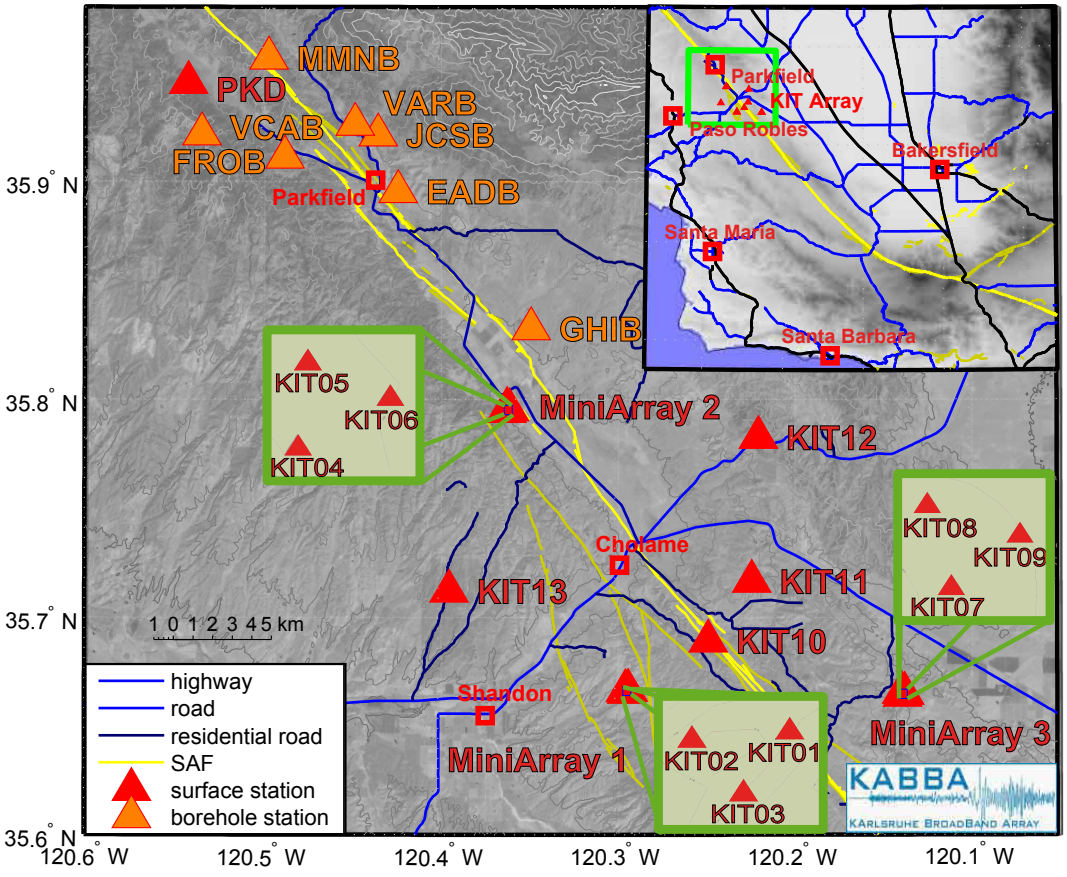

Figure 2.1.: Station distribution used in my analysis, including the temporary KABBA array, the permanent HRSN stations, and station PKD. Three sites contain a mini-array of three stations each, spaced approximately 150 m apart.

2.2. Dataset

The data set consists of continuous broadband recordings of 13 STS-2 seismometers from the KArlsruhe BroadBand Array (KABBA) at a sampling rate of 200 sps. The surface stations were deployed along the Cholame segment of the San Andreas fault at seven sites within a 20 km by 25 km area centered on the town of Cholame (figure 2.1). The highest amplitude tremor identified in previous studies occurs directly beneath Cholame (Nadeau and Guilhem, 2009; Shelly and Hardebeck, 2010; Ryberg et al., 2010). In contrast to the area around Parkfield, the area near Cholame lacks dense station coverage. The KABBA array was designed to supplement the seismic network south of Berkeley High Resolution Station Network (HRSN) to better record the vigorous tremor occurring here. The station installation at three of the seven sites consist of mini-arrays of three stations each spaced approximately 150 meters apart. The stations recorded continuously from May 2010 to July 2011. In addition to the KABBA broadband surface stations, I use seven borehole stations from the HRSN and one additional broadband surface station from the Berkeley Digital Seismic Network (BDSN). The HRSN stations GHIB, EADB, FROB, VCAB, VARB,

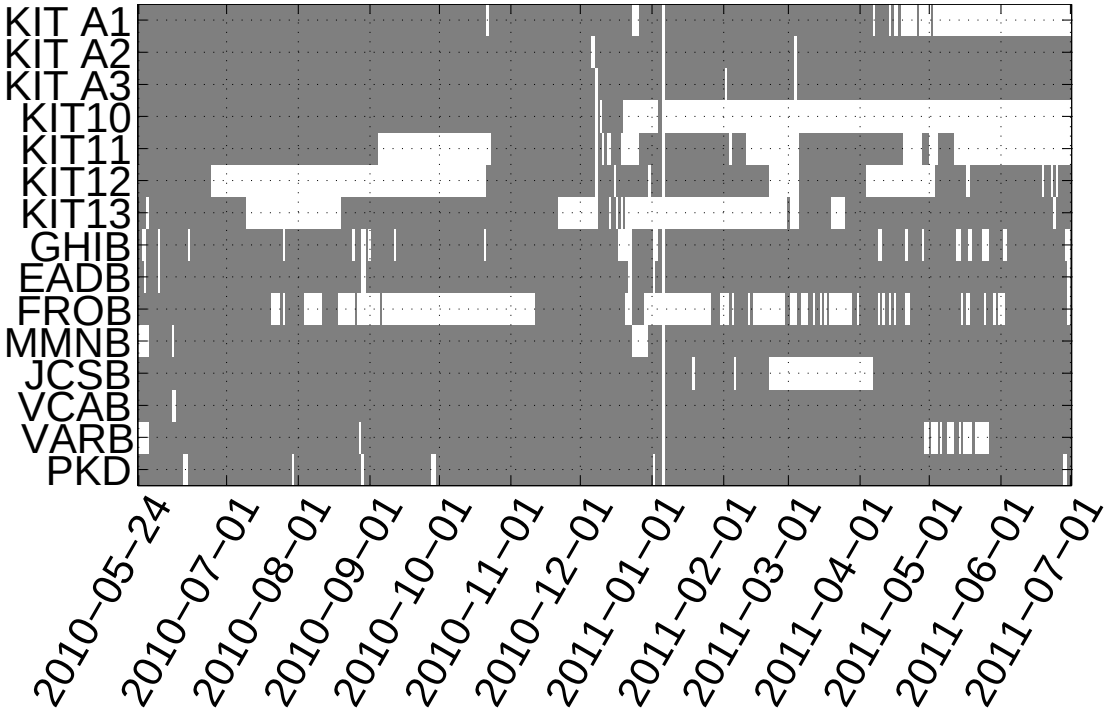

Figure 2.2.: Data availability for the complete data set. White space denotes missing data or data with malfunctioning components, while time periods marked in gray are used in the analysis.

MMNB and JCSB are located north of the KABBA broadband array near Parkfield and record at a sampling rate of 250 sps. Station PKD of the BDSN network is also located north of the KABBA array, and records continuous data at a sampling rate of 100 sps. Additional data exists from Northern California Seismic Network (NCSN) surface stations however, I do not use them, as selected stations provide us with the widest range of azimuthal coverage using the least number of stations possible in order to optimize the computational efficiency. A complete list of stations is provided in table 2.1 and an overview of the data availability is shown in figure 2.2.

2.3. Methods

In this section, I outline the individual steps of the semi-automated detection method. I first detail the data reduction step which reduces the volume of continuously recorded data (section 2.3.1) to enhance the computational performance. Second, I describe the data classification steps required to prepare the data input for the neural network, or Self-Organzing Map (SOM) clustering algorithm (section 2.3.2). Next, I present the SOM clustering, including the determination of the signal classes (section 2.3.3). Finally, I describe the post-processing steps that reduce the number of earthquakes and false picks in the signal classes, which may occur if the adjustable sensitivity of the algorithm is set to be high (section 2.3.4).

Station	Latitude (deg. N)	Longitude (deg. W)	Elevation	start date	end date
KIT A1	35.665945	-120.293227	510m	24-May-2010	02-May-2011
KIT A2	35.795039	-120.360526	375m	24-May-2010	31-Jun-2011
KIT A3	35.664648	-120.137173	387m	24-May-2010	31-Jun-2011
KIT10	35.688881	-120.247177	599m	24-May-2010	05-Jan-2011
KIT11	35.716370	-120.222643	619m	24-May-2010	11-May-2011
KIT12	35.782349	-120.218689	581m	25-May-2010	31-Jun-2011
KIT13	35.711880	-120.393730	448m	24-May-2010	31-Jun-2011
GHIB	35.832249	-120.347282	330m	24-May-2010	31-Jun-2011
EADB	35.895222	-120.422623	224m	24-May-2010	31-Jun-2011
FROB	35.910950	-120.486877	231m	24-May-2010	31-Jun-2011
MMNB	35.956501	-120.496002	480m	29-May-2010	31-Jun-2011
JCSB	35.921169	-120.433998	299m	24-May-2010	31-Jun-2011
VCAB	35.921619	-120.533920	555m	24-May-2010	31-Jun-2011
VARB	35.926079	-120.447052	177m	29-May-2010	31-Jun-2011
PKD	35.945171	-120.541603	583m	24-May-2010	31-Jun-2011

Table 2.1.: Complete list of stations, their positions, and data availability.

2.3.1. Data reduction

Our dataset contains roughly 14 months of continuous recordings on a maximum of 21 stations, including both the temporary KABBA array and permanent stations. The goal of the data reduction step is to keep time periods with potential seismic events while reducing the data volume as much as possible. In the following, the term 'seismic event' refers to both tremor and earthquakes, which are assumed to be of unknown type until they are classified by the method. The data reduction step uses a cross-correlation technique similar to that applied by previous studies; however, here the cross-correlation is not designed to detect or classify seismic events exclusively. Instead, portions of a continuous time series are classified using the SOM clustering.

I start by searching for time windows containing coherent signals across the station array. I first filter the waveforms between 2 and 8 Hz, as the signal to noise ratio for tectonic tremor for my dataset is highest in the 2-8 Hz band (Obara, 2002; Schwartz and Rokosky, 2007; Beroza and Ide, 2011). Second, the envelope of each trace is calculated and decimated to 0.2 sps, following which, the envelopes of individual components are stacked for each station. Third, I perform a cross-correlation of waveform envelopes between each station and a designated master station. The cross-correlation step is repeated using each station once as a master station. I do not remove the instrument response, as it is flat within the frequency band of interest and, removing it would increase the computational time. Moreover all cross-correlations are normalized and based on smoothed envelopes, which removes the influence of different amplitudes and reducing the effect of phase shifts. I tested different time window lengths and the time step to determine the most effective time window length. A trial-and-error comparison of hand-picked time windows and time windows picked by the automated method indicates that a 520 second window

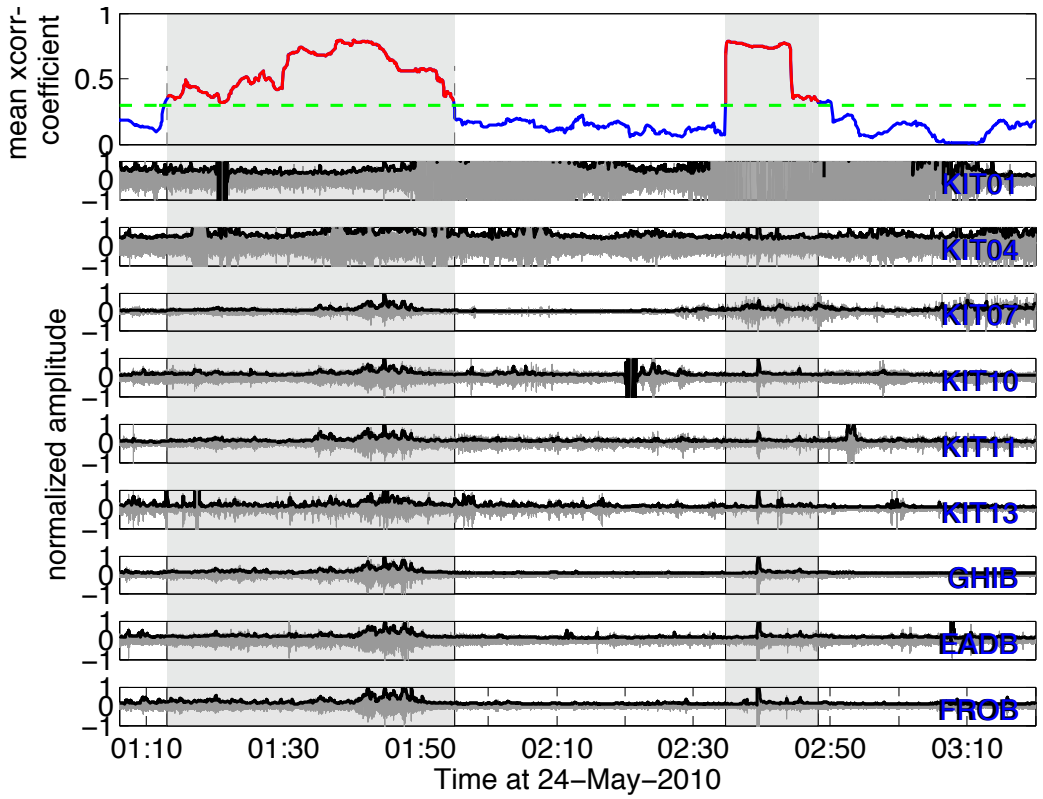

Figure 2.3.: Example of the data reduction step: top panel shows the mean cross correlation coefficient of the envelope cross-correlation for a 2 hour period on the 24th of May, 2010. The green dashed line denotes the threshold value. Cross-correlation values above the threshold value are indicated in red, and determined retained time windows shown as gray boxes. The bottom panels show the normalized waveforms filtered between 2 Hz and 8 Hz and the normalized envelopes.

and 5 second time step optimally removes noise while retaining the highest number of the seismic events. The inter-station distance divided by a speed of 3 km/s is the maximum permitted time lag between peak correlation values, reducing the influence of infrasound events and noise while still detecting S-waves from shallow sources close to the stations. After averaging the cross-correlation values for each time window and each master station over all station pairs, I then select the maximum mean cross-correlation value, producing a mean coefficient function over time. I retain event windows for which the coefficient function exceeds the mean correlation value by a threshold of 0.1 for at least 30 seconds. The threshold was determined by testing values on a a one-week test data set from 24th of May to 14th of June, 2010. I determine by visual inspection which values retain the majority of events, while best reducing the data volume. I merge windows separated by less than 300 seconds into a single event window. Doing so may preserve extended tremor episodes which may have been otherwise fragmented into separate time windows. Visual examination of the tremor episodes recorded in my data set suggests that tremor episodes

do not typically last longer than approximately 100 seconds, hence I use a generous value of 300 seconds to bridge time windows. One could use a longer inter-window time, however, doing so increases the cost of computational time during the SOM processing.

Figure 2.3 shows exemplary a 2 hour time period on the 24th of May, 2010, visualizing the data reduction step. The bottom panels show the filtered waveforms and the envelopes. The top panel shows the mean cross-correlation coefficient and indicates the threshold value with a green dashed line. The retained time windows are marked as gray boxes.

2.3.2. Data preparation

The data preparation steps outlined here prepare the data for input into the Self Organized Map (SOM) algorithm (Kohonen, 2001), which is available as a Matlab toolbox (Vesanto, 2000). The data preparation is not essential to the clustering algorithm, but is included to enhance the detection algorithm's performance, including adjusting the sensitivity of the algorithm. The goal of the SOM is to group time series data with distinguishing features. The SOM algorithm may use any similar feature, such as frequency content in a particular band or polarity, to classify the data. The larger the feature differences between various types of signals, the more effectively they distinguish those signals. Below, I describe the pre-conditioning steps and the feature selection and calculation. The main data pre-conditioning steps entail reducing the effects of noise and calculating and normalizing the feature values used by the SOM algorithm. I first describe the noise reduction in section 2.3.2.1, followed by trace alignment in section 2.3.2.2. I then explain the feature calculation in section 2.3.2.3 and, finally, I describe the feature vector normalization in section 2.3.2.4.

2.3.2.1. Noise Reduction

To remove the influence of noise and to enhance signal amplitudes for the feature calculation, I implement a noise reduction technique introduced by Martin (2001), which is based on minimum statistics and employs spectral subtraction methods. The noise reduction step improves the detection result, thereby increasing the sensitivity of the detection algorithm. The technique assumes that the power spectral density of a given signal quickly decays to the background noise level over time. It tracks the minimum spectral amplitude value in a moving time window larger than the signal length and in narrow frequency bands, using the tracked values as an estimated minimum noise level. A mean noise level estimation is then calculated by multiplying the minimum noise estimation with a bias compensating factor, which is based on the variance of the spectral amplitude in that given frequency band (Martin, 1994). Assuming that noise and signal are statistically independent and additive, one may remove noise by subtracting the mean noise estimation from the original spectra. The phase spectra are not modified, thereby permitting a transformation back to the time domain, with the noise removed.

The algorithm applies a short-time Fourier transform with a moving time window length of 0.6 seconds and 0.3 second overlap in which the power spectra are recursively smoothed. For example, let $M_{k,l}$ denote the power spectrum for a given frequency bin l within some time window k. The smoothed power spectrum is given by $P_{k,l} = \alpha \cdot P_{k-1,l} + (1-\alpha) \cdot M_{k,l}$,

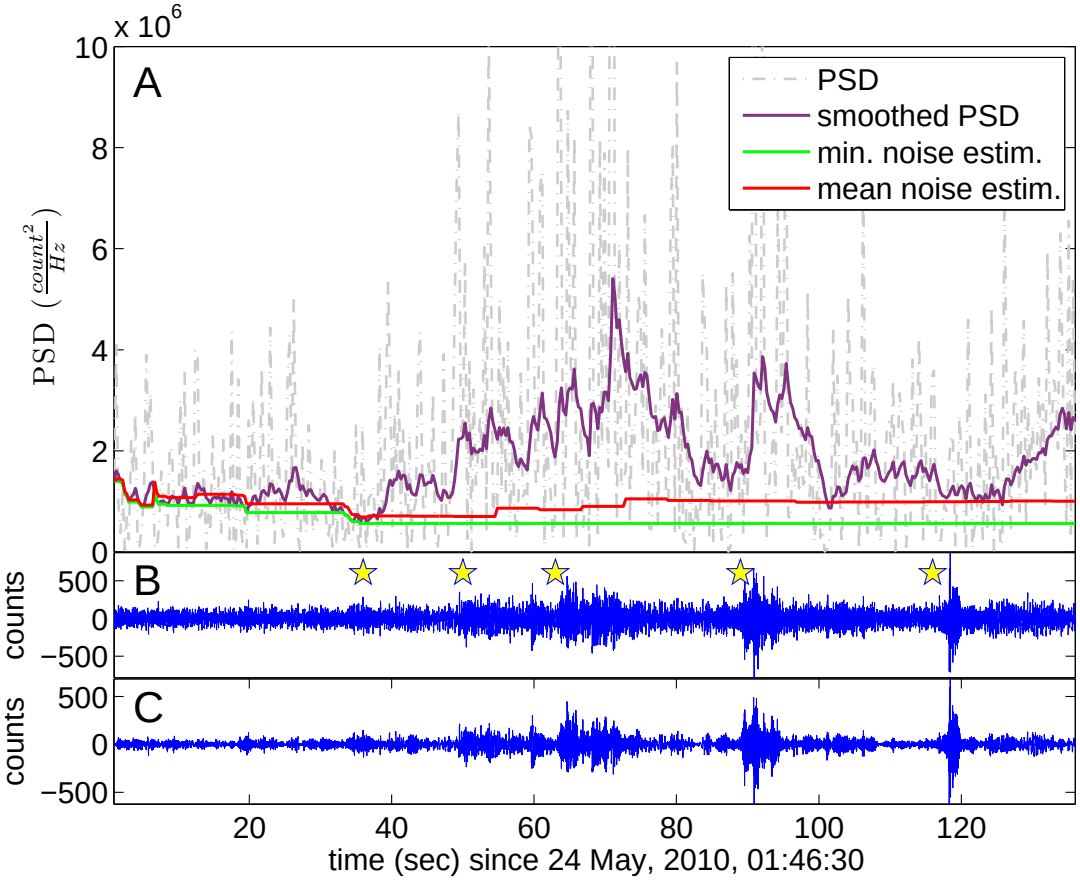

Figure 2.4.: A) Power spectral density (PSD) for one narrow frequency bandpass centered around 7 Hz of the waveform data shown in B (dashed line). Smoothed PSD (purple), tracked minimum value (green), and a bias factor computed mean noise estimation (red). (B) Z-component of station KIT 10 filtered between 2 - 8 Hz during a tremor episode including individual tremor bursts (yellow stars). (C) Noise reduced trace after subtracting the mean noise estimation. The trace in C has lower noise amplitudes than the trace in B, enabling the SOM algorithm to perform better.

where α represents an updating factor that controls the influence of previous time windows. The updating factor α is typically set between 0.9 and 0.95 (Martin, 1994). Here, I use a value of 0.9.

A requirement of the noise reduction method is that the time window used to track the minimum noise level must be longer than the expected observed signal (Martin, 1994). Tremor episodes consist of successive energy bursts which may last up to several minutes. The time window for the noise reduction must be larger than the longest observed tremor signal in order to bridge to the next minimum containing only noise. However, the shorter

the time window, the more accurate the estimation of the noise level. I reviewed longer tremor episodes in my test dataset and tested various window lengths and found a maximum of 420 seconds an optimum duration. The disadvantage of using such a long time window becomes apparent when considering cases where the noise level is monotonically increasing. For example, the noise level is calculated for a given sample from the time window spanning 420 seconds prior to the sample. If the noise level constantly increases, the current estimation of the minimum noise level in a given window occurs at the beginning of the window. However, the noise estimation is subtracted from the sample at the end of the time window. Thus, the noise level is underestimated. Consequently, the noise level estimation will be underestimated at a time lag approximately equal to the time window length. However, even in the extreme case of monotonically increasing noise, the noise reduction will reduce the noise amplitude leading to a better signal-to-noise ratio and therefore an enhanced tremor signal.

Figure 2.4 illustrates the functionality of the technique. Panel B shows the original time series recorded at station KIT10 with a 2-8 Hz bandpass filter applied exhibiting multiple tremor bursts. The same tremor bursts highlighted in B are enhanced in C after applying the noise reduction. The enhanced signal will be more easily recognized by the SOM algorithm. Note that the power spectral density (PSD) shown in figure 2.4 reflects a narrow frequency band centered at 7 Hz. Therefore, some tremor bursts which are not obvious in the PSD can be seen in the waveforms in B and C.

2.3.2.2. Trace alignment

The goal of the SOM algorithm is to cluster specific data features independent of the signal duration. Specifically, I want to be able to detect short tremor bursts, as well as longer episodes. Therefore, in order to cluster features of the same signal recorded at individual stations, all traces must be corrected for moveout. I calculate an individual moveout correction for each of the time windows retained by the data reduction step discussed in section 2.3.1. I then align traces according to the moveout before inputting them into the SOM. I determine the moveout between station pairs by cross-correlating envelopes that have been smoothed over 15 samples with a master station.

In order to allow greater flexibility and account for the current noise conditions at the individual stations, any of the stations may serve as the master station. I determine the moveout used to align the traces from the offset associated with the maximum of the cross-correlation function. Preliminary inspection of the data showed a number of infrasound events (see example in section 2.4.1, figure 2.14, as well as a discussion of the feature calculation of infrasound events). Setting a maximum permissible time difference allows us to remove infrasound events with much lower propagation velocities, while retaining most other seismic events. For each time window, I choose the master station for which the envelope correlation coefficients are on average higher than the other stations.

2.3.2.3. Feature Calculation

Once I prepare the data for input into the SOM by reducing the effects of noise and aligning the traces, I calculate the features on which the event detection is based. Any characteristic of a time series which varies with signal source is well-suited for use in

SOM clustering. Such characteristics may include: polarity, frequency-wavenumber, and complex seismic trace properties. I term such particular characteristics as “features" after Köhler et al. (2010), and calculate multiple feature values continuously throughout the time series. I combine all feature values into a feature vector for each window where the feature values are calculated. For an extended discussion on features, including various types and their interdependence, I refer the reader to Köhler et al. (2010).

Determining what features work best for a given data set requires testing the features for uniqueness using a sample data set. I perform a preliminary test of the SOM algorithm on a three-week long sample data set that contains both tremor and earthquakes. The sample data set was taken from the beginning of the measurement period, spanning the period from 24th of May to 14th of June, 2010. I use waveforms from the temporary deployment, as well as from permanent stations installed locally near the Parkfield segment of the San Andreas fault (table 2.1). The sample data set contains noise, tremor events, and local and regional earthquakes, and is therefore suited for testing the method. In the subsequent text, I refer to the three-week long test data set discussed here as simply the test data set. Example tremor events are shown in figures 2.11 and 2.12, and an example earthquake recording is shown in figure 2.13. Systematic tests using various features of tremor episodes indicate that two features are capable and sufficient to distinguish tremor signals from regional earthquakes and noise: 1) spectral amplitudes in five narrow frequency bands calculated via a Stockwell transform (Stockwell et al., 1996), and 2) combined horizontal to vertical component motion products (Jepsen and Kennett, 1990).

The five frequency bands used for the first feature include the main energy band of tremor, namely the 2-8 Hz band, as well as the 15-30 Hz and 0.5-1.5 Hz bands. The 2-8 Hz band is subdivided into three equally sized bands. The 15-30 Hz band is useful for distinguishing tremor from noise, and the 0.5-1.5 Hz band is useful for discriminating tremor from regional and teleseismic earthquakes. The high-resolution spectral amplitudes are calculated using a Stockwell transform and then averaged over the given frequency bins (Stockwell et al., 1996). The Stockwell transform produces the time-frequency distribution of a signal using a moving Gaussian window that is scalable for different frequencies. Compared to a short-time Fourier transform, the Stockwell transform retains better time resolution, similar to wavelet transformations.

The second feature I calculate consists of combined motion products. Combined motion product values differ widely for different seismic phases; thus, they are ideal for use within the SOM algorithm. White (1964) defined two motion product detectors, HV and HiV having a 90° phase shift:

$$P_N = u_N \cdot u_D \qquad P_E = u_E \cdot u_D \qquad (HV) \tag{2.1}$$

$$Q_N = H(u_N) \cdot u_D \qquad Q_E = H(u_E) \cdot u_D \qquad (HiV) \tag{2.2}$$

where u_N, u_E and u_D are the displacements in the North, East and vertical directions. $H(u_N)$ denotes the Hilbert transform of u_N. Jepsen and Kennett (1990) used both HV and HiV detectors to define combined motion products:

$$P_{NE} = \sqrt{P_N^2 + P_E^2} \qquad \text{and} \qquad Q_{NE} = \sqrt{Q_N^2 + Q_E^2}. \tag{2.3}$$

They define a wave classification parameter PQ_{abs} using the combined motion products, where $PQ_{abs} = P_{NE} * abs(Q_{NE})$. For a rectilinear polarized wavefield, PQ_{abs} is used to discriminate between vertically and horizontally polarized S-waves, with expected PQ_{abs} values of > 0.25 and < 0.25, respectively. Waves with 2-dimensional motion, such as Love or Rayleigh waves, are expected to have PQ_{abs} values greater than 0.25. The PQ_{abs} parameter exhibits large increases during earthquake and tremor episodes, while maintaining low values for noise. PQ_{abs} is therefore a useful parameter for distinguishing seismic events from noise. I also use it to distinguish the clusters identified by the SOM algorithm containing seismic signals, which I discuss in detail in section 2.3.3.1.

As discussed above, I use five frequency bands for the spectral density calculation and one combined motion product, for a total of six values per time interval, per station. I first decimate the time series to 50 sps after applying a lowpass filter with a 20 Hz corner frequency to avoid aliasing effects. I then calculate the six feature values at the sample rate of the decimated time series, with the exception of the upper frequency. The upper frequency band feature is calculated from the time series decimated to 100 sps, which then has a lowpass filter applied with a corner at 40 Hz. The decimated and filtered time series of the upper frequency band is also resampled to 50 sps. I then create feature vectors for an individual station by taking the average value of each feature over 0.5 second time intervals, in order to optimize the balance between computational cost and accuracy. The feature vectors from each individual station are combined into a single feature vector for the entire array. For example, a feature vector would consist of 60 feature values per time interval for a 10 station array.

2.3.2.4. Feature vector normalization

The input for the SOM algorithm is the feature vectors. The SOM clustering algorithm is based on Euclidean distances of the feature values comprising the feature vectors in a high-dimensional parameter space (Vesanto and Alhoniemi, 2000). In order to weight all features equally, it is critical to normalize all feature values to the same range, i.e., between 0 and 1. I use an extended softmax normalization to normalize feature values.

The softmax normalization is defined as

$$X_{norm} = \frac{1}{1 + e^{-X_{scaled}}} \quad \text{, with} \quad X_{scaled} = \frac{X_{org} - \text{mean}(X_{org})}{\text{std}(X_{org})}, \tag{2.4}$$

where X_{org} are the original feature values (Pyle, 1999, pp. 271-274, 355-359). The main benefits of the softmax normalization over a standard normalization are the ability to reduce the influence of extreme values without neglecting them and regulate the detection sensitivity of the method. By inserting two scaling factors within the softmax normalization, I can define the extended softmax normalization as follows:

$$X_{norm} = \frac{1}{1 + e^{-X_{scaled}}} \quad \text{with} \quad X_{scaled} = \frac{X_{org} - F_{mean} \cdot \text{mean}(X_{org})}{F_{std} \cdot \text{std}(X_{org})}, \tag{2.5}$$

where F_{mean} and F_{std} are the scaling factors that determine the range of the scaled feature values. Adjusting the F_{mean} and F_{std} parameters are what allows one to adjust the

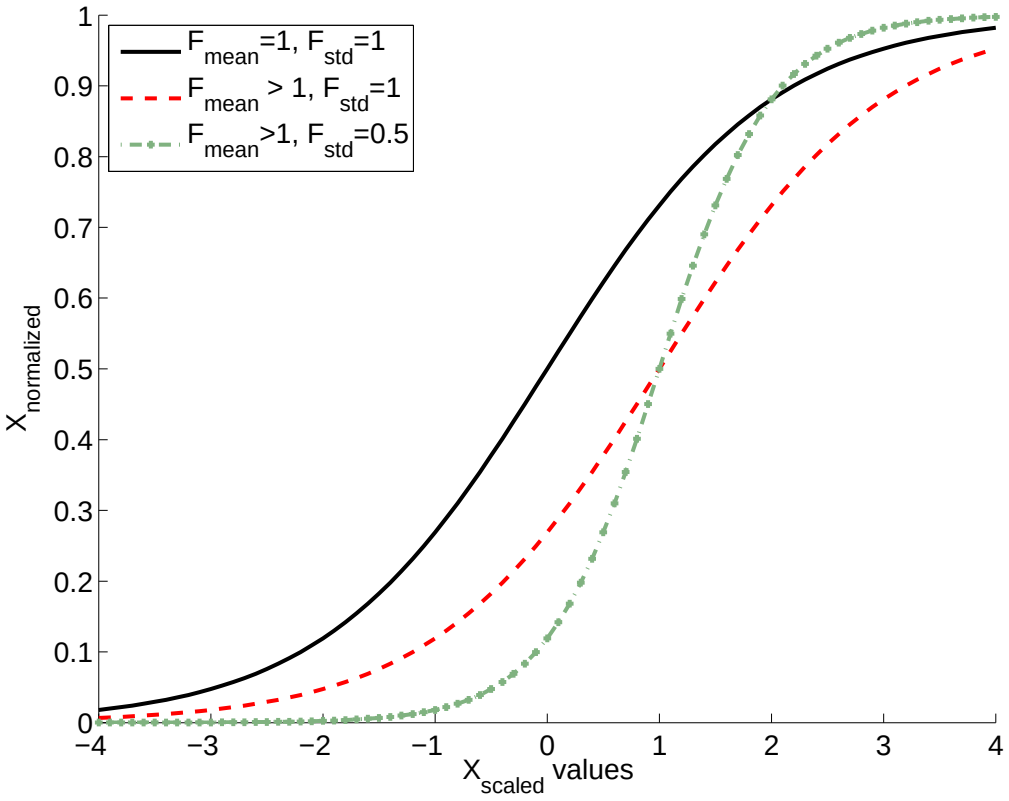

Figure 2.5.: Graphic description of extended softmax normalization: transformation from X_{scale} to X_{norm}: a) Solid line: original softmax normalization; b) dashed line: $F_{mean} * mean(X_{org}) = 1$ and $F_{std} = 1$; c) dashed dotted line: $F_{mean} * mean(X_{org}) = 1$ and $F_{std} = 0.5$.

sensitivity of the detection algorithm for a given a dataset. The scaling factors F_{mean} and F_{std} influence the transformation behavior of the data set to a normalized data space, and can be used to carve out small but important differences which would be lost using the standard softmax normalization. At the same time, bigger, yet less important differences in the data values can be down-weighted.

Our dataset contains over one year of data, making calculating the mean and standard deviation of X_{org} for all feature vectors for the entire time period computationally expensive. Nevertheless, applying the same normalization to the entire data set is critical in order to cluster events that may occur widely spaced in time during the study period. As one does not know the range of feature values *a priori*, the F_{mean} and F_{std} scaling factors must be determined empirically using a sample data set. I therefore calibrate my algorithm using the same three-week representative test data set used for the feature selection in section 2.3.2.3. I calculate the mean (mean(X_{org})) and standard deviation (std(X_{org})) of the feature values for the three-week time period, and use those values to normalize the entire data set. I manually pick tremor events during the three-week period and determine the best F_{mean} value based on a comparison of manually picked events and those picked by

the SOM. I start by normalizing my data set with a range of F_{mean} and F_{std} values and run the SOM for each of the F-value pairs. I evaluate which of the F-value pairs corresponds to the highest number of accurately picked events compared to the hand-picked events. The F-values deemed best from the comparison are then used for the entire dataset, assuming similar characteristics amongst earthquakes and tremor over the entire time period.

Figure 2.5 illustrates the normalization. If the factors F_{mean} and F_{std} are set to one for the regular softmax normalization (black line), the normalization scales nearly linearly for values close to the mean value, and tapers off asymptotically to zero and one for values far from the mean. The portion of the curve that scales linearly is controlled by the standard deviation scaling factor, F_{std}. When $F_{std} \neq 1$, as in the case of the extended softmax transformation, then the curvature of the non-linear region scales asymptotically to both zero and one. The factor F_{mean} is used to shift the linearly-scaled region of the normalized data to the position in the feature dataset where it best discriminates between noise and seismic signals. Increasing the F_{mean} value has the effect of offsetting the scaled data to a value above zero; in the case of the red and green curves shown in figure 2.5, the inflection point of the curves are shifted to a value of one. The most important benefit of using the extended softmax normalization is the capability to regulate the sensitivity of the detection method via the scaling factors F_{mean} and F_{std}. Higher or lower values for F_{mean} and F_{std} translate to higher or lower detection sensitivity. One must keep in mind, however, that with increased sensitivity comes an increased number of false detections. Given their importance, section 2.3.2.5 contains an extended discussion on the determination of F-values. Table 2.2 indicates the optimal values for my data set to achieve the desired level of sensitivity.

feature	F_{mean}	F_{std}
2-4 Hz frequency band	0.5	0.5
4-6 Hz frequency band	0.5	0.5
6-8 Hz frequency band	0.5	0.5
15-30 Hz frequency band	8.0	1.5
0.5-1.5 Hz frequency band	2.5	1
PQ_{abs}	1.8	0.6

Table 2.2.: F_{mean} and F_{std} values determined by a comparison of manually and SOM detected events for the test data set. The values shown are the normalization values used for the remaining data set in the extended softmax normalization (equation 2.5.)

2.3.2.5. Normalization factor determination

In section 2.3.2.4 I introduce the extended softmax normalization, where I briefly discuss the possibility of shifting the range of linear normalization to the optimal position in the feature dataset for discriminating between noise and different seismic signals. One can change the range of linear normalization by changing the F_{mean} and F_{std} factors. Here, I discuss determining the F_{mean} and F_{std} values in greater detail. The optimal F-values are not known *a priori*, because the range of feature values is not known *a priori*, requiring manual determination or in other words a calibration of the method for a certain dataset.

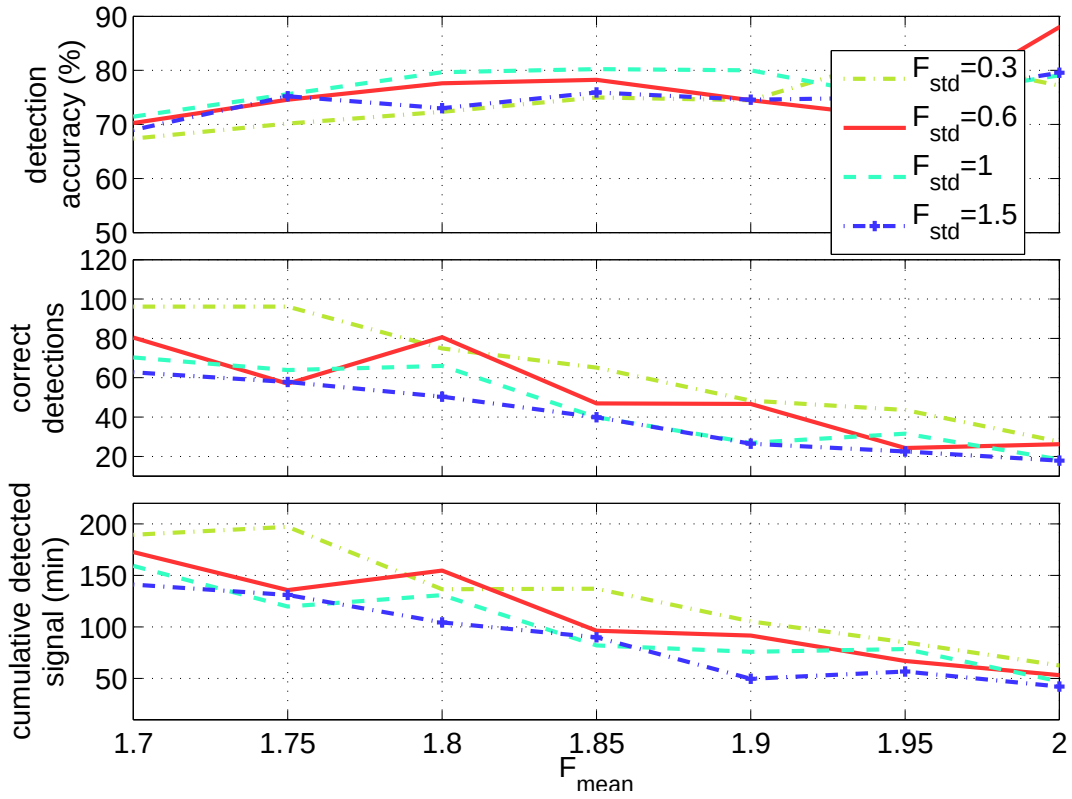

Figure 2.6.: Normalization factor values for PQ_{abs} feature. The color coding corresponds to the F_{std} values shown in the legend.

As mentioned in section 2.3.2.4, I use a test dataset containing three weeks of seismograms with multiple tremor episodes, in order to determine the optimal F-values. I start by comparing manually picked time windows with SOM picked time windows to determine a measure of the detection accuracy. I repeat the process and detection accuracy estimation, each time changing the F-value pairs, while performing a grid search of the best F-values for an individual feature. The values corresponding to the highest accuracy empirically determine the values for F_{mean} and F_{std}.

I face a trade-off between detection accuracy and sensitivity. Figure 2.6 shows the SOM performance for various F_{mean} and F_{std} values for the PQ_{abs} feature value normalization. By choosing a lower F_{mean} value, the number of correctly detected signals increases, as does the number of incorrectly detected signals. As a result, the detection accuracy is lower than for higher F_{mean} values. The grid search depicted in figure 2.6 shows that values of $F_{mean} = 1.8$ and $F_{mean} = 0.6$ provide an optimal balance between sensitivity and accuracy. Table 2.2 summarizes the values for other features. Table 2.3 shows the calculated mean and standard deviation values used in the extended softmax normalization in equation 2.5 for each station and feature.

feature	2-8 Hz		15-30 Hz		0.5-1.5 Hz		PQ_{abs}	
value	F_{mean}	F_{std}	F_{mean}	F_{std}	F_{mean}	F_{std}	F_{mean}	F_{std}
KIT A1	3.17	17.08	4.69	27.08	5.44	7.39	9.85	7.27
KIT A2	5.68	21.88	2.47	20.03	11.08	29.03	10.93	7.80
KIT A3	2.98	9.57	6.66	18.05	2.59	7.66	9.42	7.56
KIT10	1.90	6.70	1.62	3.98	6.70	6.06	9.29	6.10
KIT11	1.47	4.83	0.53	1.09	2.72	2.69	7.14	5.73
KIT12	0.78	1.53	10.46	24.99	1.31	1.39	6.76	6.12
KIT13	2.84	12.51	4.12	12.06	6.81	7.01	9.54	6.83
GHIB	7.08	19.49	1.13	2.65	4.47	4.70	12.22	7.99
EADB	3.21	8.75	1.14	2.41	3.62	3.15	10.95	7.53
FROB	3.54	15.55	1.57	7.57	3.87	3.90	9.97	7.52
MMNB	2.26	10.35	0.97	2.77	5.18	4.94	8.94	6.87
JCSB	1.82	8.66	1.05	3.55	0.53	0.50	8.24	5.26
VCAB	8.33	31.35	5.74	25.71	5.46	5.17	13.45	9.42
VARB	1.30	6.23	1.07	2.05	0.53	0.88	6.88	5.42
PKD	0.73	3.29	0.26	0.69	3.72	3.28	4.02	4.73

Table 2.3.: F_{mean} and F_{std} values used in the extended softmax normalization for each feature and station (in equation 2.5). KIT A1, A2, and A3 represent the mini-arrays for stations KIT01 - KIT09.

2.3.3. SOM clustering algorithm

Following feature normalization, the feature vectors are ready for input into the SOM clustering program (Vesanto, 2000). The SOM is an unsupervised learning method that clusters data into groups with similar feature values. Following feature input, the algorithm first determines the number m of so-called prototype vectors in an N-dimensional parameter space with the heuristic formula (Vesanto, 2000)

$$m = 5 \cdot \sqrt{X}, \tag{2.6}$$

where N is the number of feature values for each time window (e.g., the number of components comprising the feature vectors for an individual station) and X the number of feature vectors $\vec{x}_i (i = 1, ..., X)$. The prototype vectors $\vec{m}_n (n = 1, ..., m)$ form a two-dimensional grid with a hexagonal structure, where each prototype vector has the same dimension as each of the feature vectors, and is connected to the six nearest neighboring vectors. After the grid is randomly initialized in the parameter space, the algorithm updates the prototype vectors and moves them toward the feature vectors during an iterative training period. I use the *batch* training mode (Vesanto, 2000), in which the prototype vectors in each learning step t are moved based on the equation

$$\vec{m}_n(t+1) = \frac{\sum_{j=1}^{n} h_{cm}(t)\vec{x_j}}{\sum_{j=1}^{n} h_{cm}(t)}. \tag{2.7}$$

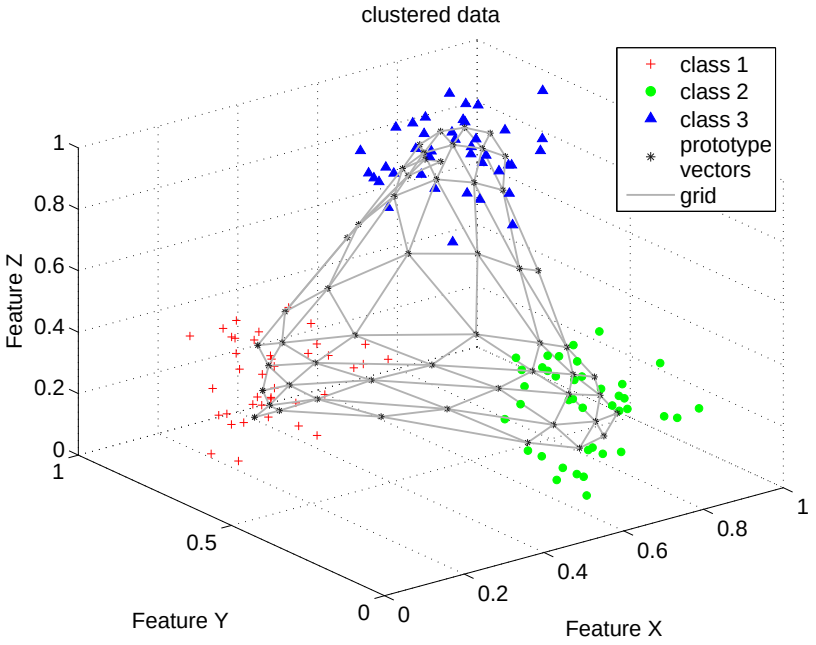

Figure 2.7.: SOM after training: The SOM can be seen as a regular two-dimensional grid of prototype vectors (black stars connected by a mesh) initialized in a 3-D data space in this example. Red, blue and green points represents the data set. Each component of an individual data vector (shown here as X, Y, and Z) represents a feature. The color code of the data points indicates the clustering result.

The Gaussian neighborhood function $h_{cm}(t)$ can be expressed by

$$h_{cm}(t) = \exp^{-d_{cn}^2/2\sigma_t^2}, \tag{2.8}$$

where σ_t^2 denotes the neighborhood radius at learning step t and $d_{cn} = ||r_c - r_n||$ is the 2D distance between the prototype vectors m_n and m_c on the map grid. The term m_c denotes the prototype vector to which the feature vector x_j is linked. At the end of the training period, the grid is spread to the data cloud. The data cloud is composed of the feature vectors, and it approximates the probability density function of the input data. This process is also known as vector quantization (Köhler et al., 2010). Once the grid position in the parameter space has been calculated, each data point is linked to the nearest prototype vector. I illustrate an example of a dataset with three features in figure 2.7. Data (feature values) are shown by the colored dots, the prototype vectors as black stars, and the grid is indicated by black lines. Following the grid formation, a hierarchical clustering algorithm clusters the SOM prototype vectors (Vesanto and Alhoniemi, 2000). The algorithm iteratively determines appropriate clusters based on the average distances between prototype vectors within existing clusters; however, the user may set an acceptable minimum and maximum number of clusters. The optimal number of clusters is then chosen by evaluating the Davies-Bouldin index (DB index) introduced by Davies and Bouldin (1979). The DB index is a metric for evaluating the appropriate number of clusters based on the dis-

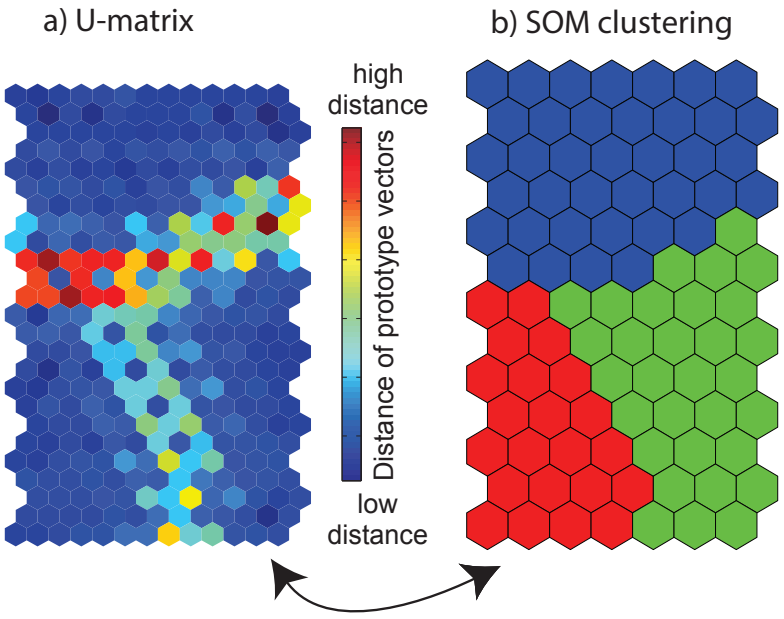

Figure 2.8.: SOM clustering: visualization of the SOM of the data shown in figure 2.7 after training. a) shows the U-matrix with the distance to the neighboring prototype vectors indicated by the color code. Based on the distances of the prototype vectors a hierarchical clustering algorithm determines clusters which are visualized in b). The color code indicates the determined clusters and matches with the color code of the clustered data in figure 2.7.

tance between cluster members, and between cluster centers. For a given number n of clusters, the DB index is calculated by

$$\text{DB index} = \frac{1}{n}\sum_{1}^{n}\max_{j\neq i}\left\{\frac{D_i + D_j}{d_{ij}}\right\}, \tag{2.9}$$

where n is the number of clusters, d_{ij} the distance between cluster centroids i and j, and D the average distance to the cluster centroid. The DB index has a minimum value when the clusters are most compact and widely spaced. All of the above mentioned aspects of the clustering algorithm, including the DB index, are contained within the SOM toolbox as described by Köhler et al. (2009, 2010).

Figure 2.8 visualizes the SOM from figure 2.7 and shows the "unified distance matrix" (U-matrix) and the clustering result. The U-matrix in figure 2.8a represents each prototype vector by seven hexagons and indicates the distance in the data space to each of the six neighboring prototype vectors with the outer hexagons while the seventh hexagon in the middle displays the averaged distance. In this case shown, the DB index determines an optimum of the three clusters. Figure 2.8b shows the cluster composition.

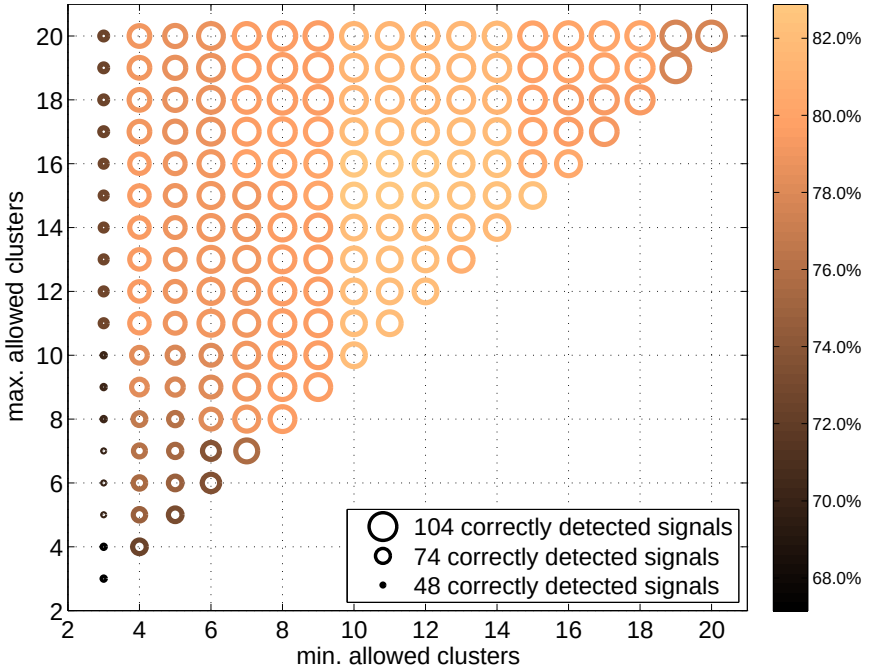

Figure 2.9.: Minimum and maximum number of permitted clusters: circle size corresponds to number of correctly detected events, color code indicates the detection accuracy.

In practice, I restrict the range n for which the DB index is evaluated in order to avoid using an inappropriate number of groups. Based on the number of different signals I expect to be present in the continuous data (noise, tremor, earthquakes, infrasound), I empirically determine the appropriate range of numbers of clusters necessary. I thereby attempt to prevent the algorithm from mixing different signals in one cluster that I want to distinguish. I use the test data set to evaluate the appropriate maximum and minimum number of clusters. Figure 2.9 illustrates the influence of the number of clusters on the detection accuracy, as well as the number of accurate detections found by the SOM in the three-week data set. The detection accuracy varies only marginally ($\pm 2\%$) when the minimum allowed number of clusters is greater than four, and the maximum allowable number of clusters is greater than 8, suggesting that the number of clusters has little influence on the detection accuracy (figure 2.9). The method detects the largest number of events when the minimum number of clusters is 8 or 9. The detection accuracy increases by approximately 1 percent if the minimum number is set to 7 or 10. However, the number of detected signals decreases significantly when the minimum number of clusters is less than 8. One might argue based on figure 2.9 that the best minimum value ranges from 19 to 20. However, analyses of various normalization factor values show a general trend of decreased detection accuracy when using such a high minimum number of clusters. I therefore use 8 as the minimum number of clusters because the SOM detects the largest number of events with a minimum loss in detection and accuracy for the remaining dataset. A similar argument holds for the maximum number of clusters. I choose a

maximum value of 20 to allow greater flexibility in the number of clusters. Therefore, the DB index falls within the range of 8 and 20 clusters.

2.3.3.1. Signal class determination

The SOM groups the data points into clusters, but these clusters do not have an *a priori* association with any particular signal type (e.g. tremor, earthquake, noise). Therefore, the user is free to determine the signal cluster of interest. Here, the algorithm identifies the content of the clusters, and I manually classify the groups of clusters into "classes". I designate three main classes into which the various clusters determined by the SOM are sorted. Two of the classes contain seismic signals, and the third class contains noise. I label these classes as S1, S2, and N (seismic signal classes 1 and 2, and noise). Clusters containing seismic signals are identified by isolating classes with high PQ_{abs} values. The PQ_{abs} feature is able to discriminate between noise and seismic signals for all features values, making it a robust tool for identifying seismic events. Examination of the test data set indicates that normalized $PQ_{abs} \gg 0.5$ for seismic signals, and $PQ_{abs} < 0.5$ for noise signals. I therefore designate a cluster as belonging to one of the two seismic classes if the following two criteria are met: 1) mean $PQ_{abs} \geq 0.5$ at a minimum of three stations and 2) average $PQ_{abs} \geq 0.5$ on all borehole stations. I impose the additional requirement for borehole stations in order to avoid classifying infrasound events as tremor.

I use the frequency features to further group the seismic signals into two classes (S1 and S2). Class S1 contains tremor and small local earthquakes, and class S2 contains regional, and larger local earthquakes. Similar to tremor signals, earthquake signals also have values of $PQ_{abs} > 0.5$. Although the PQ_{abs} feature is similar between the two types of signals, the spectral characteristics of teleseismic and regional earthquakes differ from tremor in the low-frequency band (0.5-1.5 Hz). I identify clusters containing regional and larger local earthquakes using the mean spectral amplitude values in the lower frequency band; events with (normalized) mean spectral amplitude exceeding 0.6 at a minimum of three stations comprise the class S2. The remaining clusters of seismic events comprise class S1 (tremor and local earthquake) class. Unfortunately, the spectral characteristics of small local earthquakes are similar to those of tremor, and there is no definitive cutoff value which can discriminate between the two. Additionally, visual inspection shows similar spectral energy of tremor and local earthquakes in the 10 Hz to 15 Hz band. I initially tried using a feature in the 15-50 Hz band in an attempt to differentiate local earthquakes from tremor. The spectral amplitudes in the 15-50 Hz band also did not differ significantly enough to cluster local earthquakes into separate groups. I therefore use an additional post-processing step to distinguish the small local earthquakes from tremor event in the S1 class (section 2.3.4.1). I describe an estimation of what fraction of the signal grouped into the S1 class is comprised of local earthquake signal in sections 2.4.3.1 and 2.4.3.5.

Finally, I discard all detected time windows less than 4 seconds in length and merge time windows separated by less than 30 seconds in the S1 class. I compile the beginning and end of the resulting time windows in my tremor catalog. Table 2.4 summarizes the criteria used to sort the SOM detected time windows into the three user determined classes.

Class	Class description	mean PQ_{abs}	$0.5 - 1.5$ freq. band
S1	Tremor, small local earthquakes	> 0.5	< 0.6
S2	Earthquakes (large local, regional)	> 0.5	> 0.6
N	Noise	< 0.5	-

Table 2.4.: Criteria used for grouping SOM clusters into the respective classes

2.3.4. Post-processing

Following the SOM clustering and sorting into the S1, S2, and N classes, the S1 class still contains a number of false detections (noise and small local earthquakes). The goal of the post-processing step is to identify false detections and non-tremor seismic signals, and move them into the N and S2 classes respectively. The post-processing step consists of two parts: 1) the first part sorts the earthquakes remaining in the S1 class into the S2 class, and 2) the second part sorts noise (false detections) into the N class. I label the two parts earthquake post-processing and noise post-processing, respectively. The noise post-processing step is optional, and may be implemented depending on the sensitivity set by the user (adjustable via the F_{mean} and F_{std} parameters discussed in section 2.3.2.4).

2.3.4.1. Earthquake post-processing

Because the amplitude/frequency characteristics of small local earthquakes are not dissimilar enough to that of tremor to be discriminating, some local earthquakes are grouped into class S1. The earthquake post-processing step identifies earthquakes in class S1 and moves them into class S2. I first apply a short term average / long term average (STA/LTA) trigger to S1 class time windows that are less than 30 seconds in length to identify impulsive earthquake arrivals. I use a STA/LTA trigger based on the algorithm described by Allen (1982) with a STA-window length of 0.5 seconds and a LTA-window length of 30 seconds. I set the weighting factor C2 from Allen (1982) between the two terms of the characteristic function to 6, and the threshold constant C5 to 5.5. The two terms of the characteristic function are sensitive to changes in amplitude and frequency, respectively, while the C5 constant sets the threshold for event declaration. I apply the algorithm to the Z-component and declare an earthquake when the STA/LTA threshold is reached on at least three stations within a 6-second time window.

The second part of the earthquake post-processing compares the remaining time windows in the S1 class to the ANSS catalog (Advanced National Seismic System, 2012). The detection algorithm presented here does not determine origin times for the detected events; therefore, I compare the results by calculating travel-times from the earthquake epicenter to the center of the KIT array. I estimate the time window in which a cataloged event should occur by calculating upper-bound and lower-bound travel times using a range of seismic velocities between 4.4 and 6.6 km/s. I account for both P- and S-wave velocities for cases where only the S-wave is detected. Additionally, I extend the time window of the expected earthquake by 30 seconds for two purposes: to compensate for uncertainties in the travel path, and to account for the range of arrival times for epicenters which are in close proximity to the array. The range of 4.4 to 6.6 km/s was chosen quasi-empirically (based on realistic values) to maximize earthquake detection by increasing the tolerance

for error in the travel time estimation without making the time windows so large that I might have erroneously included coincidental tremor events. I count an earthquake as detected if it occurs within the calculated time window. I limit the earthquake catalog to the area bounded within the latitude and longitude ranges of 32° N and 38° N, and 123.3° W and 113.3° W. Additionally, I consider only earthquakes with a calculated peak ground velocity (PGV) > 1400 nm/s at the station array. I calculate the PGV following van der Elst and Brodsky (2010), using $\log_{10} PGV = -2.29 + 0.85M - 1.29 \log_{10} r$ where M represents the magnitude and r represents the hypocentral distance in km.

I assume the ANSS catalog is complete for larger earthquakes. And, I apply the STA/LTA detection algorithm to time windows of less than 30 seconds in length to identify small events missing from the catalog. If no catalog information is available, one could apply the STA/LTA trigger to all time windows. The STA/LTA detection alone decreases the correctly classified tremor by approximately 10%, while also increasing the number of earthquakes in the S1 class by approximately 10%. I provide a quantitative assessment of the detection algorithm performance using the earthquake post-processing step in section 2.4.3.5.

2.3.4.2. Noise post-processing

The noise post-processing step moves noise events falsely classified into classes S1 or S2 into class N. The false classification of noise events results from the sensitivity of the algorithm, which can be adjusted via the F_{mean} and F_{std} parameters discussed in section 2.3.2.4. There is an inherent trade-off between accuracy and sensitivity in the detection algorithm, however higher sensitivity enables the detection of more lower amplitude tremor events. For cases where a high sensitivity is desired the optional noise post-processing step detects and removes the majority of false picks, increasing the detection accuracy. The basis for the noise post-processing step is the assumption that events have a similar shape at different stations, while uncorrelated noise bursts do not. Thus, the noise post-processing consists of the following steps: 1) calculating a smoothed envelope for all traces in the time windows selected by the SOM, 2) cross-correlating the envelopes and calculating a mean coefficient of the three best cross-correlation coefficients, and 3) discarding time windows with an average coefficient below 0.8.

I implement additional steps to determine the time window for which the envelope correlation is calculated to account for possible misalignment of traces. In detail, I extend first the detected time window by two percent of the time window length at the beginning and end. To account for short time windows, I also add three seconds at the beginning and end of each signal. The extension is necessary as sometimes the detected time windows are only fraction of an extended tremor signal.

Second, I calculate the envelopes within the extended time windows for each Z-component trace, and smooth the envelopes with a window of 0.6 percent of the time window length.

Third, I calculate the cross-correlation coefficient between all combinations of envelopes, using each station once as a master station. I permit a 4-second time-lag between the envelopes in the cross-correlation. The 4-second time lag is meant to account for cases where alignment between traces is incorrect. An example of where signal misalignment could occur is at a noisy station or where multiple events in short succession are recorded

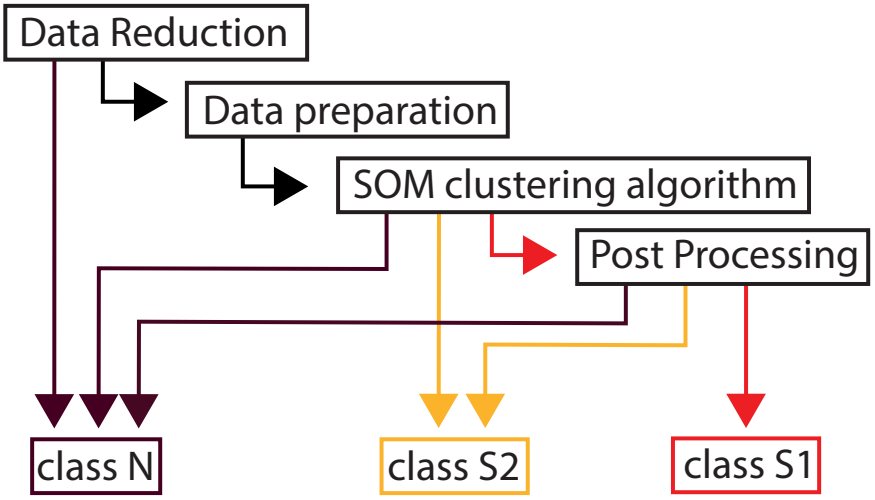

Figure 2.10.: Flow chart of the method: neglected data within the reduction step in section 2.3.1 are sorted in the noise class N, while potential signals are kept and prepared in section 2.3.2, which entail the noise reduction, alignment of traces and the feature calculation and normalization. Then, the remaining data gets classified into the three classes within the SOM clustering algorithm in section 2.3.3. Afterwards, the optional post processing step in section 2.3.4 is sorting out misclassified tremor to the earthquake class with a STA/LTA trigger and noise to the class N with the help of an envelope cross-correlation.

at various source-station geometries. The alignment described in section 2.3.2.2 is then sensitive to the bigger event with the higher amplitudes leading to a larger moveout for other events contained within the same window.

After calculating the cross-correlation values, I average the three highest cross-correlation coefficients for each master station and select the highest average cross-correlation coefficient for each detected time window. Whether or not the noise post-processing step accepts or rejects an event is based only on three station values, i.e., the minimum number of stations required for event detection. Finally, I neglect time windows with an average cross-correlation value below 0.8.

All parameter values described in section 2.3 are summarized in table 2.5 and figure 2.10 provides a flow chart of the method.

Data reduction (section 2.3.1)	
Filter bandpass	2 Hz - 8 Hz
Data decimation	0.2 sps
Cross-correlation time window length	520 s
Cross-correlation time window step	5 s
Cross-correlation max. lag	interstation distance / 3 $\frac{km}{s}$
Correlation coefficient threshold	0.1
Signal merging period	300 s
Noise reduction (section 2.3.2.1)	
Fourier transform time window length	0.6 s
Fourier transform time window step	0.3 s
Smoothing factor α	0.9
Minimum tracking time window length	420 s
Trace alignment (section 2.3.2.2)	
Envelope smoothing	15 samples
Cross-correlation max. lag	interstation distance / 3 $\frac{km}{s}$
Feature calculation (section 2.3.2.3)	
Data decimation	50 sps
Time window length for feature averaging	0.5 s
SOM clustering algorithm (section 2.3.3)	
Minimum number of clusters	8
Maximum number of clusters	20
Signal class determination (section 2.3.3.1)	
PQ_{abs} threshold	0.5
Amplitude threshold for the 0.5 Hz - 1.5 Hz band	0.6
Minimum station number	3
EQ post-processing (section 2.3.4.1)	
STA-window length	0.5 s
LTA-window length	30 s
C2	6
C5	5.5
Minimum station number with detections	3
Time window length for connecting detections at different stations	6 s
Time window extension	30 s
PGV threshold	1400 nm/s
Noise post-processing (section 2.3.4.2)	
Cross-correlation value averaging	3 best stations
Mean cross-correlation value threshold	0.8

Table 2.5.: Summary of parameter settings of the method discussed in section 2.3 (specific sub-sections are listed in the headers of the left column).

2.4. Results

In this section, I evaluate the performance of the tremor detection algorithm using test data set referenced in section 2.3 to determine the best parameter settings. I first discuss three examples of detected waveforms in order to illustrate the capabilities and limitations of the method (section 2.4.1) and visualize the SOM exemplary for the data of 24th of May, 2010 (section 2.4.2). Next, I present tremor and earthquake detection statistics, including correct, false, and missed detections (section 2.4.3.1). I find that the method detects tremor reliably for a signal-to-noise ratio (SNR) >3, and performs optimally when at least 10 stations are used (section 2.4.3.3). Additionally, to evaluate the method's effectiveness, I compare the performance of my method to an implementation of Wech and Creager (2008) method (section 2.4.3.2). Furthermore, a comparison of the earthquake detections with the ANSS catalog gives a detection accuracy of approximately 90% (section 2.4.3.5). Finally, I show in section 2.4.4 that the method detects 2606 tremor events (spanning over 55 hours) within the 14-month data collection period.

2.4.1. Tremor waveforms

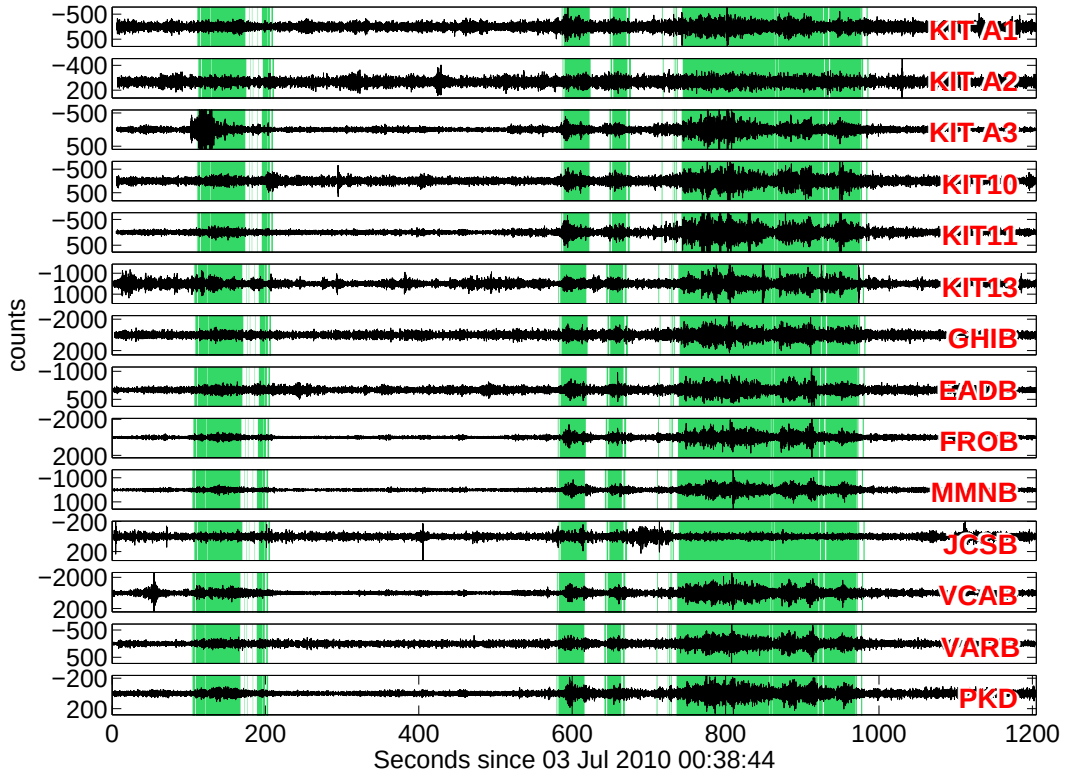

Figure 2.11.: Example of a tremor episode exhibiting a good signal-to-noise ratio. Detected tremor is shown in green, and noise is shown in white.

Although tremor waveforms share characteristics, such as a long-duration (seconds to tens of minutes) and a lack of distinct phase arrivals, individual tremor episodes vary greatly in their appearance (e.g., duration, number of high amplitude pulses or tremor

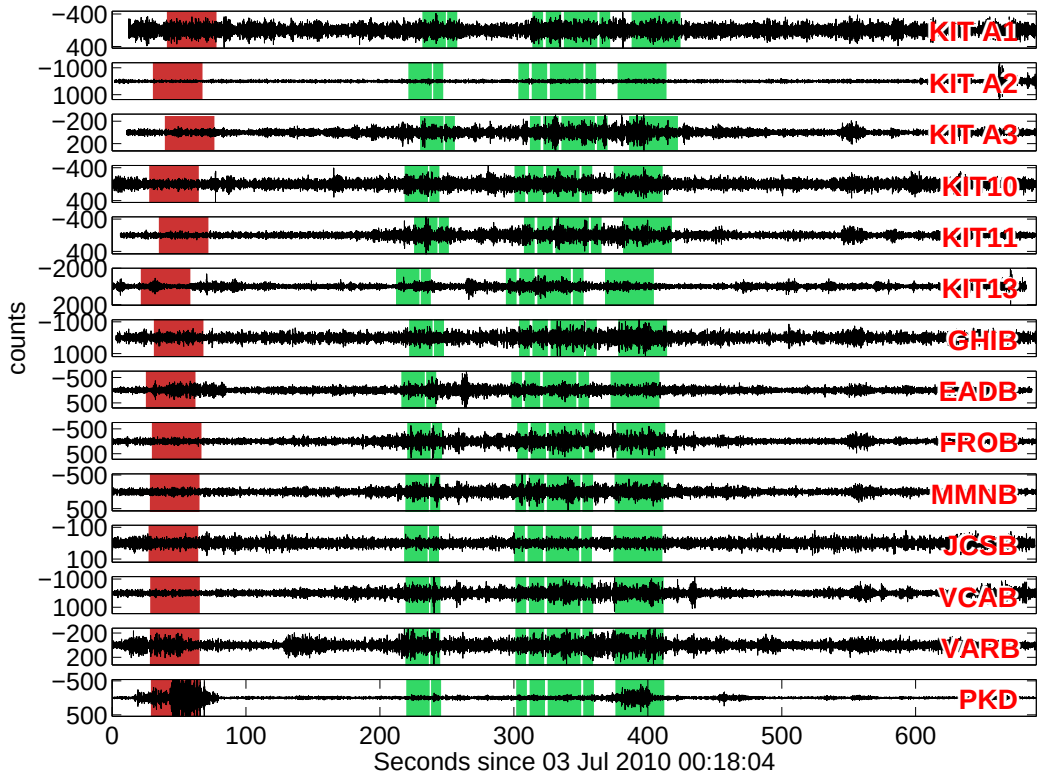

Figure 2.12.: Example tremor waveforms with low signal to noise ratio. The figure illustrates the performance of the SOM clustering algorithm at the SNR detection threshold. Due to local noise conditions, tremor is often only visible on a subset of stations. Data are filtered between 2 - 8 Hz. Color code indicates the clustering result following the post-processing step: detected tremor (green), noise (white), and tremor detected by the SOM and rejected by the noise post-processing step (red). The color coded clustering result is shifted in time at different stations illustrating the trace alignment determined by the algorithm. The unusual moveout for KIT A1, A2, and A3 shows the failing of the trace alignment step, although the method still detects the tremor. A probable event at 570 seconds is not detected, likely due to erroneous moveout correction within the trace alignment step.

bursts, maximum amplitude, etc.). In this section, I show three examples of detected tremor waveforms as well as an earthquake and infrasound event to illustrate the capabilities and limitations of the method.

Figure 2.11 shows an example waveform from 3rd of July, 2010, filtered between 2 and 8 Hz. Time windows highlighted in green indicate windows designated as tremor and white indicates background noise. The tremor episode between 750 to 980 seconds has a median SNR of ∼3 based on root-mean-square (RMS) value in contrast to the much lower amplitude tremor around 180 seconds (SNR of ∼1.5). The SOM method does not provide estimates of source location; however, the detection method of Wech and Creager

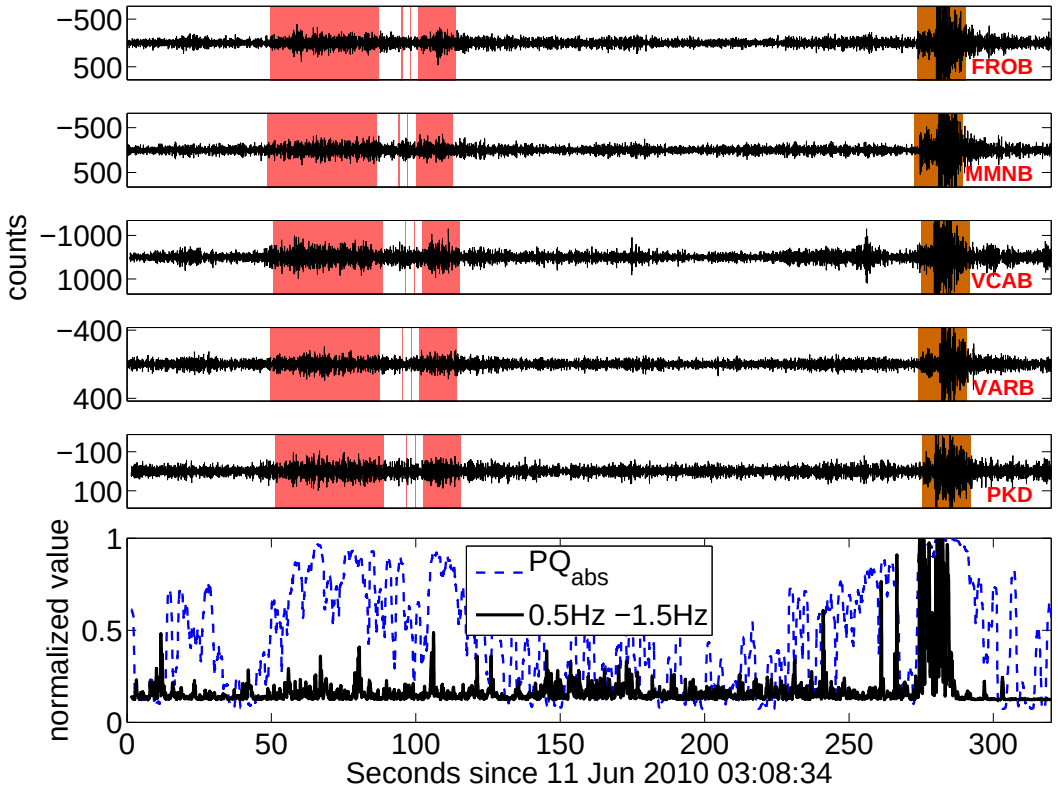

Figure 2.13.: Example tremor waveforms with low signal to noise ratio followed by a small earthquake. Data are filtered between 2 and 8 Hz. Color code indicates the clustering result following the post-processing step: detected tremor (red), earthquake (yellow), and noise (white). The bottom panel shows the normalized feature values for the PQ_{abs} feature and the lower frequency band for station PKD.

(2008) provides an estimate of tremor locations. For the episode shown in figure 2.11, the average epicentral location is $35.64°N \pm 0.30°$, $120.59°W \pm 1.07°$, with a depth of 19.16 km $\pm$ 13.54 km. The event location had horizontal errors on the order of 30 km. The epicentral location is outside the boundary of figure 2.1, and is therefore not shown.

Given my emphasis on greater detection sensitivity (i.e., a higher number of detections) in my current algorithm settings, I also obtain a number of false detections. The tremor signal shown in figure 2.12 has a low SNR of ∼1.8, and is difficult to recognize even by visual inspection. Figure 2.12 illustrates the performance of the method near the detection threshold. Both figures 2.11 and 2.12 show waveforms where the detected tremor bursts are not obvious on all stations, often due to local noise; All traces are shown to illustrate the performance of the method even if noisy data are present. The post-processing step (correctly) rejects the first time window originally identified as a tremor event (highlighted in red), while retaining the remaining tremor windows highlighted in green. Furthermore,

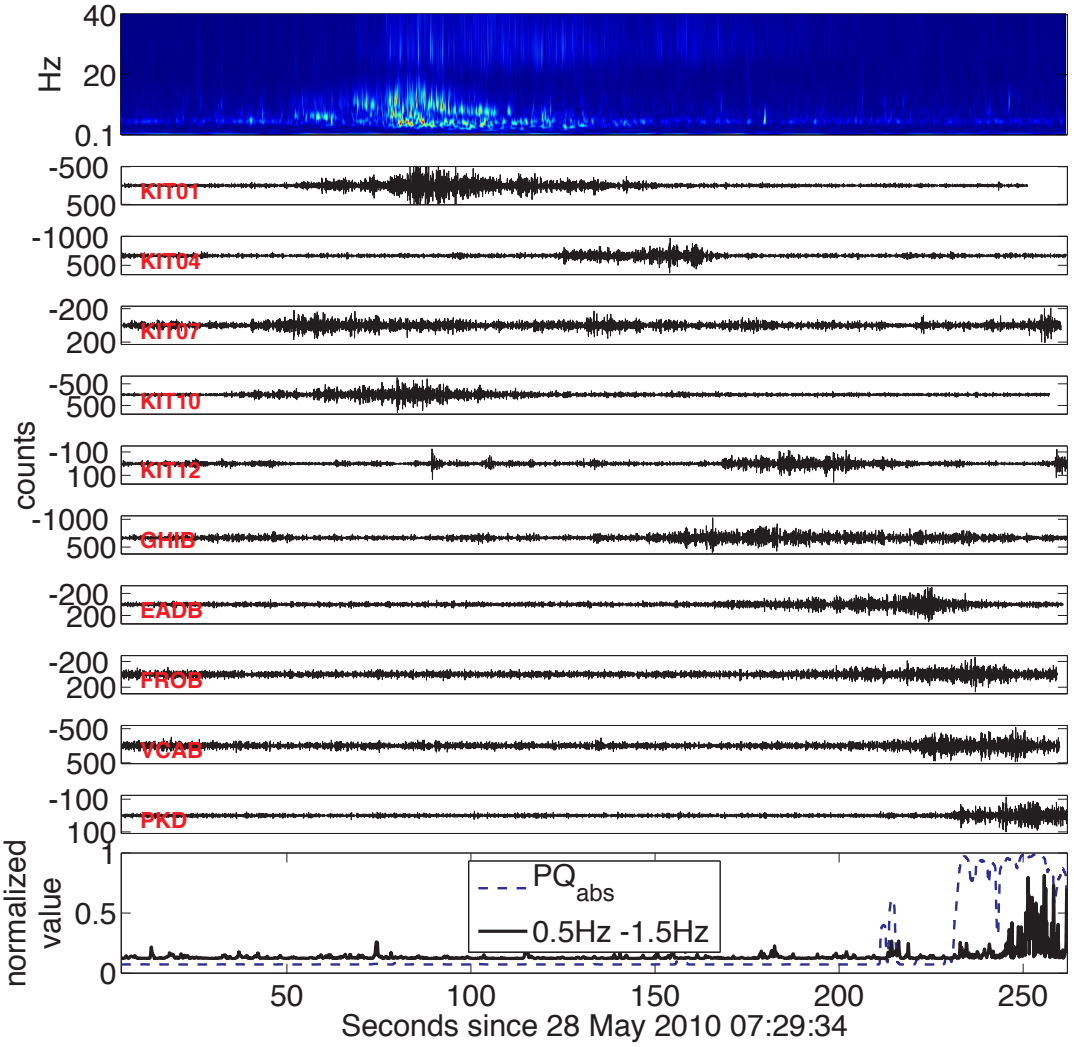

Figure 2.14.: Example infrasound event waveforms, filtered between 2 and 8 Hz. White background color indicates the classification as noise as the clustering result. The top panel displays a spectogram of the raw waveforms recorded at station KIT 01, showing most infrasound energy concentrated between 1-10 Hz. The bottom panel shows the normalized feature values for the PQ_{abs} feature and the lower frequency band for station PKD. Note the large move-out between the stations.

the algorithm misses a probable tremor event around 570 seconds, likely due to misaligned traces. Figure 2.11 and 2.12 show time shifted traces to illustrate the trace alignment determined by the algorithm. Misaligned traces could occur at a station with a low SNR or where multiple events occur in short succession. Either case would lead to different

moveouts within the same time window.

In addition to the previous two tremor waveform examples, figure 2.13 displays a low signal to noise tremor signal as well as a detected earthquake. The upper panels in figure 2.13 show the waveform data, filtered between 2 Hz and 8 Hz for selected stations. The bottom panel documents the normalized values for the PQ_{abs} feature and the lower frequency value between 0.5 Hz and 1.5 Hz. During the seismic events, the PQ_{abs} feature values are increased, while the lower frequency band values are only increased during the earthquake. The difference in the normalized amplitude in the lower frequency band is used by the SOM to distinguish between tremor and earthquakes, although, in this particular example the earthquake was classified by the STA/LTA trigger in the post-processing step.

Figure 2.14 shows an example of an infrasound event to illustrate the misclassification problematic. The bottom panel documents the increase of the PQ_{abs} feature values during the infrasound wavetrain, which leads the SOM to misclassify infrasound events as tremor. The large move-out between the stations indicates the low propagation speed in air.

2.4.2. SOM clustering

A strength of the SOM is its ability to visualize the data of a high dimensional data space, since the topology of the data is preserved by the trained map. As described in section 2.3.3 the SOM consists of prototype vectors, which approximates the probability density function of the input data after the training process. Thus, the distances between the prototype vectors allow insight into the composition of the input data and the clustering process.

Data analysis occurs on a daily basis, therefore a SOM is trained and clustered for each 24-hour time period. This section describes the SOM clustering analysis for the 24th of May, 2010 which is the first day of the dataset and concludes the tremor example in figure 2.12.

Figure 2.15a shows the U-matrix of the trained SOM. The color code shows the distances between each prototype vector and the neighboring 6 prototype vectors. The reddish color indicates a separation of the input data within the multidimensional parameter space and thus possible cluster boarders. The hierarchical cluster algorithm separates the data in up to 20 different clusters, which are analyzed by the Davies-Bouldin index. The DB index, plotted in figure 2.15c, has a global minimum at 11 clusters, implying that 11 as an optimal number of clusters and is hence chosen by the algorithm. The cluster membership of each prototype vector of the SOM for each of the 11 clusters is displayed in figure 2.15b. The color code indicates the class affiliation of each cluster after applying the signal determination step described in section 2.3.3.1. The particular example here indicates one tremor class S1 shown in red, a small earthquake class S2 shown in yellow, and 9 noise classes displayed in white, which are later merged to noise class N. The majority of data classified as noise also reflects the high sensitivity of the data reduction step described in section 2.3.1.

Another interesting visualization providing some insight in the signal class determination is the distribution of feature values for the different classes shown in figure 2.16. The

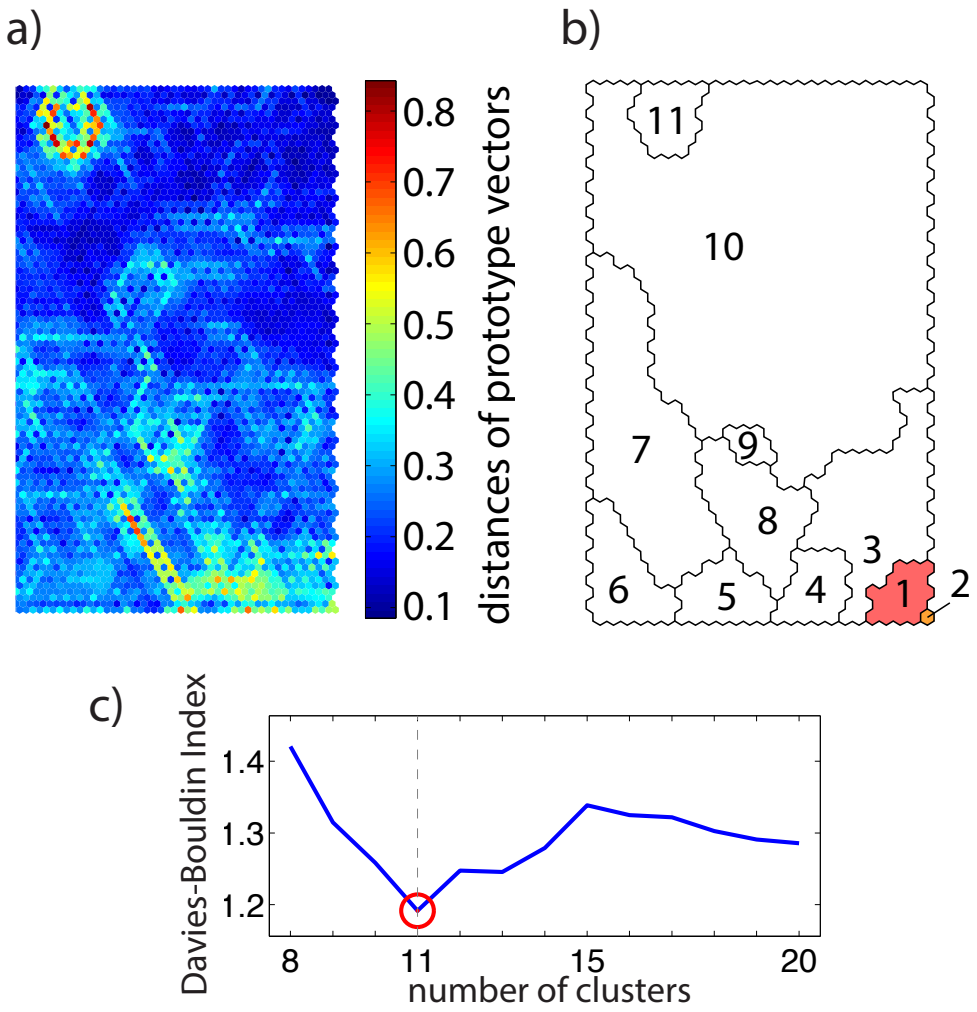

Figure 2.15.: Clustering of the SOM exemplary for data of 24th of May, 2010. The U-matrix in figure a) shows the distances between the prototype vectors in the data space, which is the basis for the clustering algorithm. The Davies-Bouldin Index in figure c) indicates 11 as an optimal number of clusters. The cluster membership of the prototype vectors for 11 clusters are shown in figure b). Cluster 1 is determined as a tremor class, cluster 2 as earthquake class and clusters 3-11 as noise classes.

color code indicates the three classes S1, S2, and N, and triangles denote the average values for each class. For example, within the PQ_{abs} feature, the values for the noise class are low with an average value of ~ 0.25, while the tremor class and earthquake class consist of higher values around 0.7. Furthermore, the distinctive high values around 0.8 at the lower frequency band of 0.5 to 1.5 Hz of the earthquake class S2 are clearly visible. The three frequency bands between 2 Hz and 8 Hz also show also higher values for the tremor class S1 and the earthquake class S2 compared to the noise class N. The values depend on

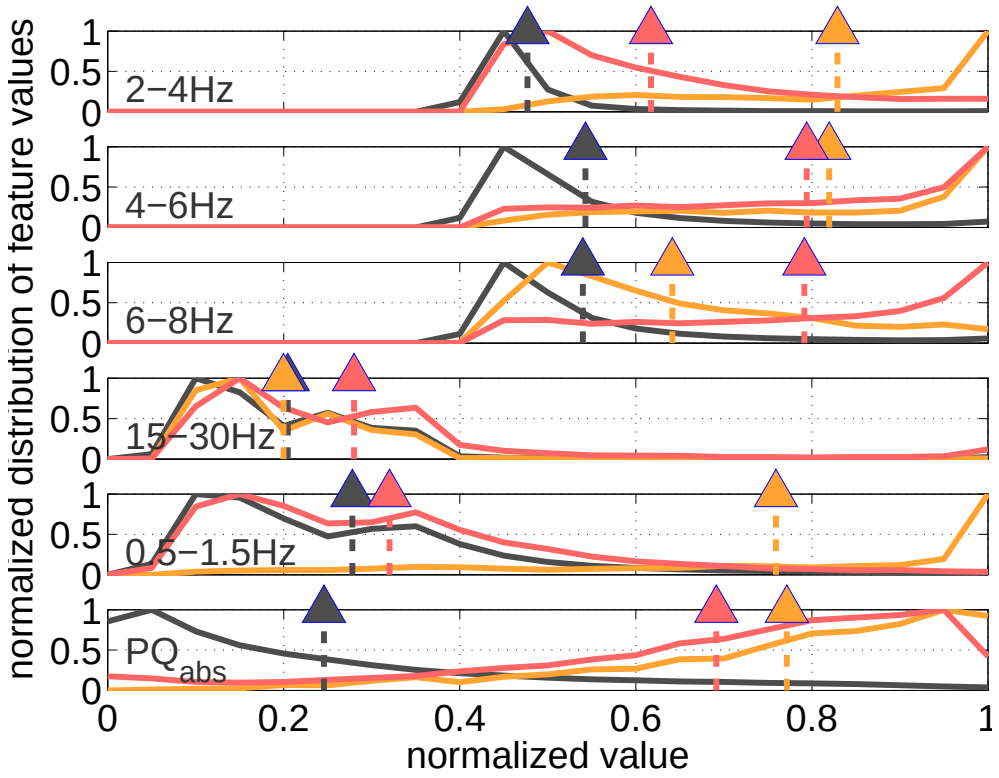

Figure 2.16.: Distribution of the feature values for different classes. Tremor class is shown in red, earthquake class in yellow, and the combined noise classes in black. Triangles indicate the average value.

the amplitude of the signals within the seismograms and thus of the signal-to-noise ratio, which is varying for each day. Please note that the absolute number of data points within each class is not indicated by the figure as the distribution curve is normalized to one.

2.4.3. Performance evaluation

2.4.3.1. Comparison to manually detected events

Using the feature and normalization parameters outlined in the methods section, I compare the detected event time windows to manually picked events in a three-week test data set from the beginning of the deployment, May 24th to June 14th. The manual picking, thus the manual detection and classification of earthquakes and tremor was performed by careful inspection of the raw and filtered waveforms. A correct detection is defined when a time window picked by the algorithm overlaps with a manually picked event. In some cases, the semi-automated method defines an event time window that is visibly shorter than the duration of a tremor episode. Detected time windows separated by more than 30 seconds are considered as individual events. While events separated by less than 30 seconds are grouped into a single event.

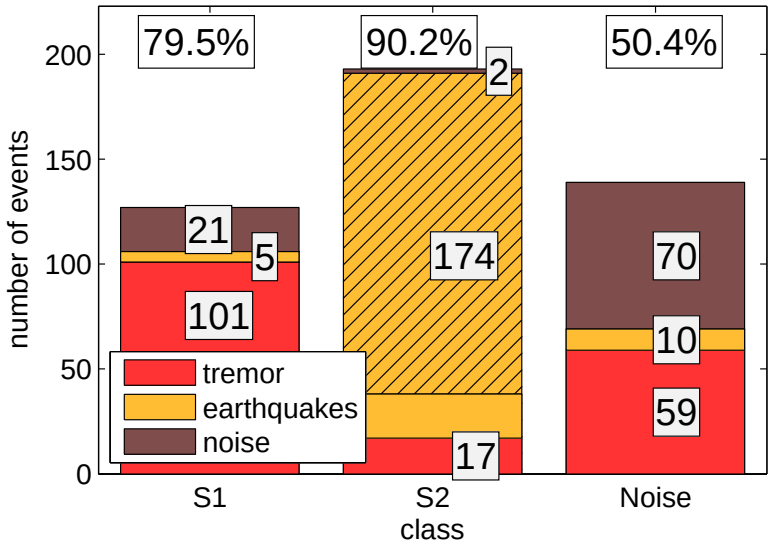

Figure 2.17.: Detection performance for the test data set. Tremor events shown in red, earthquakes in yellow, and noise in brown. Cluster composition of S1 class, S2 class, and rejected events within the noise class. Class S1 contains 101 tremor events, 5 earthquakes, and 21 noise windows resulting in a detection accuracy of 79.5%. Class S2 contains 17 tremor events, 174 earthquakes, and 2 noise events. Class N contains 59 tremor events, 10 earthquakes, and 70 noise time windows. Of the 174 earthquakes (class S2), 48 have been identified and moved from class S1 using the ANSS catalog , and 105 with the STA/LTA algorithm (hatched area).

Figure 2.17 shows the composition of classes S1, S2, and N. The events shown in class N consist only of those events which were moved from class S1 following the noise post-processing step; the events classified originally as noise by the SOM are not included. In total, the SOM and post-processing steps correctly detect 101 tremor events and obtains 26 false detections (5 earthquakes and 21 noise events) in class S1, equivalent to a detection accuracy of 79.5%. Class S2 consists of 174 earthquakes, 17 tremor and 2 noise events, corresponding to a 90.2 % detection accuracy. During the earthquake post-processing, the STA/LTA algorithm moves 105 earthquakes and 8 tremor events from class S1 into class S2. The comparison with the ANSS catalog shifts 48 earthquakes from class S1 to class S2, as well as 9 tremor events. The hashed area in class S2 represents the events moved from S1 to S2 in the earthquake post-processing step.

Figure 2.18 plots the detected event date versus event length for the three-week-long test data set. Roughly two-thirds of the detected events in classes S1 and S2 are shorter than one minute. The longest tremor signal has a duration of 13 minutes, but I note that the method often divides tremor episodes into separate events. The top panel of figure 2.18 indicates the events in class S1 detected by the algorithm after applying the post-processing steps. The middle panel (2.18B) shows the time windows in class S2 and the bottom panel (2.18C) the events in class N which are rejected by the noise post-processing

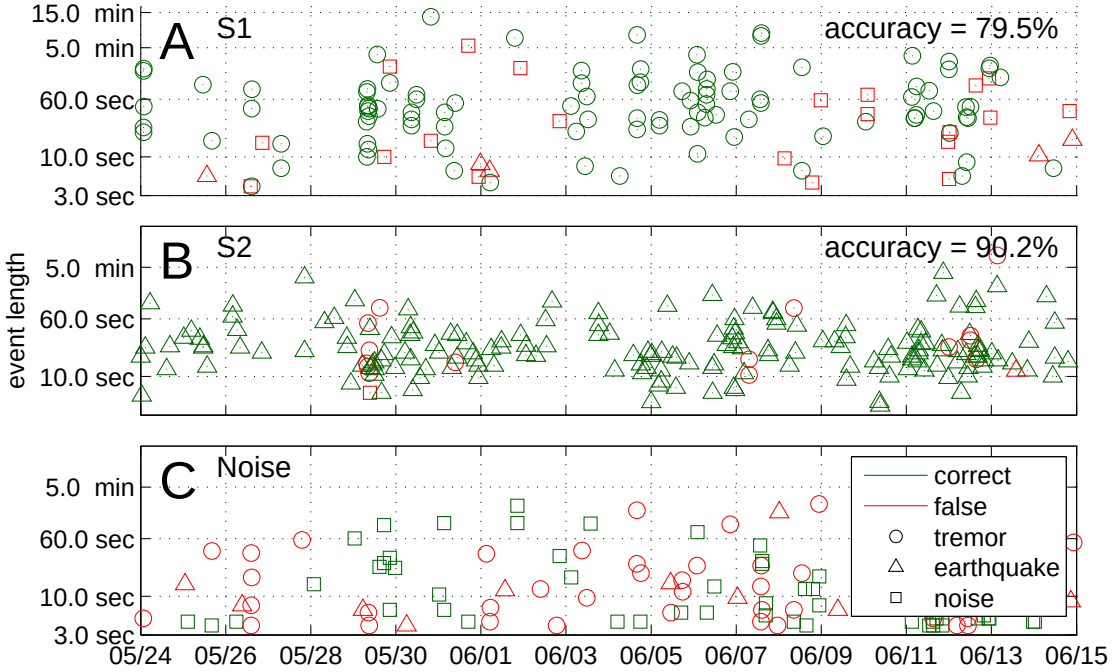

Figure 2.18.: Method performance on the test data set. (A) detected event time windows of class S1 plotted according to date and detected event length. Marker type denotes event type: tremor (circles), earthquakes (triangles), and noise (squares). Of a total of 127 automatically detected events, 101 are correctly detected tremor (green), and 26 are falsely detected (red) based on a comparison with manually picked events. Detection accuracy is 79.5%, and the sum of detected time windows is 141 minutes. (B) events in class S2 and (C) events moved from class S1 by the noise post-processing step.

step. Seventy time windows rejected by the post-processing step are removed correctly (green squares), while 69 manually picked events (i.e., correctly detected events) are removed (red circles and triangles). Of the 139 rejected time windows, 101 windows are shorter than 30 seconds (figure 2.18B). The noise post-processing step rejects events mostly due to alignment failure (section 2.3.2.2), high noise conditions, and/or detection of a small fraction of a signal.

2.4.3.2. Comparison to Wech and Creager [2008] Method

I compare the SOM method results for the three-week-long test data set with another commonly implemented detection algorithm developed by Wech and Creager (2008), referred to here as WECC. I implement the WECC method as it has been successfully applied for tremor detection in Cascadia, and is most comparable to my method as it detects more extended coherent tremor episodes rather than single LFEs. The WECC method calculates the cross-correlation of the envelopes of all station pairs within a 5-minute time window. Next, the method performs a grid search over all potential source-locations, searching for the S-wave lag times in order optimize the cross-correlation. There are a number

Method	Number of detections	Manual classification			Detection accuracy
		tremor	EQ	noise	
WECC	245	54	160	31	22%
WECC with STA/LTA	81	34	38	9	42%
SOM S1 class	127	101	5	21	79.5%

Table 2.6.: Results of the WECC method applied to the test data set. The results of the SOM method from section 2.4.3.1 are displayed in the last line for comparison.

	SOM classification			
	class S1	class S2	post-eval.	Detected events missed by the SOM
WECC	34	4	10	6
WECC with STA/LTA	25	3	4	2

Table 2.7.: Tremor detected by the WECC method compared to SOM detection method. Number of tremor events correctly detected ('class S1'), detected events incorrectly classified as earthquakes ('class S2'), events discarded by the post-evaluation step ('post. eval.'), and correctly detected events missed by the SOM ('missed by the SOM').

of adjustable parameters in the WECC method, namely cross-correlation window length, cross-correlation value threshold, and minimum number of stations for location. I tested different parameter settings finding that a time-window length of 300 seconds with a 150 second time step worked best for my data set. I only use observations with a maximum cross-correlation coefficient exceeding 0.5, and require a detection on a minimum of 5 stations.

One shortcoming of the WECC method is that it detects earthquakes and other coherent signals without any means of distinguishing such signals from tremor. Therefore, it is necessary to implement a post-processing step as well. Similar strategies to those used with the SOM may be adopted for distinguishing earthquakes and tremor identified by the WECC algorithm: one option is to use a STA/LTA trigger to exploit the distinct phase arrivals of an earthquake. A second strategy is to use a remote station to distinguish earthquakes from lower amplitude tremor. A third possibility is the use of an earthquake catalog. Here I use the same strategy as the post-processing step described in section 2.3.4.1, namely, and STA/LTA trigger paired with the comparison of an earthquake catalog. However, I now set the C5 constant from Allen (1982) to a value of 1.5.

I applied the WECC method to the test data set with and without the optional STA/LTA trigger. The method without the STA/LTA detects 245 events and only 54 are tremor according to my analyst picks. Of the 245 events, 160 are local and regional earthquakes, and 31 events are noise (see table 2.6). The STA/LTA reduces the detected events to 81, 34 of which are tremor events, 38 earthquakes, and 9 noise events, leaving a detection accuracy of 44%. In comparison, the SOM method detects 101 tremor events in the same

time period. Changing the parameter settings for the WECC method to adjust for higher detection sensitivity not only leads to an increase in detected tremor events (approximately 80), but also to an exponential increase in false detections (over 500).

A direct comparison of the algorithms is difficult given that the SOM may detect multiple tremor events (i.e., multiple time windows) within the 5-minute time window used by the WECC method. Therefore, I compare each detected tremor event by the WECC method directly with the detection result of the SOM method. Of the 34 tremor events detected by WECC, 25 were detected by the SOM method and correctly classified in class S1, 3 tremor events were missclassified as earthquakes by the SOM, 4 were thrown out by the SOM post-evaluation step, and 2 were not detected (see table 2.7). However, the SOM identifies an additional 76 tremor events that were not identified by WECC. Thus, 101 tremor events were correctly identified by SOM compared to just 34 identified by WECC.

A reason for the discrepancy may be the limitation that the WECC method requires spatial and temporal clustering. The advantage of the WECC method is its ability to locate and detect tremor at the same time and its computational efficiency. However, the SOM method detects more tremor events with a higher accuracy since it uses characteristics of the waveforms to classify different event types.

2.4.3.3. Influence of noise

Furthermore, I determine the influence of signal to noise ratio on the detection accuracy. Using the test data set with manually detected events, I define a detection completeness by dividing the number of automatically and correctly detected events by the total number of manually detected events, regardless of the difference in time window length. I calculate the detection completeness for bins of events with a similar SNR. The SNR is calculated by dividing the RMS amplitude of an event time window by the RMS amplitude of a noise window. The SNR is computed at each station on the vertical (Z) component. The individual noise window is manually selected. As the detection requires a minimum of three stations, I assign the third highest SNR of all stations to an individual event.

Figure 2.19A shows the detection completeness vs. the SNR. I differentiate between results with and without the noise post-processing step included (blue and red respectively) to show its influence. Note that the detection accuracy is lower if the noise post-processing step is not implemented. In order to reduce the false detections without applying the post-processing step, one could lower the detection threshold and increase the detection accuracy by choosing different normalizing parameters F_{mean} and F_{std}. However, evaluating the detection completeness of the method with and without the noise post-processing step is instructive, as it allows us to understand how the noise post-processing step influences detection accuracy.

Figure 2.19C indicates that for tremor, the method provides a detection completeness of 96% for events with a SNR above 3. The detection completeness is approximately 80% for signals with a SNR value of 2 or higher. However, it is important to note that the majority of tremor have a signal to noise ratio less than 2. I also find that the noise post-processing step may reduce the detection completeness in some cases. For example, events missed by the detection algorithm with a SNR ~ 3 are explained by failure of the noise

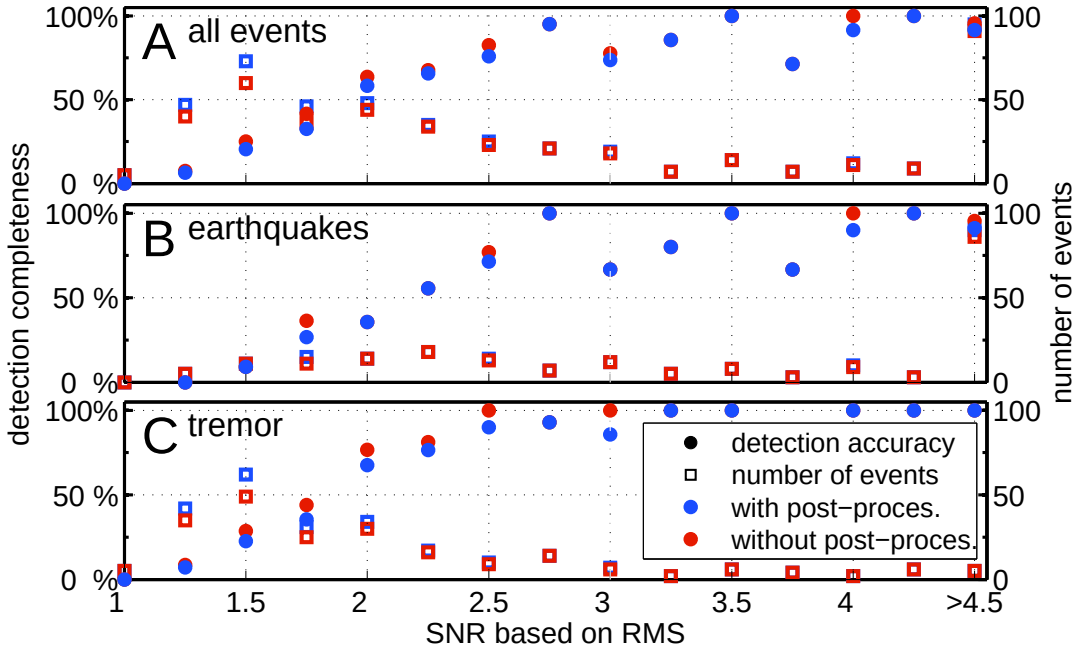

Figure 2.19.: Mean detection accuracy of events for a given signal-to-noise ratio (SNR) (dots). Squares indicate number of events within each SNR bin. Blue corresponds to results with the noise post-processing step included, and red corresponds to results before the noise post-processing step is applied. A) detection accuracy vs. SNR for all events, (B) detection accuracy vs. SNR for earthquakes, and (C) detection accuracy vs. SNR for tremor. Event classification is based on visual inspection. The y-axis indicates the detection accuracy in percent (left) and the total number of events determined by manual detection (right). Note that the results without the noise post-processing step include more false picks, resulting in a lower detection accuracy.

post-processing step. The noise level similarly influences the detection completeness for earthquakes. The influence of noise is minimal with a SNR > 3, although a small number of undetected earthquakes with SNR > 3 result from poor trace alignment. The majority of earthquakes have a SNR above 4.5 and are concentrated in the last bin.

2.4.3.4. Influence of the number of stations

I also determine the influence of the number of available stations used. In order to assess how the number of stations affects the detection accuracy as well as the total number and duration of detections, I employ a jackknife test. I run the detection algorithm using data from a set number of 3 to 15 stations. For a given number of stations, I use a random subset of the stations and repeat the analysis up to 250 times. I then calculate the mean and standard deviation values for each subset of stations (figure 2.20). Figure 2.20A shows

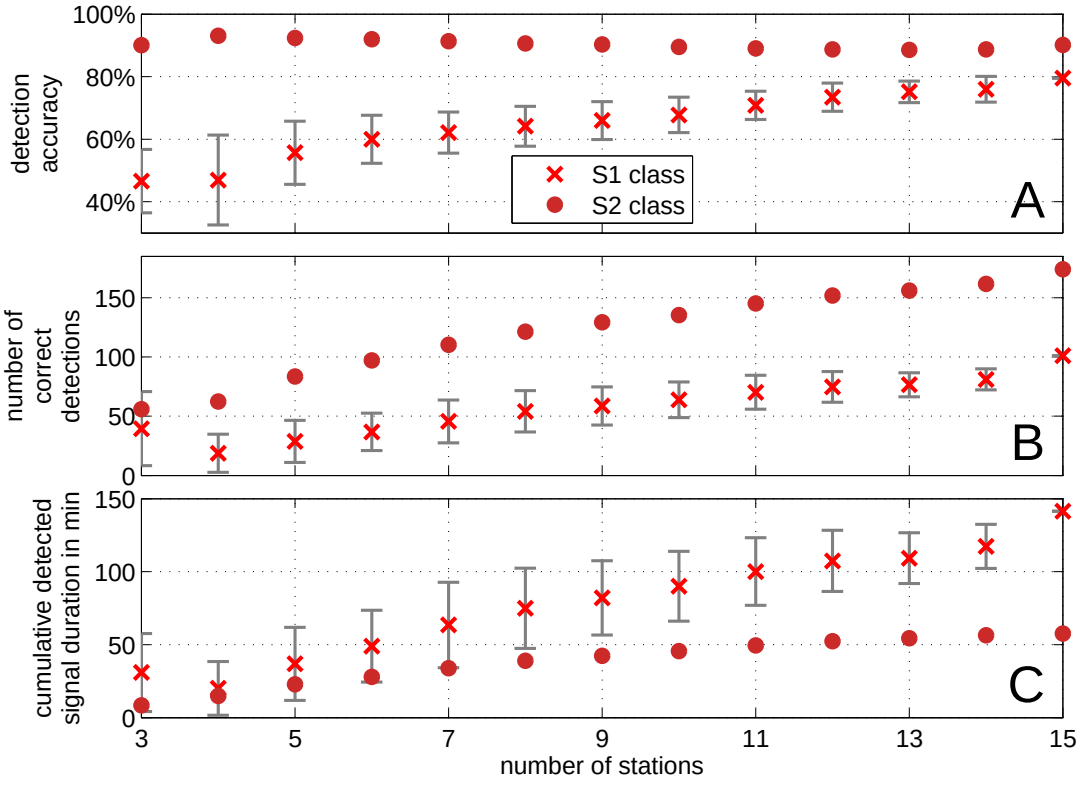

Figure 2.20.: (A) Detection accuracy, (B) number of correctly detected events, and (C) detected signal length vs. the number of stations used. Crosses display the result for the S1 (tremor) class, and dots indicate the results for the S2 (earthquake) class. Bars indicate the standard deviation within the averaged value.

the detection accuracy, 2.20B the number of correctly detected events, and 2.20C the total detected signal length vs. number of stations used. I perform the jackknife test for both classes S1 and S2 (crosses and dots respectively). The figure shows consistently higher accuracy for class S2 ($\sim$ 90%) while the accuracy for the tremor class S1 increases from 50% for three stations to 80% for 15 stations. Using the minimum number of stations (3) results in a detection of roughly 1/3 of all events with a high level of accuracy (90%) for class S2, but with a poor level of accuracy for class S1 (50%). As the number of stations is increased, the effects of noise at individual stations is reduced, particularly when borehole stations are considered. Additionally, an enlargement of the station array increases the spatial sensitivity to detect weak signals at the edges of the array.

I also test the influence of individual stations on the detection accuracy. I perform a jackknife test for each omitted station, with each test consisting of 250 random samples of (remaining) stations. I use the minimum number of occurrences for which any given station is included (N) in the random sampling to calculate the average values for each station over N samples (instead of 250). The jackknife test is performed in separate stages,

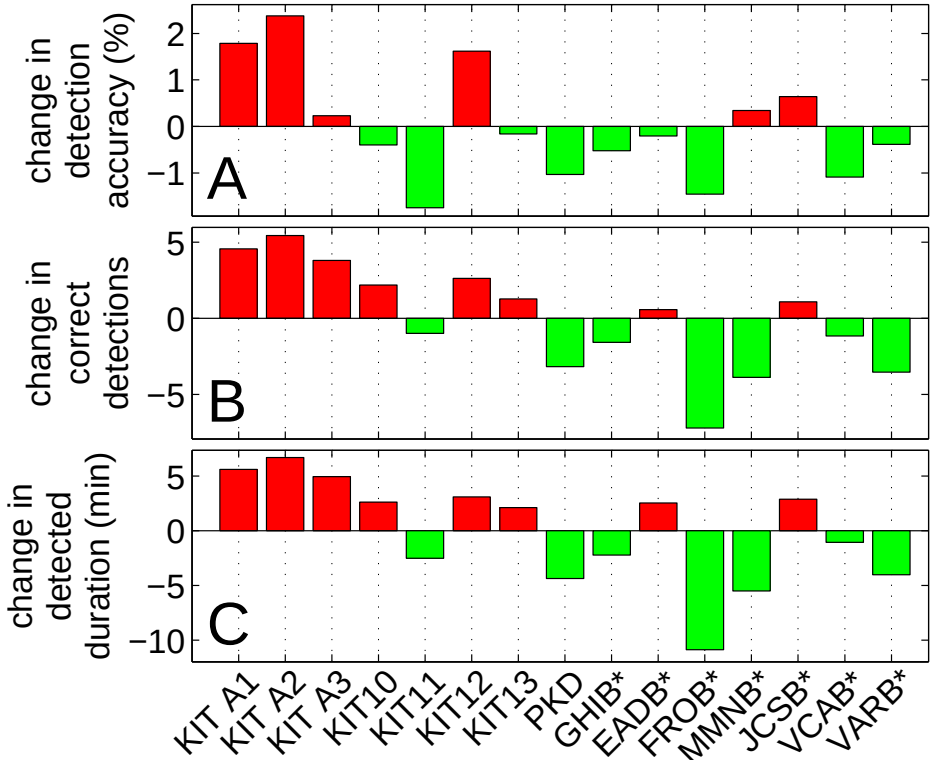

Figure 2.21.: Comparison of mean performance values from the jackknife test. (A) deviation from the mean detection accuracy value for each (neglected) station, (B) deviation in the number of correctly detected events, and (C) the deviation in detected signal length. Asterisks designate borehole stations. Negative values (green) indicate improved accuracy when a station is included.

in which a successively larger number of stations are omitted. The effect of omitting a specific station is shown in figure 2.21. Panel A displays the deviation from the mean detection accuracy. Negative values (green) indicate a decrease in the detection accuracy when a given station is omitted, indicating the importance of that particular station for the overall detection accuracy. Positive values (red) suggest that a given station is less important for performance accuracy. An asterisk is used to denote the borehole stations.

Figure 2.21 suggests that the stacked mini-array stations KIT A2 and KIT A1 have a negative influence on the detection accuracy while KIT 10 improves the accuracy slightly. Including all three stations in each of the mini-arrays decreases the number of correctly detected events and the detected signal duration, likely due to noisy conditions at the sites. Moreover, there is a clear difference between surface and borehole stations. Not surprisingly, the borehole stations perform better than the surface stations. The test indicates that the most valuable surface stations during the test dataset period are KIT11 and PKD, and the most valuable borehole stations are FROB and VARB.

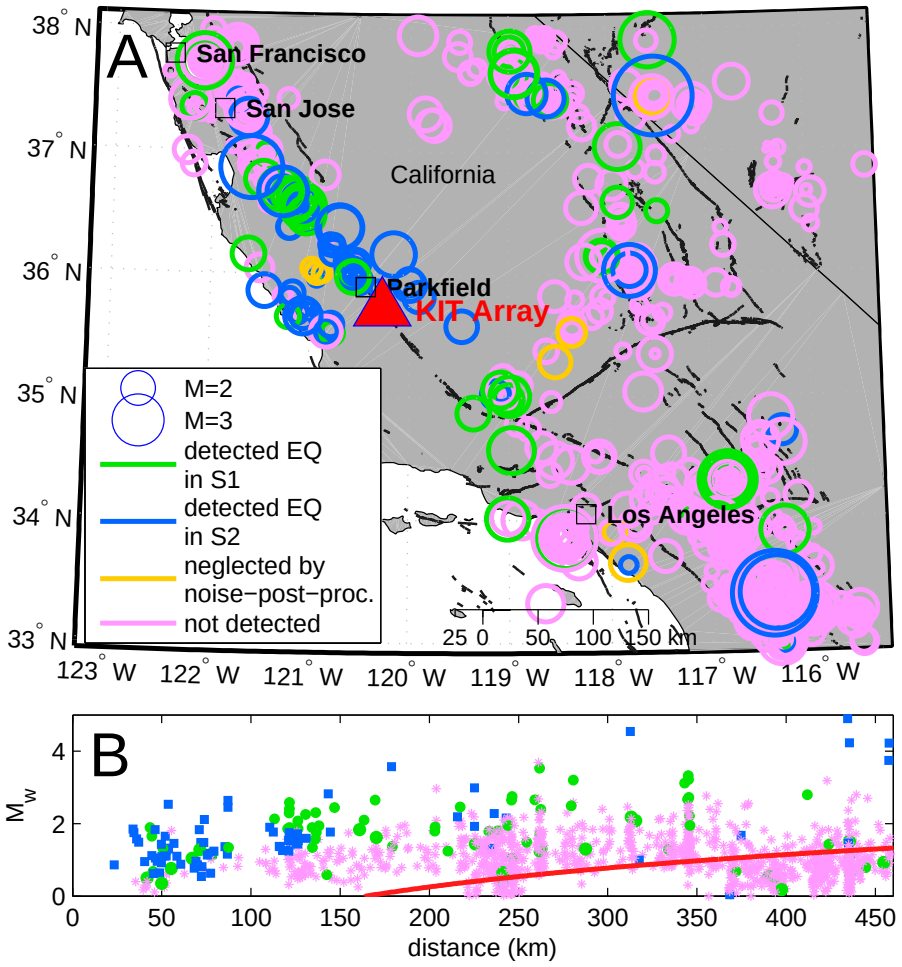

Figure 2.22.: Earthquake detection results compared to the ANSS earthquake catalog. (A) shows all earthquakes occurring within the test data period as circles. Circle size corresponds to catalog magnitude. Earthquakes detected and classified in the S1 class are shown in green, detected earthquakes classified in S2 are shown in blue, detected events rejected by post-processing shown in yellow, and undetected events shown in pink. (B) Earthquake magnitude vs. distance; the color code corresponds to (A). Distance is from the center of the KIT array. Red solid line displays the PGV threshold of 1400 nm/s.

2.4.3.5. Comparison with the ANSS earthquake catalog

In order to test the sensitivity of the detection algorithm to seismic signals in general (i.e. classes S1 and S2), I compare the detection results with the ANSS earthquake catalog as described in section 2.3.4.1.

Cross-checking the events found by manual inspection with the events detected by the SOM indicates that the SOM finds a total of 179 earthquakes within classes S1 and S2 (figure 2.17). A comparison with the ANSS catalog indicates that 135 of those events were cataloged, and that 9 tremor events were falsely classified as earthquakes. The remaining

44 events are not cataloged. Figure 2.22A shows the proportion of earthquakes from the ANSS catalog detected by the SOM. The circle size corresponds to the catalog magnitude and the circle color indicates the detection result: blue circles denote earthquakes detected correctly and classified in class S2, green circles denote earthquakes detected within class S1, yellow circles denote events initially detected and later rejected by the post-processing step, and pink circles represent events not detected by the method.

Figure 2.22B shows the ability of the method to detect almost every earthquake above a certain magnitude-distance threshold. Most of the earthquakes that occur within 150 km are classified correctly as earthquakes by the STA/LTA algorithm within the earthquake post-processing step. Most of the earthquakes incorrectly identified as class S1 that occur at distances between 150 km and 350 km are moved to class S2 by the earthquake catalog comparison described in section 2.3.4.1. Note that some small earthquakes occurring at large distances are falsely marked as detected because they occur within the window of a detected tremor event. I therefore apply the earthquake catalog comparison in the earthquake post-processing only to earthquakes with a PGV $>$ 1400 nm/s (indicated by the solid red line in figure 2.22B). Figure 2.22B suggests that small earthquakes not in the ANSS catalog that occur close to the stations are often discarded during the noise post-processing step.

2.4.4. Analysis of the 14-Month Dataset

After quantitatively assessing the detection algorithm performance using the three-week-long test data set, I apply the method to the entire 14 month dataset collected between the 24th of May, 2010, and the 30th of June, 2011, using parameters established during calibration of the method. The parameter values are given in section 2.3.

The results for the complete dataset are plotted in figure 2.23. During the 13 month long study period, the SOM detects some tremor almost every day. I find over 2606 tremor detections occurring in windows totaling over 55 hours, with an estimated detection accuracy of 80%. Panel A shows the number of events detected in class S1 per day, reflecting primarily tremor signal (figure 2.17). A tremor event in class S1 corresponds to a time window separated by at least 30 seconds from the subsequent event window. As mentioned in section 2.4.1, the method tends to split low amplitude tremor episodes into several individual bursts; thus multiple detected time windows could be affiliated with a single extended event. The estimated number of events per day, ranging between 0 and 61, reflect high amplitude tremor arrivals or 'bursts' that may occur within longer duration, low amplitude episodes. The gap in late December coincides with a drop in the number of stations used, which is due to station outages. However, generally I do not see a correlation between the number of stations used and the number of detections. The nearly linear increase in cumulative signal duration shown in figure 2.23C suggests a constant rate of seismic activity as well as a stable detection sensitivity over the study period. There is an average of 6.5 events with a cumulative signal duration of 8.2 minutes per day. There are days when the number of detections are much higher than average, for example, in the beginning of September 2010 and at the end of January 2011. To identify teleseismic or regional wave arrivals at the array, I estimate the peak ground velocity (PGV). I find no evidence suggesting increase in detections is correlated with the

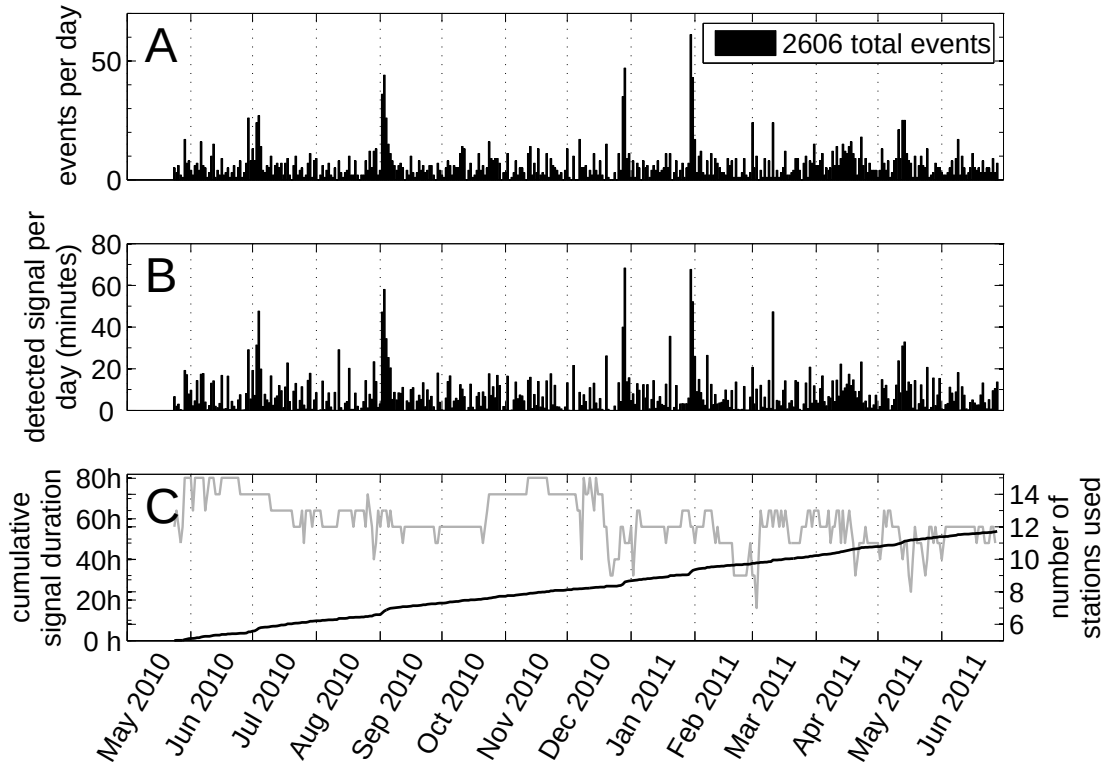

Figure 2.23.: Detection results for the complete dataset: (A) detected tremor events per day, (B) minutes of detected signal per day, and (C) cumulative signal duration (black curve). Panel C also shows the number of station used each day (gray curve).

occurrence of large earthquakes (i.e., with high PGV). Moreover, visual inspection does not suggest an increase in false detections for days with a higher than average number of detections. Thus, the step increases in the cumulative signal duration likely reflect the true behavior of ambient tremor. Similar observations of episodic tremor episodes in the area are previously described by Nadeau and Dolenc (2005), Nadeau and Guilhem (2009), and Shelly (2010).

2.5. Chapter conclusions

I present a new method for tremor detection based on a neural network approach. The method identifies and distinguishes tremor, earthquakes, and noise based on frequency content and horizontal to vertical component products. I initially use a waveform envelope cross-correlation to reduce the data volume, and increase computational efficiency. The method does not rely on *a priori* information such as event templates and is capable of identifying tremor bursts of variable duration, assuming some variation in tremor amplitude within the length of the noise window (420 sec). Moreover, the sensitivity of the method can be adjusted by a set of normalization factors, F_{mean} and F_{std}.

The method detects 2606 events within the continuously recorded dataset from May 2010 to July 2011. The tremor detection accuracy is nearly 80% for the SOM and post processing steps, estimated by comparison to manual picks in a three week long test dataset. I expect similar detection accuracy for the entire study period. A comparison of the earthquake detections with the ANSS catalog shows a detection accuracy of approximately 90%. The event detection is based on a minimum of 3 stations. However, optimum detection requires approximately 10 stations for the particular network configuration. And, the overall best performance is achieved when 4 key stations (KIT11, PKD, FROB, and VARB) are included in the analysis. One limitation of the method is that it generally detects only a portion of the tremor episode, typically identifying high amplitude portions of a longer, low amplitude tremor episode.

The method is in general very flexible and could be adjusted by supplementing further features and/or by changing the detection sensitivity. Although I tested a variety of features to discriminate tremor from noise in my dataset, the features determined to be most discriminating may differ for other data sets. For example, including polarity as a feature might be useful when observed tremor is polarized, such as examples shown by Wech and Creager (2007). In addition, taking into account the energy in the frequency band common to surface waves might help to identify and distinguish triggered tremor from ambient tremor. The fundamental advance of the method is that it does not rely on master templates and is not based on any assumptions about a minimum signal length. Removing such restrictions permits the detection of a wider range of event types than present methods, thereby increasing the potential for discovering tremor at different depths within the fault zone.

The method does not provide locations for the detected tremor, however, the method could be useful to restrict the time period for a LFE search with a template matching method. Other methods to locate tremor such as envelope triangulation could also be applied to the detected tremor periods or location with the time-reversal approach described in chapter 3.

3. Tremor localization

3.1. Introduction to tremor localization

Despite the numerous observations of tremor, the lack of distinctive phase arrivals and low amplitude signals makes locating tectonic tremor more challenging than locating earthquakes. Since its discovery by Obara (2002) numerous methods to locate tremor have been developed. They can be grouped mainly into three classes: methods based on waveform envelopes, the use of stacked low frequency events (LFE's), and methods exploiting array techniques.

Waveform envelope based methods developed by Obara (2002) have also been used in other studies (e.g., McCausland et al. (2005); Payero et al. (2008)). Such methods determine arrival time differences for station pairs by cross-correlating the envelopes of the seismic trace and using the time differences to obtained a source location by triangulation. Alternatively, one can use the time differences in a grid search over possible source locations (e.g., Kao and Shan (2004)). The advantages of the envelope based location techniques are the speed and the semi-automated fashion of the methods. However, the methods lack on precision determining arrival times precisely and require seismograms with a good signal-to-noise ratio to produce stable results.

The discovery of LFE events within tremor episodes enabled new methods for location which exploit event similarity, allowing stacking multiple events in order to enhance phase arrivals. Shelly et al. (2006) showed that many LFE's are multiplets which occur in event families, allowing for stacking of multiple events. The improved signal-to-noise ratio of the stacked events enables picking of P- and S-phases, making source locations calculated with classical earthquake location algorithms possible. The disadvantage of the approach is the need for *a priori* information of LFE master templates, multiple occurrence, and the assumption that all stacked events occur at the same source location. Correlation of coefficients between LFE's in a given event family can be in average as low as 0.33, calling the assumption of a similar source location into question (Shelly et al., 2007).

Other methods imply the use of array techniques to measure slowness and back azimuth

and to partially exploit wave polarization, however a special station and array distribution is needed (La Rocca et al., 2005, 2008; Ryberg et al., 2010; Fletcher and Baker, 2010).

On the other hand, the application and development of time-reversal-imaging (TRI) methods has been steadily increasing. TRI methods back propagate the recorded and in time reversed signals back into the medium at the recording position. The back propagated wavefields interfere positively, thus creating a large amplitude at the original source position, allowing one to locate and characterize the source (Anderson et al., 2011). The general advantage of the TRI method is the potential to exploit of the full waveform without any knowledge about the recorded signal such as phases. An overview of different TRI methods can be found in Anderson et al. (2008), that have been successfully applied in the field of non-destructive evaluation of materials to locate and characterize cracks (Ulrich et al., 2006, 2007) and to estimate shear elasticity of materials (Brum et al., 2008). TRI has been also used for locating land mines (Sutin et al., 2009), as well as in biomedical imaging and therapy, such as tracking kidney and gallstones (Fink et al., 2003) and imaging of human teeth (Santos and Prevorovsky, 2011). Furthermore, TRI has been applied to the Earth in order to locate seismic sources, such as the 2004 Sumatra earthquake (Larmat et al., 2006) and Lokmer et al. (2009) showed the ability to locate a synthetic vulcanic tremor source, and Larmat et al. (2009) determined the ability to locate a long-lasting tectonic tremor source in a synthetic study. Drawbacks to the application of TRI methods to seismic data include the often sparse coverage of stations, the lack of deeper borehole stations, and finally, inacuracies in the velocity model. In the case of tremor a very low signal-to-noise ratio within the recorded signals adds to the problem.

Here, I apply a modified TRI method to seismic data recorded on the San Andreas fault near Parkfield in order to locate individual LFE's within tremor episodes. I further develop the TRI method by introducing an imaging condition: instead of looking at individual snapshots of the time-reversed wavefield for the biggest amplitude due to a constructive interference, I search for phase coherence over a short time period with a matched filter approach. The advantage of the modified TRI method is the independence of amplitude and the inclusion of temporal information making it suitable for low amplitude signals and sparse station configuration as is the case with tremor localization.

In the following, I first introduce the modified TRI method in the methods section 3.2, followed by a description of the data in section 3.3. I will present my location results in section 3.4, including synthetic tests performed to test the method, described in sections 3.4.1 and 3.4.2 and the application of the method to a recorded M 1.4 earthquake and recorded LFE events within tremor episodes in sections 3.4.3, 3.4.4, and 3.4.5.

3.2. Methods

The fundamental premise of the time-reversal imaging technique is to locate seismic signals using the constructive interference of rebroadcasted seismic waveforms. The technique propagates a time-reversed seismic signal recorded at discrete points at the surface, back into the subsurface. Assuming a similar waveform of all rebroadcasted wave fields at the source time and source origin, one can search for coherence of the wave fields in time and space to obtain the source location and origin time where the constructive interference is a maximum. Figure 3.1 illustrates the technique schematically in three parts:

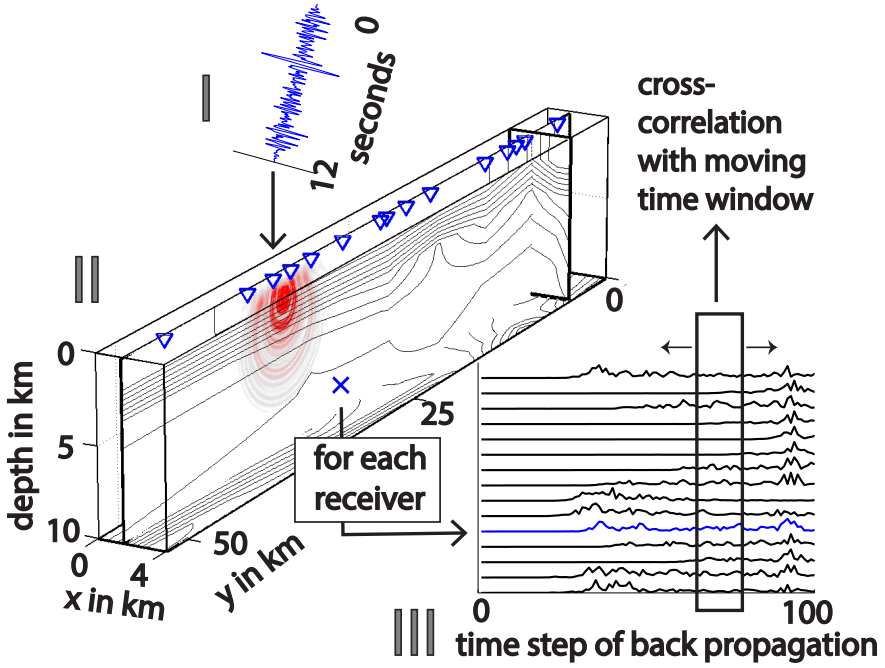

Figure 3.1.: Schematic sketch of the method: time reversed seismograms (I), plot of the curl field produced by back propagation (II) of the time reversed seismograms from all receivers at an individual gridpoint. I search the curl field for peaks in coherence by cross-correlating the functions of the curl fields at each grid point in a moving time window (III). Velocity model orientation corresponds to the coordinates described in Thurber et al. (2006) with positive y trending Southeast.

the time reversal of the data (I), the back propagation into the subsurface (II), and the evaluation of coherence in time and space (III).

In the first step I pre-process the seismograms of all three recorded components by removing the instrument response to get the true ground motion and filtering the seismograms between 1 Hz and 5 Hz. The frequency band is chosen based on two criteria: firstly, the tremor observed near Cholame typically has its highest energy concentrated in the 2 - 8 Hz frequency band (Obara, 2002; Schwartz and Rokosky, 2007; Beroza and Ide, 2011). Secondly, some studies suggest that the high-frequency energy goes down to 1 Hz (Shelly et al., 2007; Brown et al., 2008; Wech and Creager, 2008). I limit the higher frequency to 5 Hz, as the computational demand for the back propagation calculation increases exponentially for higher frequencies. Furthermore, the back propagation becomes more affected by the inaccuracies in the velocity model at higher frequencies due to smaller wavelenghts. Next, I interpolate the sampling rate of the seismograms equal to the time step used in the calculation of the back propagation. Afterwards, after rotating the seismograms in the local coordinate system of the velocity model grid, the seismograms are ready for rebroadcasting in the subsurface. Finally, I reverse the seismograms in time to be able to use them in the back propagation calculation as source function.

I use the staggered grid, finite-difference (FD) code of Bohlen (2002) and the 3D velocity model of Thurber et al. (2006) to back propagate the prepared seismograms (figure 3.1 II). The calculation of elastic wave propagation employs an 8th order spatial Holberg FD operator and perfectly matched layer (PML), to absorb the energy at the boundaries in my model as described by Komatitsch and Martin (2007). I set the spatial dimension of the PML to 15 grid points, the dominant frequency to 5 Hz, and the velocity near the boundary to 3.5 km/s. I interpolate the velocity model to an even grid spacing of 100 m and add the first layer 15 times to the top of my model to account for the PML absorbing frame. The grid spacing is chosen based on the minimum shear wave velocity in my model and the maximum frequency of the source signal to avoid grid dispersion due to an inaccurate spatial sampling. According to the maximum P-wave velocity and the grid spacing, we set the time step to 5 ms for the calculation of elastic wave propagation to fulfill the Courant-Friedrichs-Lewy criterion (Courant et al., 1967) and ensure the stability of the FD code by an accurate temporal sampling. During the calculation, I write out the relative curl field energy amplitudes in my model every 50 milliseconds for each rebroadcasted seismogram, gaining a time series of the curl field for each grid point (figure 3.1 III). The relative curl field energy amplitudes are calculated within the FD code from the displacement after Dougherty and Stephen (1988). I use the curl field, because much of the energy in tremor bursts is contained in shear waves (La Rocca et al., 2009; Wech and Creager, 2007; Payero et al., 2008; Miyazawa and Brodsky, 2008), and shear waves have higher amplitudes than longitudinal waves .

In the final step, I search for coherence within the curl field in time and space. I do so by a grid search which cross-correlates all combinations of the time series of the curl fields in a sliding time window. To account for 180° phase shifts due to radiation patterns of double couple sources, I take the absolute value of the cross-correlation value. Additionally, I introduce a cross-correlation condition: if the local maximum correlation coefficient between any two time series within the time window is lower than 0.5 times the global maximum for either time series, I skip the calculation and set the cross-correlation value to zero. The condition avoids numerical artifacts caused by division by zero, decreases the computation time, and improves the result by avoiding artifacts, e.g. locally high cross-correlation coefficients at random grid points. The cross-correlation is carried out in a time window of 1.5 seconds and a time step of 0.1 seconds. Finally, I calculate a median cross-correlation value at each grid point and within each time window and search for the highest cross-correlation median value, which indicates the origin source position. I allow the source position to be only in the sub-volume of the model which excludes the absorbing layers and the receiver positions, thus I ignore the 15 grid points next the model boundaries, and neglect the top 30 grid points.

Figure 3.2 exemplifies the result for one snapshot in time. The median cross-correlation value distribution shows a clear maximum around gridpoint B2, interpreted as source position. Gridpoints B1 and B3 exhibit a low coherence as documented by the functions of the curl field.

I calculate a relative error of the determined source position by considering the positions of the highest local maxima of median cross-correlation values in the model, i. e., the calculated source location. I estimate the uncertainty of the solution by determining the distances to the obtained source position of all cross-correlation maxima exceeding a value

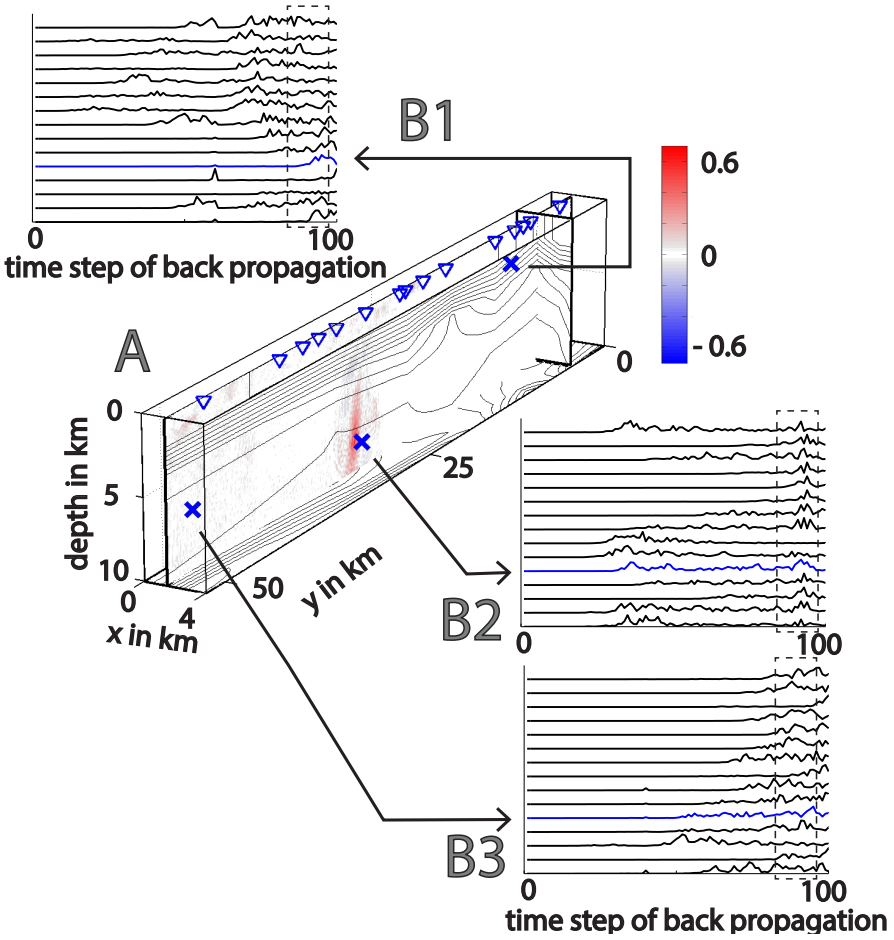

Figure 3.2.: Evaluation of curl field coherence in time and space: the model volume (A) is same as in figure 3.1, however contours now represent curl-field coherence for one snapshot in time. The color code shows the distribution of the median cross-correlation values for the time window indicated by the dashed boxes. B1, B2, and B3 show the functions of the curl field from each of the receivers at individual gridpoints (shown as 'x's). Note the high cross-correlation values around grid point B2.

of 90 % of the global maximum throughout all calculated time steps. Thus, the spatial range over which the maximum exceeds the 90 % value maximum along each coordinate axes constitutes the relative error distance.

3.3. Dataset and FD model

I use seismograms from both permanent stations, and waveform data recorded during a temporary deployment of 13 surface stations from the KABBA array at seven sites around Cholame, California, forming the PERMIT array. The KIT labeled PERMIT stations are equipped with STS-2 sensors and record continously at a 200 Hz sampling frequency from

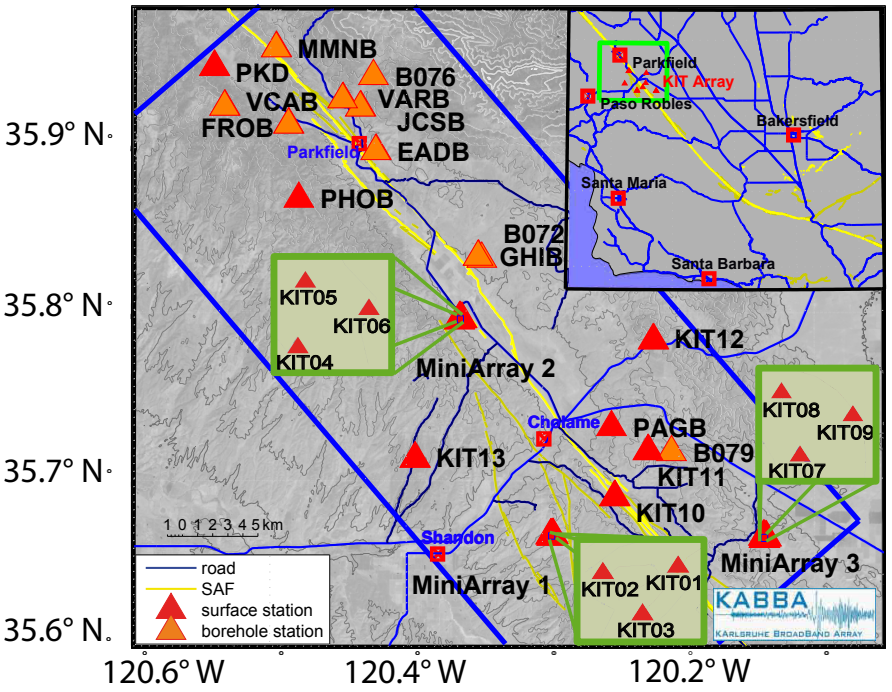

Figure 3.3.: Station distribution of PERMIT Array and additional surface stations from the BK and NC networks as well as borehole stations from the HRSN and PBO networks. The extend of the model volume used here is indicated by the blue line.

May 2010 to July 2011. Data from permanent stations include data from station PKD from the Berkeley Digital Seismic Network (BDSN), station PHOB and PHF from the Northern California Seismic Network (NCSN), and the borehole stations GHIB, EADB, FROB, VCAB, VARB, MMNB and JCSB of the Berkeley High Resolution Station Network (HRSN) and stations B072, B076, B078, B079 and B901 of the Plate Boundary Observatory (PBO). The station distribution, shown in figure 3.3 covers approximately 50 kilometers of the Cholame segment of the San Andreas Fault (SAF). Recent studies have shown that much of most vigorous tremor activity occurs on the San Andreas Fault beneath Cholame, which is why I focus my study here (Shelly and Hardebeck, 2010; Ryberg et al., 2010; Nadeau and Guilhem, 2009).

I apply the coordinate system adopted by the 3D velocity model of Thurber et al. (2006) for the finite difference calculation, with origin at $35°57.60'$ N and $120°30.28'$ W and a Y-axis rotation from an azimuth $139.2°$. My model has 240 grid points in the cross-fault direction (X-direction), 520 grid points in the fault parallel direction (Y-direction), and a depth of 280 gird points corresponding to a dimension of 24 km x 52 km x 28 km and a total number of 34,944,000 grid points. The upper left corner is located at -14km in the x-direction and -2 km in the Y-direction in the Thurber coordinate system. The model location and geometry is indicated as a blue box in figure 3.3.

The velocity model of Thurber et al. (2006) contains P-wave velocity v_p value only, I

therefore calculate the shear wave velocity v_s and the density ρ assuming a Poisson solid. The expression for v_s is given by

$$v_s = \frac{v_p}{\sqrt{3}}. \tag{3.1}$$

Brocher (2005) determined an empirical relationship between v_p and ρ determined primarily by velocity measurements on rock samples, boreholes, and seismic studies from California, USA. The relationship is valid for $1.5 < v_p < 8.5$ km/s and is given by

$$\rho = 1.6612 \cdot v_p - 0.4721 \cdot v_p^2 + 0.0671 \cdot v_p^3 - 0.0043 \cdot v_p^4 + 000106 \cdot v_p^5 \quad , \tag{3.2}$$

with v_p in km/s and ρ in g/cm^3. I use equations 3.1 and 3.2 to calculate a shear wave and density model from the P-wave model of Thurber et al. (2006) for use in the wave propagation calculation during the rebroadcasting of the seismograms.

3.4. Results

The result section is structured as follows: first, I determine the performance of the method in a 2D test in section 3.4.1. Due to computational reasons I restrict my calculation to a 2D cross section and use for my synthetic source a force in z-direction. The enhanced computational performance allows us to determine the influence of noise in the seismograms and velocity perturbations in my velocity model. Next, I show the functionality of the method with a synthetic double couple source in section 3.4.2 and apply my method to a recorded M 1.4 earthquake in section 3.4.3. Here, I show the velocity model being a limiting factor, which can be compensated by tapering the S-phase in the seismograms. Finally, I present the results for recorded tremor in section 3.4.4.

3.4.1. Synthetic 2D test with a single force

I start by testing the method with a simple synthetic velocity model, where I calculate synthetic seismograms for a single force and calculate the source position with the time-reverse imaging method. To speed up the calculations, I use the 3D wave propagation code but only consider a 2D cross section at x=20km in my 3D model. Considering a 2D cross-section allows us to limit my model to 40 grid points in the x-direction including 30 grid points in the absorbing layers. The model geometry is shown in figure 3.1 and 3.2. The enhanced computational time enables us to also test the influence of SNR of the recorded seismograms and perturbations to the velocity model.

I use a single impulsive force in the z-direction as a source and distribute the receiver positions randomly at the trace of the 2D cross section below the absorbing layer at the surface. I place the synthetic source at coordinates x=20km, y=30km, z=8km and calculate in a first step synthetic seismograms at the receiver positions in a forward calculation.

Next, I corrupt the synthetic seismograms in four cases with white noise, creating seismograms with SNR of 5, 2.5, 1.66, and 1.25 for each receiver. Figure 3.4 shows exemplary the waveforms with a SNR of 2.5. Moreover, I add Gaussian distributed perturbations of 10% and 20% of the median velocity value to the velocity model of Thurber et al. (2006). Finally, I locate the source position based on the different subsets of seismograms and

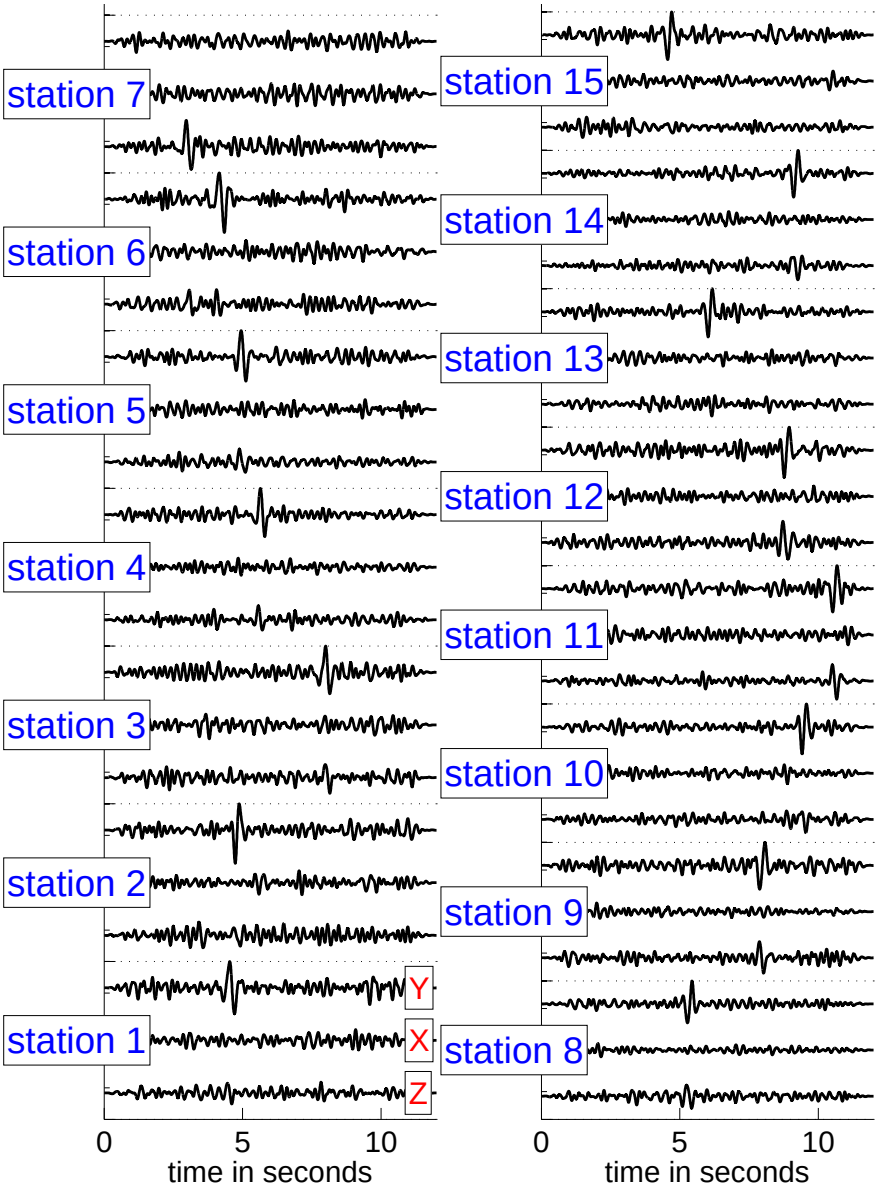

Figure 3.4.: Example of waveforms used in a synthetic test to evaluate the effects of noise and velocity model perturbations. THe example shown in the figure is perturbed with white noise with a SNR of 2.5 and filtered between 2 and 5 Hz. The seismograms are used for rebroadcasting in the subsurface.

velocity models and evaluate the maximum cross-correlation value and maximum artifact value for each combination. An artifact value denotes a spuriously high values in the cross-correlation coefficient that are certain unrelated to source effects.

Figure 3.5 shows the location result using the seismograms with a SNR of 2.5 and the original velocity model (without perturbations). The color contours indicate the distribution of the median cross-correlation values inside the cross section for time window 82,

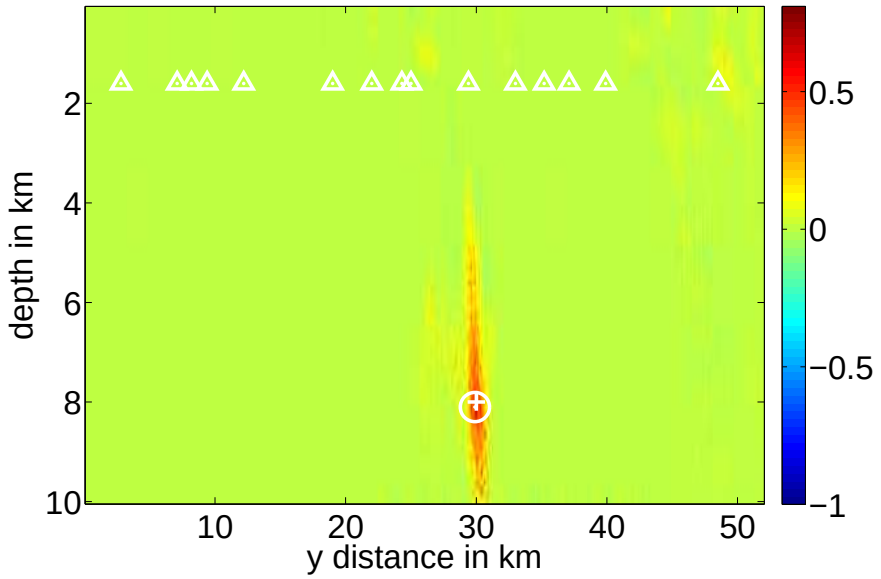

Figure 3.5.: Median cross-correlation coefficient values in a cross section of figure 3.2 for time window 82. White triangles show receiver positions, white circle indicates the maximum value, and the white cross marks the synthetic source location at 30 km horizontal distance and 8 km depth. Example with signal-to-noise ratio of 2.5 and without velocity perturbation. The rebroadcasted waveforms are shown in figure 3.4.

which corresponds to a time of 8.2s given the 0.1s time steps within the back propagation. The highest cross correlation value is interpreted as source position, which differs 100 m horizontally and 400 m vertically from the original source position. The compactness of the color contours in the horizontal direction indicates a better horizontal resolution due to the receiver distribution at the top of the model.

In contrast to the single snapshot shows figure 3.6 shows the temporal progress of the cross-correlation values using the seismograms with a SNR of 2.5. The figure illustrates the highest median cross correlation value at the determined source position and the maximum median cross correlation value at any non source position, i.e., the highest artifact value, for all time steps. The maximum source cross-correlation value is almost 0.8 while the maximum artifact value has a value of approximately 0.4. Thus, the determination of the highest median cross-correlation value and thereby the source position has a ratio of 1.9.

Figure 3.7 summarizes the results of the noise test for different SNR levels within the seismograms and the different velocity model perturbations. Figure 3.7 shows the maximum source value and the maximum artifact value for each combination of back propagated seismograms with a given SNR and velocity perturbation. The maximum source value decreases from roughly 0.9 to 0.3 with decreasing SNR as expected. The maximum artifact value is approximately 0.4 and does not vary significantly with SNR. The results of the test show that the source position is reliably recovered up to a maximum noise ampli-

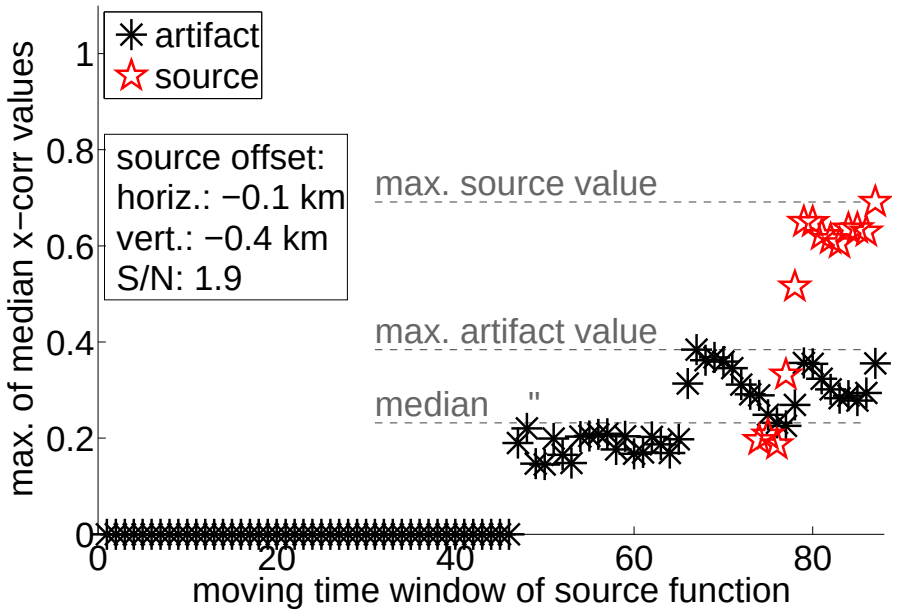

Figure 3.6.: Maximum value of the median cross-correlation coefficients in each time step. Example with signal-to-noise ratio of 2.5 and without velocity perturbation. Black stars mark artifacts (i.e., non-source values), red stars indicate the maximum cross-correlation value at the source position.

tude of 60% of the maximum median cross-correlation value. For lower SNR one would need additional information to recover the source position, e.g. the stability of the maximum cross-correlation value in time. The different perturbations to the velocity model have only a minor influence on the median cross-correlation value. A possible explanation is that the perturbations have a zero mean, thus the travel time differences may average each other out.

3.4.2. Synthetic test with a double couple source

In the previous section I used a force in z-direction as a source to calculate synthetic seismograms. Thus the radiation pattern depends only on the dip of the ray-trace, as the radiation pattern is cylindrically symmetric. I would like to verify that the method is able to reliably recover the source location of a seismic event such as an earthquake with a variable radiation pattern. I therefore generate synthetic seismograms of a double-couple source and locate the synthetic earthquake using the TRI method. I use the 3D velocity model previously described in section 3.3 (with no perturbations in the velocity values) and evaluate the complete 3D model volume for both the forward modeling and the rebroadcasting in the double-couple synthetic test. The fault plane and slip direction of the double couple source is characterized by three angles, the dip, the strike, and the rake. For the test I chose a strike of $0°$, a dip of $45°$, and $90°$ rake.

Figure 3.8 shows the median cross-correlation value distribution within the model volume for a snapshot at $t = 7.9$s in which the maximum cross-correlation value occurs. The

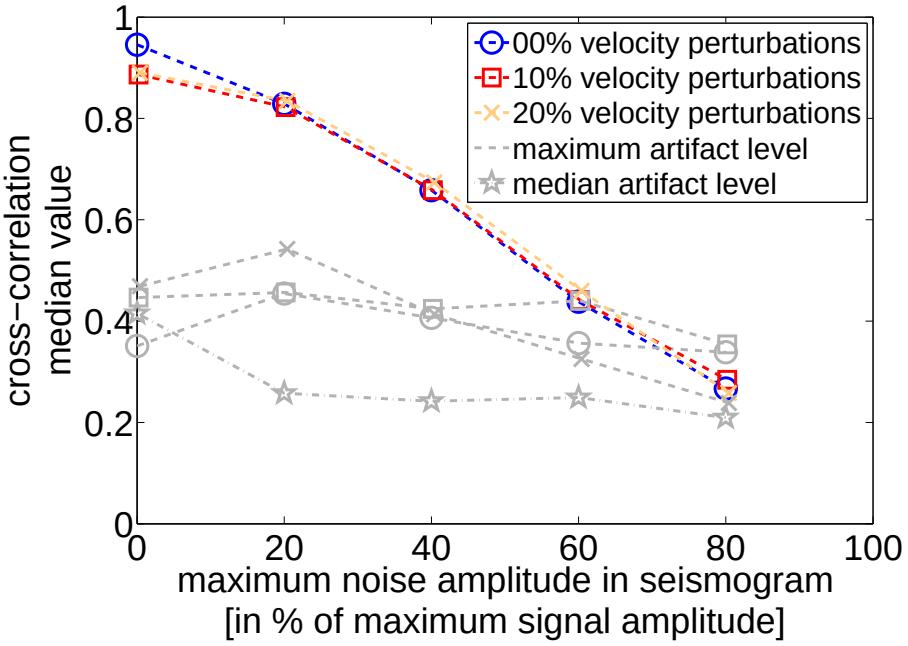

Figure 3.7.: 2D synthetic test of of noise and velocity perturbations: Maximum of all median cross-correlation values over all time windows for different noise amplitudes and velocity perturbations. Symbols in color indicate the maximum value (at the source position), gray symbols indicate the cross-correlation values of artifacts.

results depicted in figure 3.8 show cross-correlation values exhibiting a value of 0.3 concentrated around x=16 km and y=27 km. The maximum median cross-correlation value of 0.97 occurs at x=16.3 km and y=27.5 km, and at a depth of 10.9 km, which is 100 meter more shallow than the original source position but does not differ in a horizontal direction. The relative error (based on the 90% cutoff criterion discussed in section 3.2) is ± 400 meters horizontally and ± 800 vertically.

3.4.3. Location of a M 1.4 earthquake

As a final test of the method, I use the TRI method to locate a cataloged M 1.4 earthquake occurring on the 23th of June, 2010 at 04:27:06 am. Figure 3.9 shows the recorded seismograms filtered between 1 Hz and 5 Hz. Testing the method initially with real earthquake data instead of tremor data has three advantages: first, the SNR is better, second I have a location obtained with ray-tracing methods to use for comparison, and third, the spectra of the earthquake includes lower frequency energy than the tremor data. The longer wavelengths at low frequencies decrease the demands on the accuracy of the velocity model and allow us to potentially constrain how important velocity model inaccuracies may be. Given the lower frequency energy present, I filter the seismograms first between 0.5 Hz and 2 Hz as shown in figure 3.10.

Figure 3.11 shows the median cross-correlation value distribution within the model at

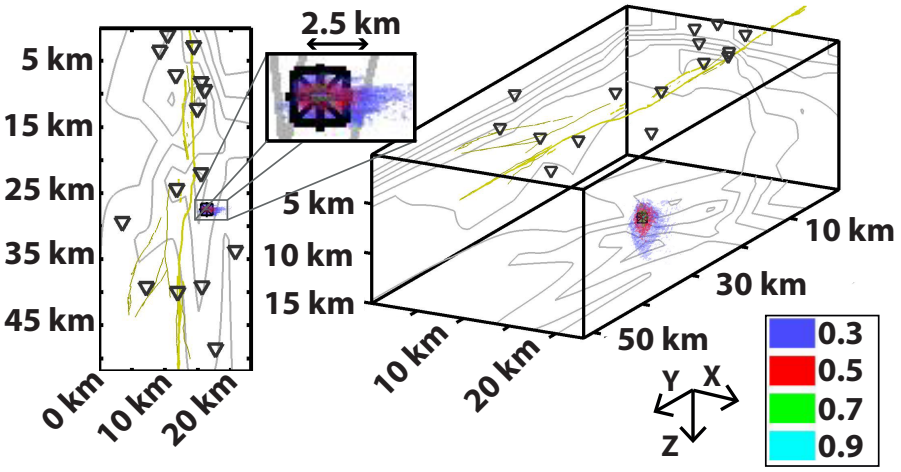

Figure 3.8.: Hypocentral location of a double-couple source using TRI. Color code indicates median cross-correlation value within the model volume. The center of the black square marks the original source position, the black star indicates the retrieved source location. Black triangles denote station positions and the yellow line is the surface trace of the San Andreas Fault.

t=19.0 s, which includes the maximum median cross-correlation value of 0.56. The determined source position is approximately 1 km east of the main San Andreas Fault at X=15.3 km$^{+1.7km}_{-2.1km}$, Y=24.8 km$^{+0.2km}_{-0.8km}$, and 9.9 km$^{+3.4km}_{-3.5km}$ depth, which includes the 1.5 km thickness of the absorbing layer on top of the model. For comparison Käufl (2012) obtained the source location at X=13.33 km $\pm$0.2 km, Y=24.42 km $\pm$ 0.2 km, and 12.4 km $\pm$ 0.1 km in depth by using an 1D velocity model averaged from the 3D model of Thurber et al. (2006) and the program Hypoellipse (Lahr, 1999). Käufl (2012) improved the location result with the program Velest (Kissling et al., 1995) by determining station and velocity model corrections for the 1D model. The improved location at X=10.7 km , Y=24.76 km and 11.5 km depth is denoted in figures 3.11 and 3.13. The difference between the determined source location with the modified TRI method and the Hypoellipse solution is 2 km horizontally and 2.5 km in depth while the difference to the improved location is 4.6 km horizontally and 1.6 km in depth. A possible explanation of the difference while using the same data set is the use of the 3D velocity model in this study, whereas Käufl (2012) used an averaged 1D model, which compensates for the velocity differences on both sides of the San Andreas Fault using station corrections. An additional factor which may cause differences in the hypocentral solution is the elongated station distribution in y-axis direction.

The maximum cross-correlation coefficient of 0.56 obtained using the modified TRI method is lower than that obtained in the synthetic test in section 3.4.2, which could be due to multiple reasons: First, the velocity model may not be accurate enough, second, the SNR may be too low, and third, there might be only a small amount of shear wave energy recorded at some stations due to the geometry of the radiation pattern. The seismograms in figure 3.10 suggest that the second and third factors may not be the cause of

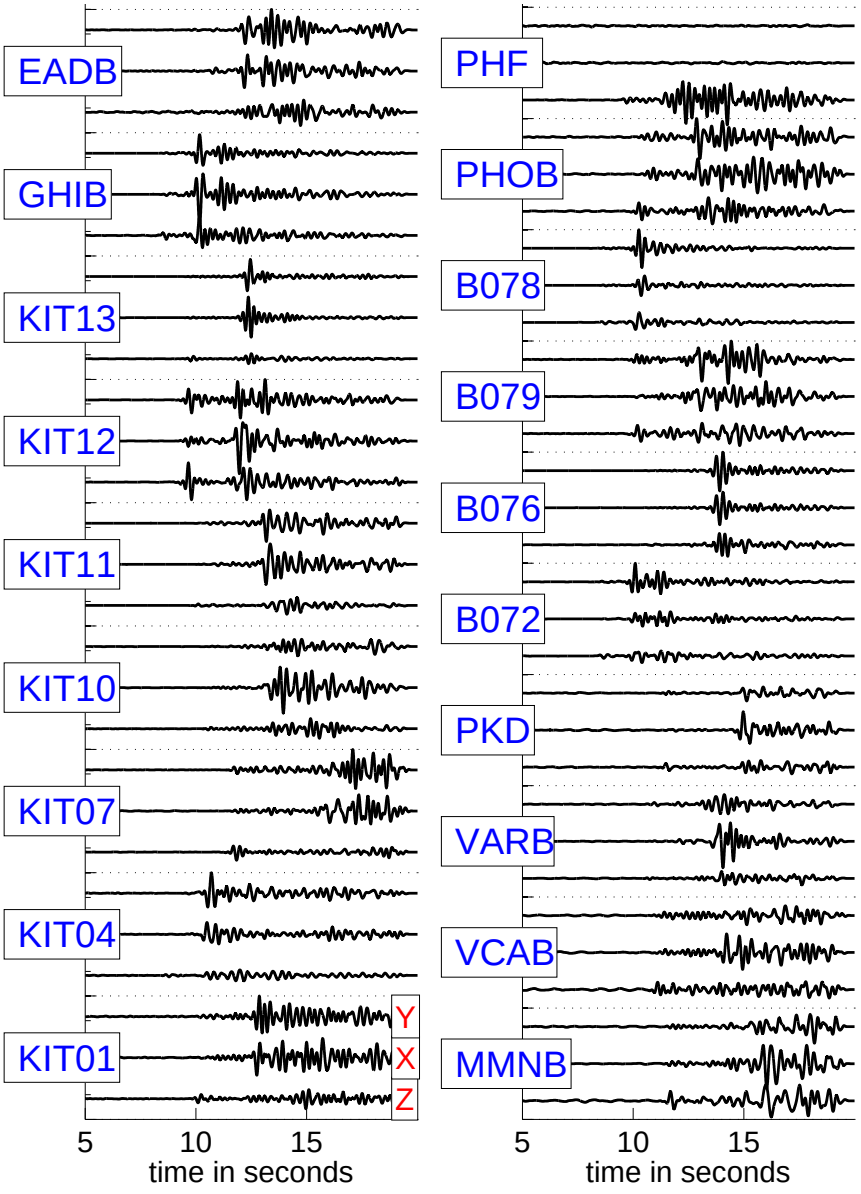

Figure 3.9.: Waveforms of a M 1.4 earthquake recorded at 23th of June, 2010, filtered between 1 and 5 Hz.

the lower cross-correlation coefficient, as there is a clear S-phase visible on each station. In efforts to reduce spurious correlation values resulting from inaccuracies in the velocity model, I taper the S-phases. I determine the S-phase arrival within the seismograms by searching for the maximum vector amplitude on the horizontal components for each station and taper with a three-second long cosine window around the maximum amplitude. Figure 3.10 depicts the tapered waveform in the frequency band of 0.5 Hz to 2 Hz.

The location result using the tapered waveforms (shown in figure A.1 in the appendix A) is nearly identical to that calculated using no tapering, differing by 0.4 km horizontally

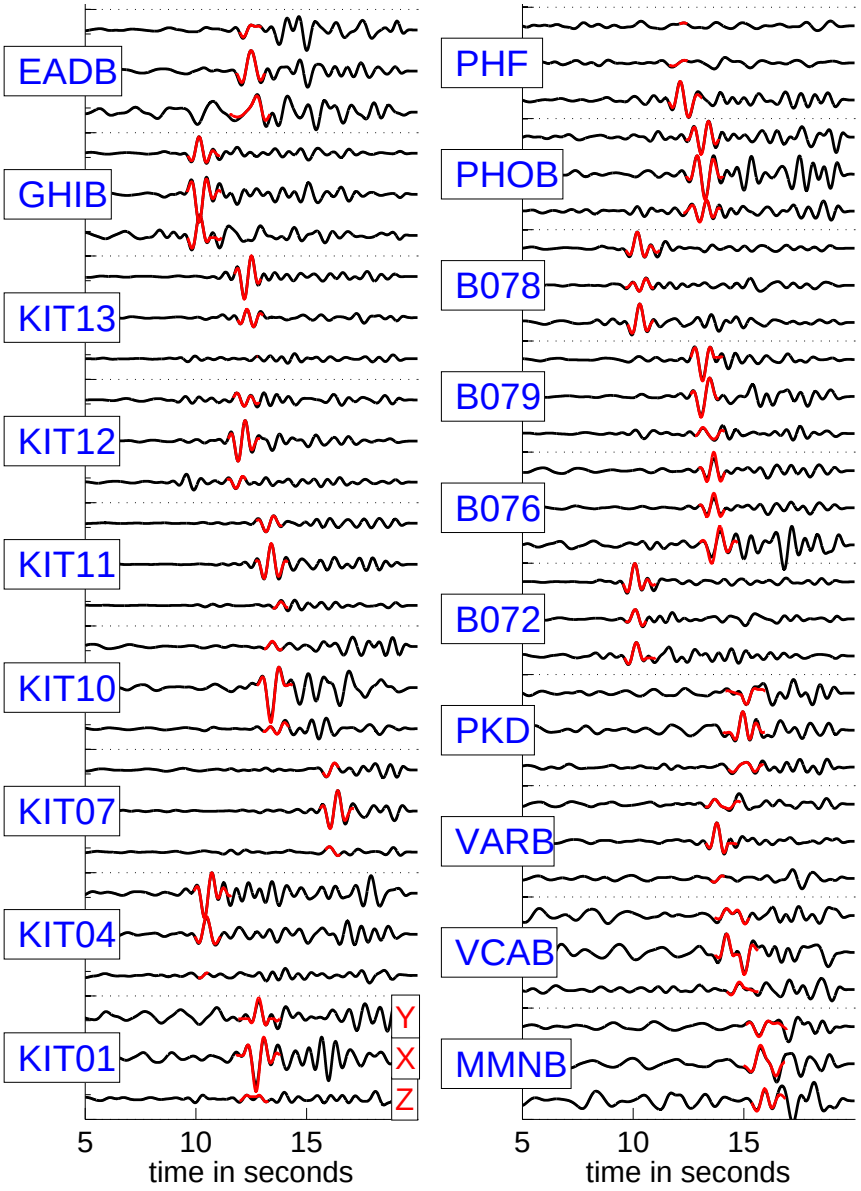

Figure 3.10.: Waveforms of a M 1.4 earthquake recorded at 23th of June, 2010, filtered between 0.5 and 2 Hz. Complete waveforms shown in black, the tapered S-phase signals used in the waveform rebroadcasting are shown in red.

and 1 km vertically. More interesting is the appearance of the curl field functions at the determined source position, i.e., the grid point where the highest cross-correlation value occurs (figure 3.12). The curl field from the S-phases pulses are partially shifted in time, on the order of one wavelength at at the gridpoint with the maximum value. Therefore, the S-wave pulses must be also shifted at other gridpoints. The implications of the maximum cross-correlation values being shifted up to one wavelength are that the velocity model is only spatially accurate to within one wavelength in the 0.5-2 Hz frequency band (e.g., the

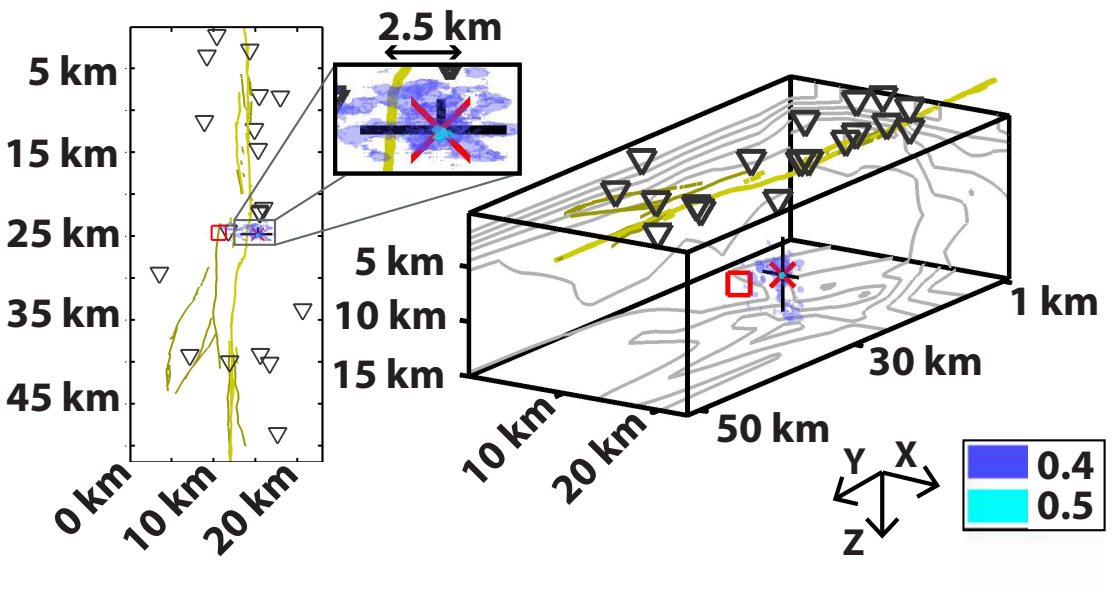

Figure 3.11.: Hypocentral location of a M 1.4 earthquake determined using seismograms shown in figure 3.10, filtered between 0.5-2 Hz. Color code indicates the median cross-correlation values within the model volume. The center of the red square marks the solution of Käufl (2012) for comparison, the black star indicates the retrieved TRI source location. Black lines show the determined error range. Black triangles denote station positions and the yellow line indicates the surface trace of the San Andreas Fault.

wavelength for a wave with 2Hz dominant frequency traveling at 4 km/s implies that the location accuracy will not be less than 2 km for the particular source region and receiver distribution).

I look now at the earthquake location in the 1-5 Hz frequency band, since it is the interesting frequency band for tremor localization. Figure 3.13A shows the median curl field cross-correlation value distribution at t=16.6 s (the source time). The maximum value of 0.3 occurs at X=14.8 km$^{+4.8km}_{-7.5km}$, Y=23.6 km$^{+1.9km}_{-1.6km}$, and 7.7 km$^{+4.1km}_{-3.7km}$ depth, different by 1.55 km horizontally from the previous location in the lower frequency band. The uncertainty in the location increased by factor of approximately 3, however, the extent of the errorbars encompasses the previous location. The increased errors are expected, as the higher frequencies and thus the shorter wavelengths contribute to location inaccuracy. Consequently, the maximum median cross-correlation coefficient decreases to 0.3, as the defocussing is up to multiple wavelengths in the new frequency band.

If I calculate the location using only the tapered S-phase, the result improves significantly. Figure 3.13B shows the median curl field cross-correlation values, this time at t=12.3s. The overall maximum of 0.26 occurs at t=16.7 s, similar to the untapered case. However the snapshot at t= 17.3 s better represents the median cross-correlation value distribution of the high values close to the global maximum, and so I therefore use it for illustration purposes. The determined source position is at X=14.6 km$^{+1.4km}_{-2.3km}$,

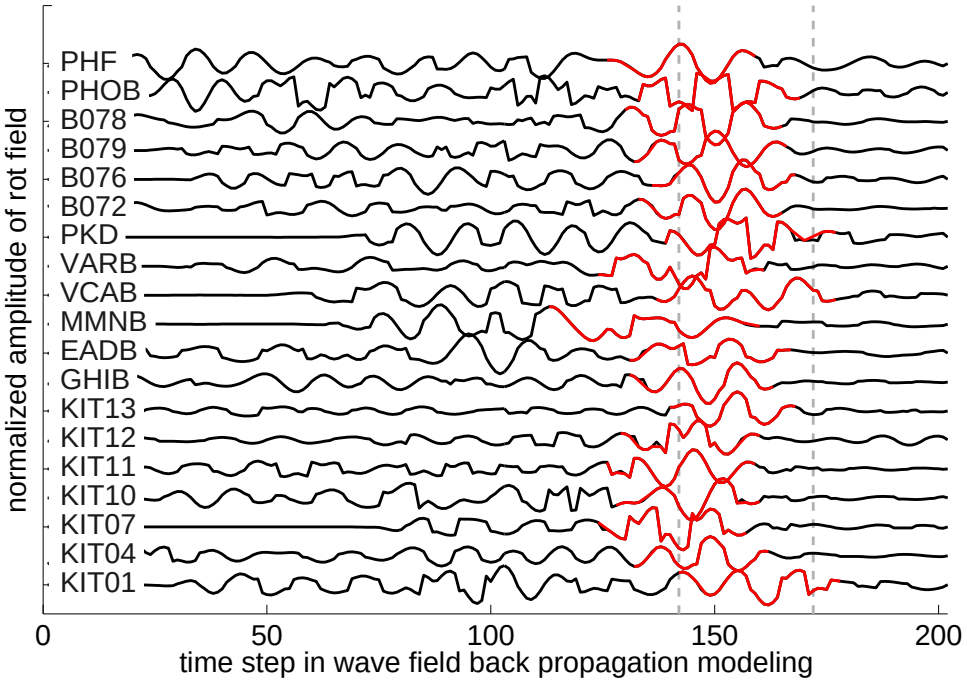

Figure 3.12.: Functions of the curl field at gridpoint X=15.3km, Y=24.8km and 9.8km depth for the seismograms shown in figure 3.10. The gray dashed line denotes the position of the time window with the maximum median cross-correlation coefficient. Red indicates the position of the separate rebroadcasted tapered S-phase. Note the shifted positions of the S-phase pulses.

Y=25.2 km$^{+0.5km}_{-0.3km}$, and 8.2 km$^{+2.6km}_{-0.4km}$ depth, which is in good agreement with the determined location in the lower frequency band. Thus, by tapering around the S-phase I reduce the volume with high cross-correlation coefficients which may result from velocity model inaccuracies or the presence of S-wave coda in the untapered waveforms. Please note, that a more accurate velocity model would increase the maximum cross-correlation coefficient at the source position to values significantly higher than the artifact values (see section 3.4.1) and thus, the tapering around the S-phase would be unnecessary. The functions of the curl field at the source position for the frequency band of 1-5 Hz are shown in figure A.2 in appendix A.

Finally, figure 3.14 summarizes the earthquake location result in time for the four calculated cases: both the tapered and untapered cases in the 0.5-2 Hz, and the 1-5 Hz frequency bands. The figure clearly shows the decrease of the maximum median cross-correlation value in the higher frequency band as well as the stable position of the maximum in consecutive time steps of approximately 5 seconds. The time period of 5 seconds of the stable position partly arises from the moving time window of the cross-correlation of the curl field functions. The time window with a length of 1.5 seconds covers a short signal up to 3 seconds, thus the remaining 2 seconds of the stable position arises from the temporally extended source signal, which demonstrate the advantage of the modified TRI method over the 'classical' TRI method. The modified TRI method includes the phase

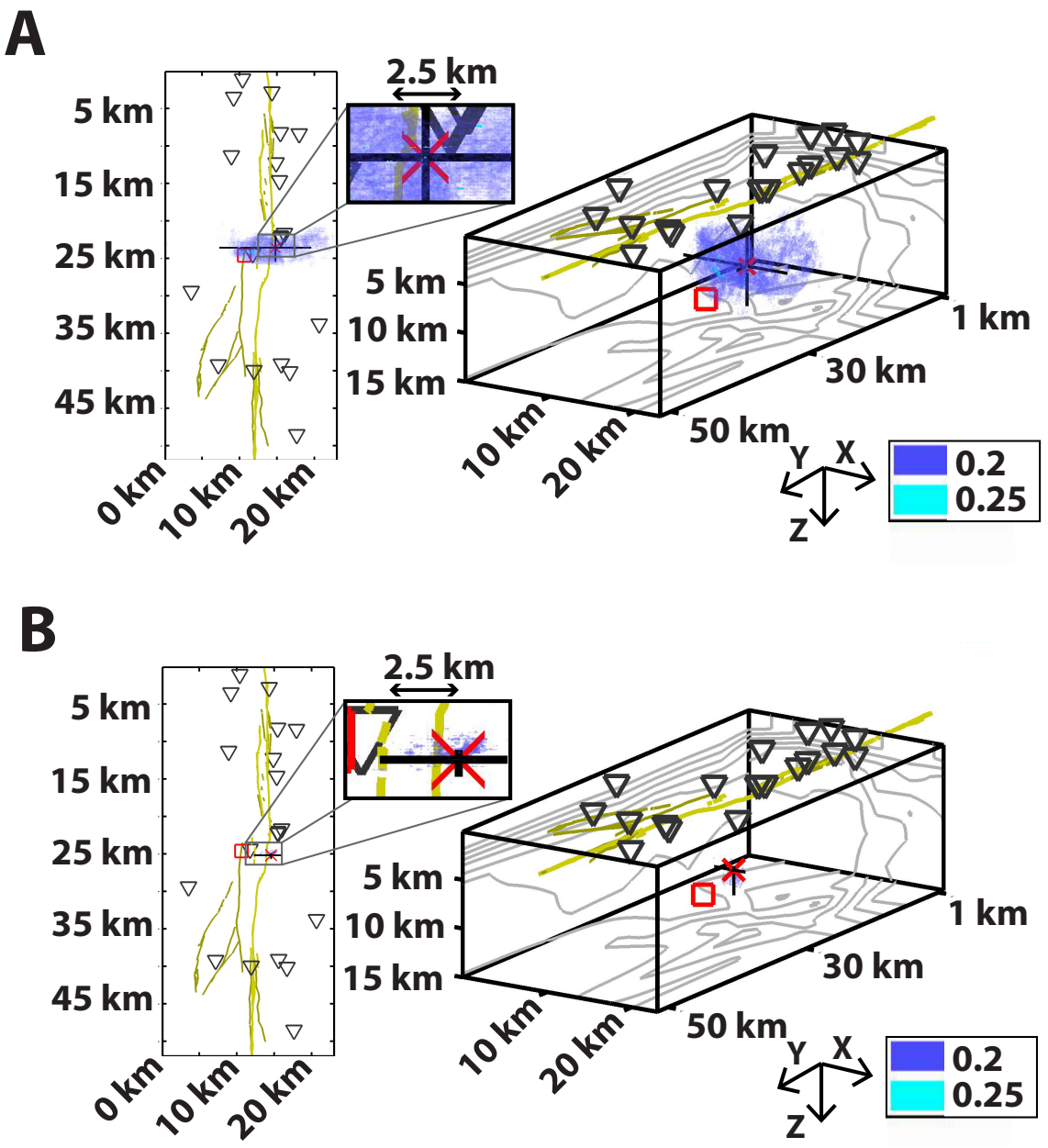

Figure 3.13.: Hypocentral location of a M 1.4 earthquake in the frequency band of 1 Hz to 5 Hz using the complete seismograms (A) and using the tapered S-phase only (B) (figure A.1 in the appendix A)). The color code indicates the median cross-correlation value of the curl field within the model volume. The center of the red square marks the solution of Käufl (2012) for comparison, the red star indicates the source location calculated here. The black lines show the estimated error range. Black triangles denote station positions and the yellow lines indicate the San Andreas Fault surface trace.

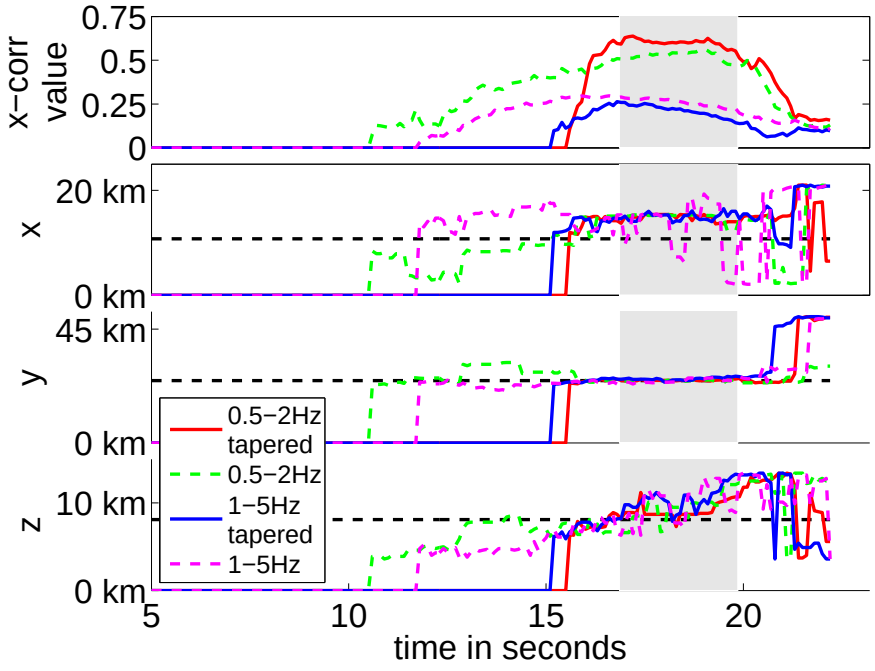

Figure 3.14.: Temporal progression of the curl field cross correlation values (top) and the corresponding implied source location (bottom three panels) of the M 1.4 earthquake. Colored lines indicate two varying frequency bands and the tapered (solid lines) vs. untapered waveforms (dashed lines). The upper panel denotes the maximum median cross-correlation value and the lower three panels show the position of the maximum within each time step. Black dashed lines and the gray box indicate the location of Käufl (2012) for comparison. The middle two panels indicate a stable horizontal position of the maximum correlation value in time.

information over a certain time period instead of only using the information of individual time steps in 'classical' TRI methods, which makes the modified TRI more robust in source localization.

3.4.4. Location of a LFE event within a tremor episode

The previous section showed the ability of the modified TRI method to locate an recorded M 1.4 earthquake, but also illustrated the inaccuracy of the velocity model used for the rebroadcasting. The inaccuracy of the velocity model limits the precision of the location result especially in the frequency band of 1-5 Hz, where tremor has its main energy. To account for the limitations of the velocity model, I tapered a 3 second long cosine window around around the S-phase of the earthquake, which improved the location result significantly.

In this section I apply the modified TRI method to a LFE within a tremor episode. The low SNR of tremor makes the localization more challenging than the localization of an

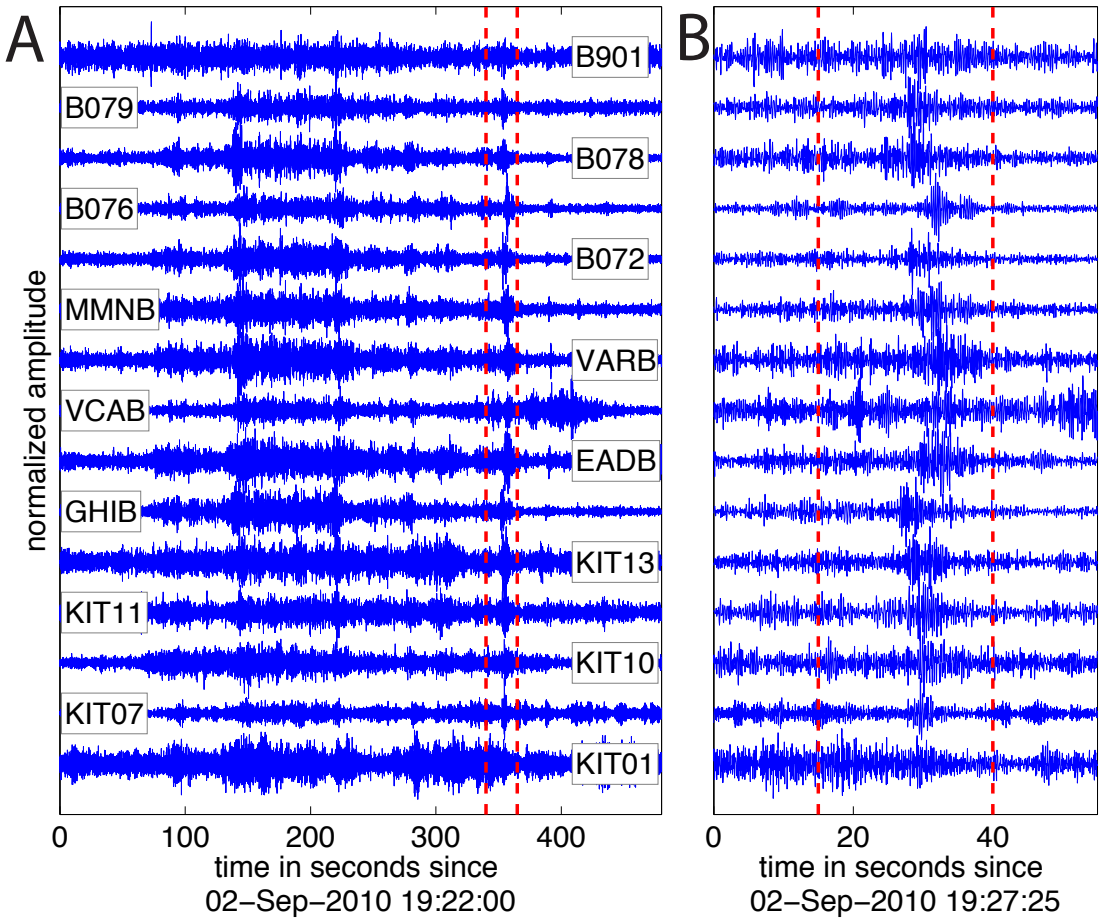

Figure 3.15.: Tremor episode recorded at 2nd of September, 2010, filtered between 1 and 5 Hz. Panel A shows the north component of the complete tremor episode. The 25s long time window chosen for rebroadcasting is denoted by the red dashed lines. Panel B shows the magnified detail around the time window which includes a LFE event.

earthquake. Furthermore, the increased depths of the source locations entail longer travel paths where velocity values may be less accurate, and lead to a worse source-receiver geometry.

Figure 3.15A shows a tremor episode recorded on the 2nd of September 2010. A 25 s long time window around a LFE at the end of the episode is indicated by red dashed lines. The waveforms of the LFE are shown magnified in Panel B. Please note the figure shows the waveform of only 15 selected stations. Other stations were neglected in the analysis due to data gaps and poor SNR. Before rebroadcasting to the subsurface I tapered the waveforms around the maximum value, or the most probable value of the S-phase of the LFE. Due to the poor SNR of tremor at most of the stations, a visual inspection of the automatically determined tapering window is necessary. In some cases the tapering window has to be moved to another position, if a transient noise burst causes the maximum amplitude. The

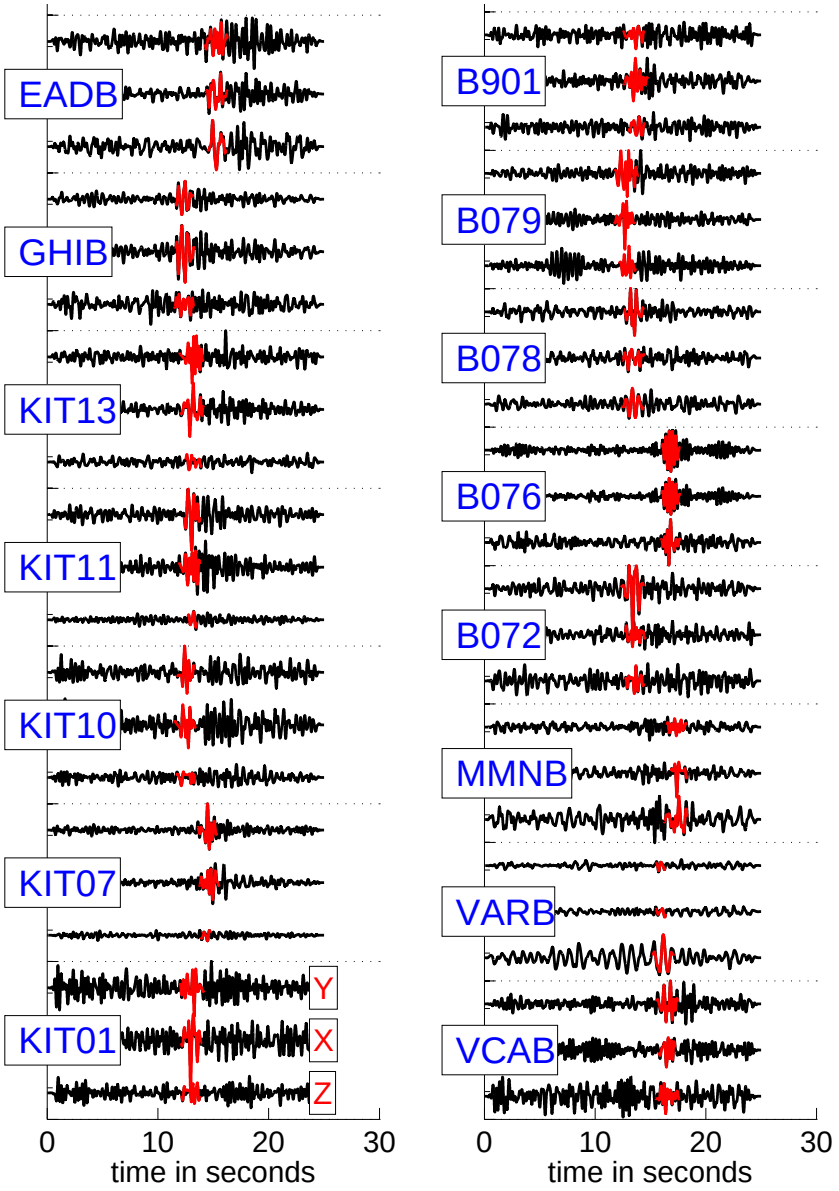

Figure 3.16.: Waveforms of a LFE event recorded at 2nd of September, 2010, filtered between 1 and 5 Hz. Complete waveforms shown in black, the tapered S-phase signals used in the waveform rebroadcasting shown in red. The time window is indicated in the tremor episode shown in figure 3.15 by red dashed lines.

waveforms of all components as well as the tapered waveforms are shown in figure 3.16. The tapered phases used for rebroadcasting are shown in red.

The hypocentral location result is shown in figure 3.17. The red star marks the calculated source location, the black lines denote the errorbars. The black triangles show the station distribution and the yellow lines indicate the San Andreas Fault surface trace. The determined source location is at X=11.7 km$^{+4.3km}_{-3.7km}$, Y=33.3 km$^{+1.5km}_{-0.6km}$, and 22.8 km$^{+1.8km}_{-5.7km}$

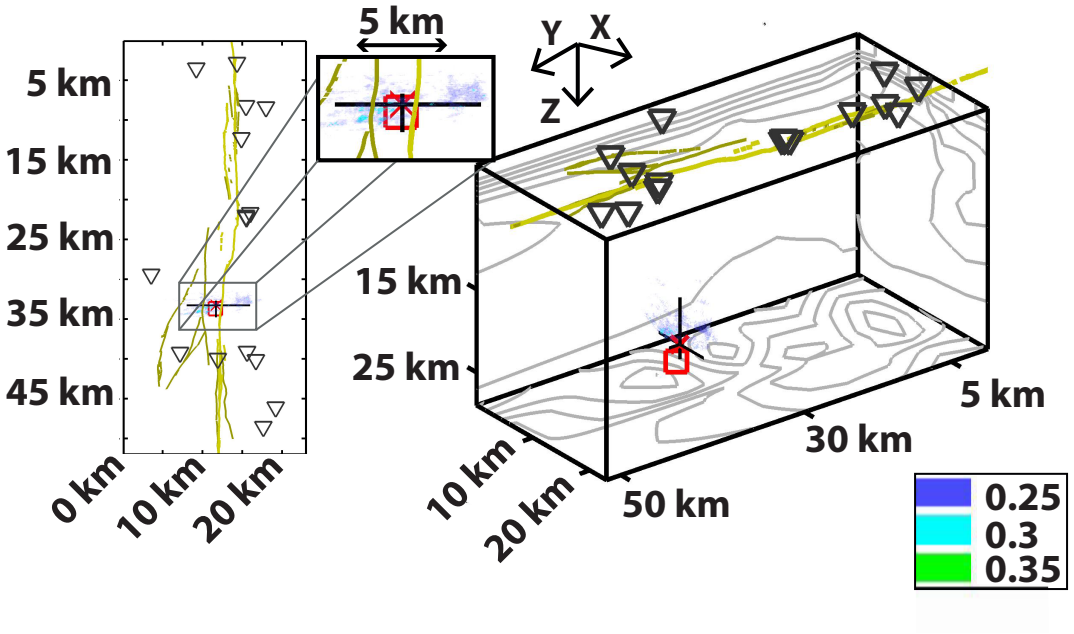

Figure 3.17.: Hypocentral location of a LFE event within a tremor episode in the frequency band of 1 Hz to 5 Hz using the tapered S-phase only. The waveforms of the tremor episode are shown in figure 3.15 and the waveforms used for rebroadcasting are shown in figure 3.16. The color code indicates the median cross-correlation value of the curl field within the model volume. The center of the red square marks the solution of Shelly and Hardebeck (2010) for comparison, the red star indicates the source location calculated here. The black lines show the estimated error range. Black triangles denote station positions and the yellow lines indicate the San Andreas Fault surface trace.

depth, which includes the 1.5 km thickness of the absorbing layer on top of the model. The maximum median cross-correlation value of 0.4 is about 0.1 higher than the maximum median cross-correlation value of the located M 1.4 earthquake in the 1-5 Hz frequency band described in section 3.4.3, likely due to the different number of stations used: while for the localization of the M 1.4 earthquake in section 3.4.3 19 stations are used, only 15 stations could be used for the localization of the LFE event. The relationship between number of stations and the maximum median cross-correlation coefficient is determined in more detail in figure 3.21 in section 3.4.6. The errorbars in figure 3.17 are twice as large compared to the errorbars of the location result of the earthquake in figure 3.13B). Possible explanations are the greater depth of the LFE event (resulting in longer travel paths), or a lower SNR within the seismograms.

We compare the determined source location with the results of Shelly and Hardebeck (2010). Shelly and Hardebeck (2010) stacked up to 400 individual LFE's from a LFE

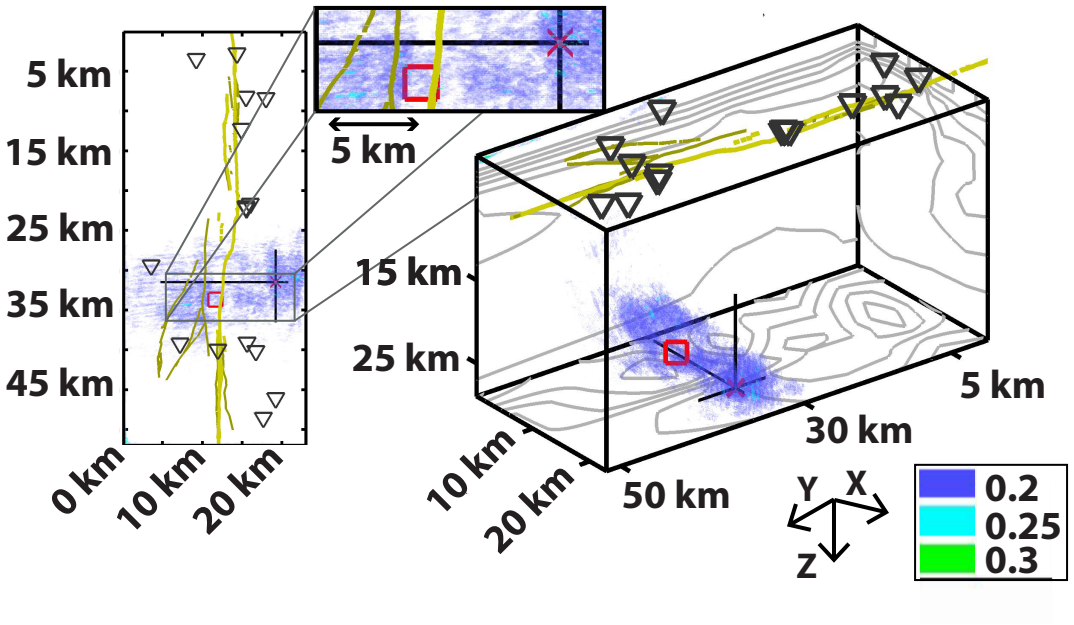

Figure 3.18.: Hypocentral location of a LFE event within a tremor episode in the frequency band of 1 Hz to 5 Hz without tapering. The waveforms of the tremor episode are shown in figure 3.15 and the waveforms used for rebroadcasting are shown in figure 3.16. The color code indicates the median cross-correlation value of the curl field within the model volume. The center of the red square marks the solution of Shelly and Hardebeck (2010) for comparison, the red star indicates the source location calculated here. The black lines show the estimated error range. Black triangles denote station positions and the yellow lines indicate the San Andreas Fault surface trace.

event family to obtain P and S-phase picks and used them to locate the LFE event family with triangulation. Thus, a direct comparison of both methods is inappropriate as the TRI method locates individual LFE's. However, the stacked LFE family location can serve as a reference point. The stacked LFE event family source location of Shelly and Hardebeck (2010) at X=11.63 km, Y=33.71, and 24.75 km depth (including the thickness of the absorbing layer on top of the model) is indicated by a red square in figure 3.17. The difference between both locations is 0.4 km horizontally and 2 km vertically.

A detailed look at the distribution of the median cross-correlation value in the figure 3.17 reveals mainly two spots with relatively high cross-correlation values that are extended in the x-direction across the fault and causing the large uncertainty in the x-direction. Once again, for a accurate velocity model one would assume high median cross-correlation values centered around only one maximum as it is the case in the synthetic test with a double couple source in section 3.4.2. Thus, the two regions with

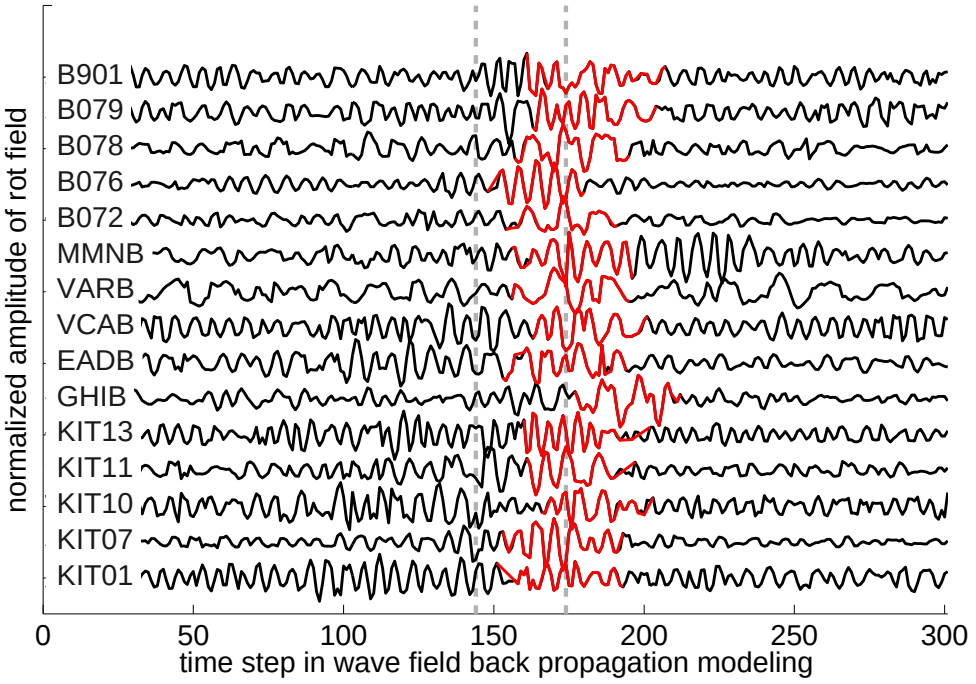

Figure 3.19.: Functions of the curl field at gridpoint X=11.7km, Y=33.3km and 22.8km depth for the seismograms shown in figure 3.16. Red indicates the position of the separate rebroadcasted tapered S-phase. The gray dashed line denotes the position of the time window with the maximum median cross-correlation coefficient for the rebroadcasted tapered S-phase.

high median cross-correlation values evidence the inaccuracy of the velocity model under the assumption that the tapering windows are applied accurately. If we rebroadcast the complete tremor waveforms without tapering around the LFE event the error range is increased by a factor of 2 to 3 as it is also observed in the localization of the M 1.4 earthquake in the frequency band of 1-5Hz (see figure 3.13). The location result for the rebroadcasted complete waveforms is shown in figure 3.18. The determined source position is X=19.2 km$^{+1.6km}_{-14.5km}$, Y=31.5 km$^{+5.1km}_{-4.1km}$, and 26.7 km$^{+0.6km}_{-11.3km}$ depth, with a maximum median cross-correlation coefficient of 0.33 at T=18.1s. The error range covers the source position obtained with the tapered waveforms.

Figure 3.19 shows the source functions at gridpoint X=11.7 km, Y=33.3 km and 22.8 km depth, which is the source location indicated by the tapered waveforms. Red lines indicate the source functions of the tapered waveforms, the gray dashed lines denote the position of the time window where the maximum median cross-correlation coefficient of 0.40 occurs. The source functions of the complete waveforms are shown in black for illustration purposes.

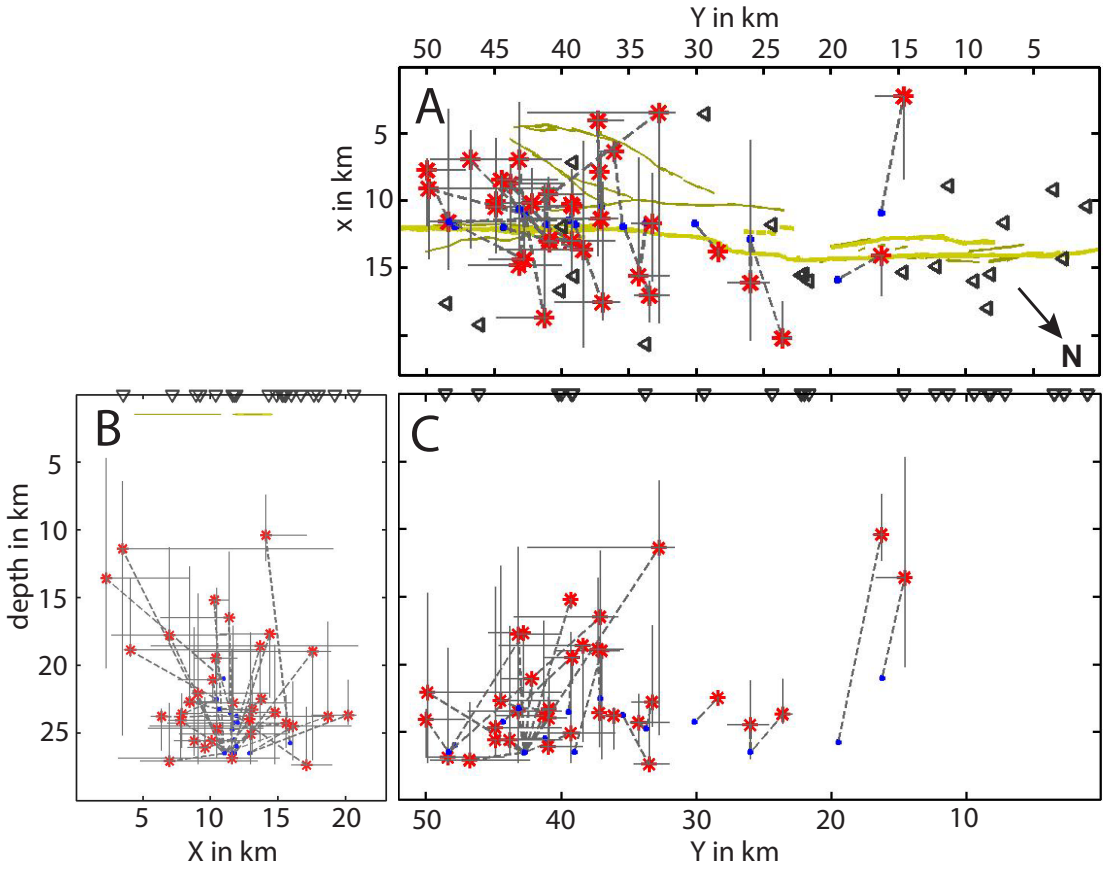

Figure 3.20.: Hypocentral location of 35 LFE using the tapered S-phase only. Panel A shows the plain view, panel B displays the vertical section in the X-axis and depth section, and panel C shows the vertical section in the Y-axis and depth section. The red stars indicate the determined source position, black lines show the estimated error range. The small red dots mark the solution of Shelly and Hardebeck (2010) for comparison and are connected with a gray dashed line to the source positions determined here. Black triangles denote all possible station positions and the yellow lines indicate the San Andreas Fault surface trace. Please note, that the stations and number of stations used is different for each LFE and therefore the individual station configuration of each localization is not shown here. Furthermore, the depth axis includes the thickness of the absorbing layer of 1.5km. The direction to north is indicated by the black arrow in panel A.

3.4.5. Location of multiple LFE events

I apply the modified TRI method with tapering of the S-phases to 35 LFE's from the catalog of Shelly and Hardebeck (2010). The restricted number is caused by the limitation of the computational time of the modified TRI method. The selection of the events is based on two criteria: first, the LFE must have visibly higher amplitude on all stations

	start of time window	X (km)	Y (km)	Z (km)	Latitude (deg. N)	Longitude (deg. W)	hor. diff. (km)	vert. diff. (km)
1	2010-07-01 17:42:50	$17.60^{+1.3}_{-9}$	$37.00^{+3.5}_{-1.3}$	19.00^{+8}_{0}	35.743	-120.221	6.11	-7.50
2	2010-07-01 17:42:50	$17.60^{+1.3}_{-9}$	$37.00^{+3.5}_{-1.3}$	19.00^{+8}_{0}	35.743	-120.221	6.11	-7.50
3	2010-07-02 04:42:45	$16.10^{+4.3}_{-10.6}$	$26.00^{+1.7}_{-1.4}$	$24.50^{+2.5}_{-3.3}$	35.809	-120.313	3.20	-2.00
4	2010-07-02 13:59:20	$6.40^{+0.4}_{-0.8}$	$36.10^{+1.1}_{-0.3}$	$23.80^{+2.5}_{-0.6}$	35.683	-120.322	5.57	0.05
5	2010-07-03 08:21:15	$13.60^{+5.2}_{-1.9}$	$39.00^{+1.3}_{-1.3}$	$20.60^{+1.3}_{-2.2}$	35.706	-120.240	5.55	-3.65
6	2010-07-04 11:08:35	$15.60^{+0.2}_{-8.8}$	$34.30^{+0.6}_{-2.3}$	$24.30^{+1.8}_{-2.1}$	35.750	-120.257	4.02	-0.45
7	2010-08-04 10:32:05	$8.80^{+3.6}_{-1.5}$	$43.80^{+0.8}_{-3.9}$	$25.60^{+1.1}_{-8.4}$	35.645	-120.246	3.97	0.10
8	2010-08-04 10:40:00	$10.10^{+0}_{-0.1}$	$44.90^{+0.3}_{-0.1}$	$25.60^{+0.4}_{0}$	35.645	-120.227	2.37	-0.90
9	2010-08-06 00:35:25	$14.40^{+0}_{-3.7}$	$42.80^{+2.6}_{0}$	$17.70^{+4.7}_{0}$	35.685	-120.206	6.20	-8.80
10	2010-08-06 00:35:45	$11.60^{+3.5}_{-8.4}$	$48.40^{+1.5}_{-4.2}$	$26.90^{+0.4}_{-8.1}$	35.630	-120.189	0.60	0.90
11	2010-09-02 10:31:40	$7.00^{+6.5}_{-2.2}$	$46.80^{+2.9}_{-4.5}$	$27.10^{+0.2}_{-4.3}$	35.614	-120.239	5.73	0.60
12	2010-09-02 17:32:40	$7.90^{+1.5}_{-0.1}$	$37.20^{+0.3}_{-0.3}$	$23.60^{+2.5}_{-1.5}$	35.685	-120.301	2.58	1.10
13	2010-09-02 19:27:40	$11.70^{+4.3}_{-3.7}$	$33.30^{+1.5}_{-0.6}$	$22.80^{+1.8}_{-5.7}$	35.733	-120.297	0.42	-1.95
14	2010-09-10 02:29:05	$12.90^{+0.1}_{0}$	$40.90^{+0}_{-1.3}$	$24.00^{+0}_{-1.2}$	35.689	-120.232	2.61	-2.50
15	2010-10-09 08:52:50	$18.70^{+0.4}_{-10}$	$41.30^{+3.5}_{-0.4}$	$23.80^{+0.2}_{-7}$	35.720	-120.181	7.80	-2.70
16	2010-10-12 12:51:45	$13.80^{+0.4}_{-0.3}$	$28.40^{+0.1}_{-0.1}$	$22.50^{+0.3}_{-0.1}$	35.779	-120.315	2.70	-1.75
17	2010-10-12 21:07:45	$3.50^{+15.6}_{-0.3}$	$32.80^{+9.7}_{-1.2}$	$11.40^{+13.8}_{-5}$	35.689	-120.370	12.46	-15.10
18	2010-10-12 21:07:50	$10.30^{+1.1}_{-0.3}$	$39.30^{+0.1}_{-0.1}$	$15.20^{+0.7}_{0}$	35.684	-120.266	3.50	-11.30
19	2010-10-22 14:31:30	$20.20^{+0.6}_{-2.7}$	$23.60^{+0.1}_{-0.7}$	$23.70^{+0.7}_{-2.6}$	35.849	-120.296	7.69	-2.80
20	2010-10-26 12:17:15	$4.10^{+10}_{-0.5}$	$37.30^{+0.6}_{-1.9}$	$18.90^{+0.5}_{-5.3}$	35.662	-120.332	6.38	-3.60
21	2010-11-07 02:45:45	$11.40^{+0}_{-5.1}$	$37.10^{+6.4}_{-1.3}$	$16.50^{+6.3}_{-4.9}$	35.706	-120.272	11.23	-10.00
22	2010-11-16 08:54:10	$14.80^{+0.2}_{-5.5}$	$43.20^{+3.7}_{-3.2}$	$23.50^{+3.8}_{-5}$	35.684	-120.200	3.80	-3.00
23	2010-11-17 10:51:25	17.10^{+2}_{-1}	$33.50^{+1.2}_{-1.4}$	$27.40^{+0.1}_{-4.2}$	35.764	-120.251	5.52	3.65
24	2010-11-17 10:57:55	$9.60^{+0}_{-1.3}$	$41.00^{+0.5}_{-2.6}$	$26.10^{+0.4}_{-3.7}$	35.669	-120.259	2.18	0.60
25	2010-11-24 11:26:15	14.10^{+3}_{0}	$16.30^{+0.6}_{-0.2}$	$10.40^{+1.9}_{-3}$	35.863	-120.400	3.66	-15.35
26	2010-12-01 12:36:10	$10.50^{+3.4}_{-5.1}$	$44.90^{+0.7}_{-4.9}$	$24.70^{+2.2}_{-10.4}$	35.647	-120.224	2.24	-1.80
27	2010-12-01 12:39:15	$13.00^{+2.7}_{-5.3}$	$39.30^{+2.4}_{-3.3}$	$25.10^{+2.2}_{-7.5}$	35.700	-120.243	3.95	-1.40
28	2010-12-28 14:46:35	$13.10^{+0.3}_{-1.9}$	$40.90^{+0.5}_{-0.5}$	$23.30^{+3.3}_{-2.5}$	35.690	-120.231	3.31	0.05
29	2010-12-28 22:27:55	$8.50^{+2.1}_{-0.4}$	$44.50^{+0.3}_{-4.2}$	$22.70^{+0.1}_{-10}$	35.638	-120.243	2.56	-0.55
30	2011-01-03 03:45:00	$2.30^{+6.1}_{0}$	$14.60^{+2.1}_{0}$	$13.60^{+6.6}_{-8.9}$	35.805	-120.512	8.80	-7.40
31	2011-01-23 19:41:20	$10.20^{+0.7}_{-2.6}$	$42.20^{+2.3}_{0}$	$21.10^{+1.5}_{-0.1}$	35.664	-120.246	0.98	-5.40
32	2011-02-03 01:42:45	$7.80^{+4.1}_{-1.3}$	$50.00^{+0}_{-2.9}$	$24.10^{+2.8}_{-1.4}$	35.597	-120.210	4.14	-2.40
33	2011-03-12 07:41:25	$9.10^{+5.2}_{-0.5}$	$49.90^{+0}_{-9.9}$	$22.10^{+5.2}_{-7.4}$	35.605	-120.199	7.43	-4.40
34	2011-04-04 21:05:55	$7.00^{+4.2}_{-4.3}$	$43.20^{+0.1}_{-3.2}$	$17.80^{+0.7}_{-6.5}$	35.638	-120.265	4.06	-8.70

Table 3.1.: Determined source location of LFE's with estimated error range in the local grid coordinate system X,Y, and Z, and the corresponding latitude and longitude values. Additionally the horizontal and vertical difference to the stacked LFE family source locations of Shelly and Hardebeck (2010) are denoted.

that are used for the rebroadcasting so that the S-wave taper can be applied without ambiguity. I assume a high median cross-correlation coefficient in the catalog of Shelly and Hardebeck (2010) to be a proxy for a good SNR and search only for events with a median cross-correlation coefficient > 0.5. Second, I want to locate LFE's occurring throughout the complete time span of the dataset, therefore I choose LFE's based on the temporal occurrence to account for different noise conditions at stations and data availability .

The values of the location results are listed in table 3.1 and the determined source

locations are visualized in figure 3.20. Panel A shows the plain view, panel B displays the vertical section in the X-axis and depth section, and panel C shows the vertical section in the Y-axis and depth section. The red stars indicate the determined source position, black lines show the estimated error range. For reference, I also show the stacked LFE family locations determined by Shelly and Hardebeck (2010), marked as small red dots in the figure. I connect both solutions with a gray dashed line to illustrate the differences. The yellow lines in panel A indicate the San Andreas Fault surface trace and the black triangles denote all possible station positions. The stations and the number of stations used for the localization of each LFE event is different and depends on the availability of data and the SNR of the LFE in the seismogram. Thus the individual station configuration of each localization is not denoted in the figure. The number of station used is listed in table 3.2.

The determined location of the LFE's are mainly south of Cholame ($Y \geq 32$ km) in a depth between 20km and 27km. The bulk of horizontal uncertainty is mainly in the X-axis direction and the events scatter in the X-direction around the SAF. The median uncertainty amounts to 5 km in the X-direction, 2.6 km in the Y-direction, and 4.8 km in depth. For reference, 18 events out of 30 have a horizontal difference less than 2km to the stacked LFE family source locations of Shelly and Hardebeck (2010) in the y-direction, whereas only 12 events differ less than 2 km in th X-direction. The average median difference in the X-direction amounts to 2.7 km and 1.9 km in the Y-direction. The determination of the depth is for location algorithms difficult due to geometrical reasons. Nevertheless, the depths of the modified TRI method are comparable to the depths of the stacked LFE family locations with a median difference of 2.6 km. In most cases the source locations of the modified TRI method are more shallow than the source locations of Shelly and Hardebeck (2010).

3.4.6. Relationship between location result and parameters

Next, I want to determine how parameters such as the median SNR of the LFE within the seismograms, the number of station used, the maximum gap in azimuthal coverage of the stations, and the distance to the nearest station influence the location result of the modified TRI method. The SNR is calculated here by the maximum signal amplitude divided by the maximum noise amplitude. The quality of the location result is a difficult quantity to assess. Location quality could be measured by a comparison to source locations obtained by different methods, or by the size of the error of the determined source location. Comparing my locations to those estimated by Shelly and Hardebeck (2010) is not an appropriate approach, because they determine locations of event stacks, and I determine the location of individual LFE's. I therefore chose the range of the horizontal uncertainty as a proxy for the quality of the location result. The parameter values are displayed in table 3.2 and depicted in figure 3.21.

Figure 3.21 A)-D) shows the different parameters over the range of horizontal uncertainty. The colored stars denote the values of the localization of an individual LFE. The gray line indicates the best fit and the number in red gives the corresponding coefficient of determination, the R^2 value. The R^2 value is based on the residuals to the best fit line and hence indicates how well the data fits a regression line. A R^2 value of 1 reflects a purely linear relationship whereas a value of 0 indicates a horizontal line as best fit.

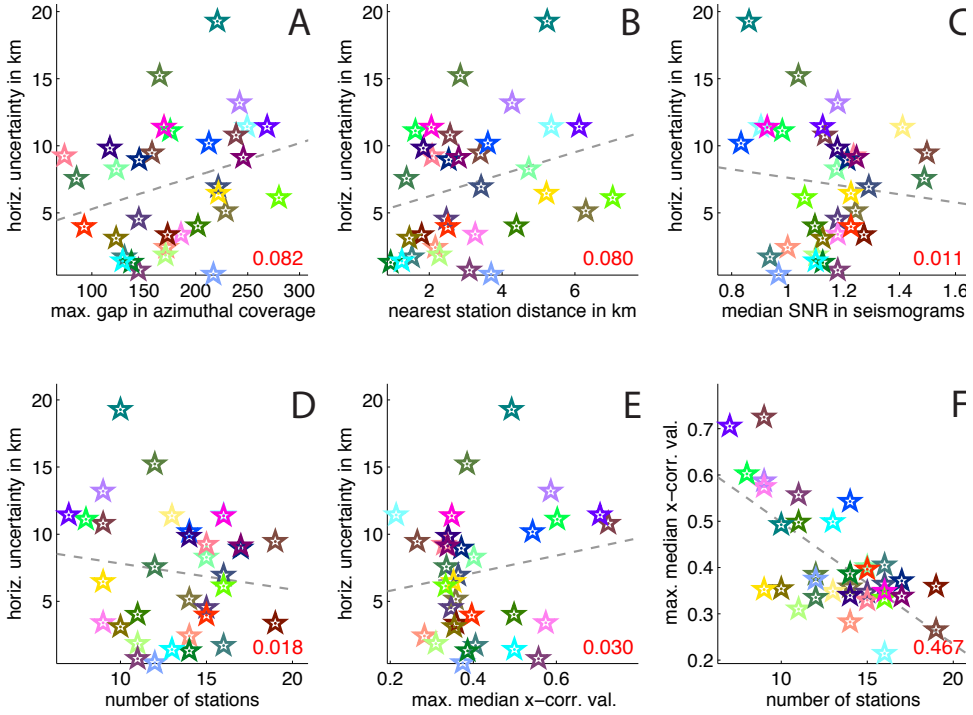

Figure 3.21.: Statistical analysis between the location result and different parameters such as the maximum gap in azimuthal coverage, nearest station distance, median SNR in the seismograms, number of stations used, and the maximum median cross-correlation coefficient in the model. The quality of the location is indicated by the horizontal uncertainty. Stars indicate the values of the localization of individual LFE's shown in figure 3.20. Gray dashed line displays the line of best fit, the red number gives the corresponding coefficient of determination (R^2 value).

Panel A indicates a very weak relationship between the maximum of azimuthal station coverage as the stars seem to scatter around the trend of the line, although, the R^2 value of 0.082 is low. Not surprisingly, the horizontal uncertainty is increasing with an increasing gap.
Panel B shows the influence of source-station distance. The R^2 value of 0.080 indicates a weak trend of short source-receiver distance is decreasing with horizontal uncertainty. However, one must keep in mind that the influence of a single station decreases with the increase of the number of stations.
Panel C suggests that the median SNR of the LFE's in the seismograms, seem to have little effect on the quality of the location result as suggested by the distribution of the stars in panel C and the R^2 value of 0.011. A reason is probably the tapering of the S-phase, which removes the noise outside the tapering window. Nevertheless, one would expect at most only a weak relationship as a strength of the modified TRI method is the search for phase coherence rather than the search for the maximum amplitude within the superposition of the wavefields.

	start of time window	num. of stat.	SNR	azimuth. gap (deg.)	nearest station (km)	max. x-corr. coeff.
1	2010-07-01 17:42:50	13	1.41	110.73	1.5	0.35
2	2010-07-01 17:42:50	16	0.93	110.73	1.5	0.35
3	2010-07-02 04:42:45	12	0.98	133.67	1.5	0.39
4	2010-07-02 13:59:20	11	1.07	179.25	2.1	0.31
5	2010-07-03 08:21:15	12	1.50	103.50	0.3	0.34
6	2010-07-04 11:08:35	19	1.50	120.46	4.6	0.27
7	2010-08-04 10:32:05	16	1.29	189.56	2.2	0.36
8	2010-08-04 10:40:00	12	0.99	218.50	3.8	0.37
9	2010-08-06 00:35:25	15	1.18	180.30	2.9	0.35
10	2010-08-06 00:35:45	9	1.18	245.03	5.7	0.59
11	2010-09-02 10:31:40	16	0.88	234.64	4.7	0.21
12	2010-09-02 17:32:40	16	0.93	112.08	1.8	0.41
13	2010-09-02 19:27:40	15	1.18	125.39	4.4	0.40
14	2010-09-10 02:29:05	14	1.13	129.50	0.7	0.39
15	2010-10-09 08:52:50	8	0.98	151.60	2.7	0.60
16	2010-10-12 12:51:45	11	1.24	145.44	3.1	0.56
17	2010-10-12 21:07:45	10	0.86	113.85	2.2	0.49
18	2010-10-12 21:07:50	13	1.10	128.01	1.0	0.50
19	2010-10-22 14:31:30	9	1.24	176.38	2.5	0.57
20	2010-10-26 12:17:15	9	1.14	147.75	2.2	0.72
21	2010-11-07 02:45:45	15	1.28	148.72	1.2	0.33
22	2010-11-16 08:54:10	17	1.21	177.46	2.4	0.37
23	2010-11-17 10:51:25	15	1.23	97.62	2.2	0.40
24	2010-11-17 10:57:55	19	1.27	157.40	1.4	0.36
25	2010-11-24 11:26:15	10	1.13	156.73	1.3	0.35
26	2010-12-01 12:36:10	14	0.83	199.59	2.6	0.54
27	2010-12-01 12:39:15	14	1.18	116.67	2.8	0.34
28	2010-12-28 14:46:35	14	1.00	178.42	2.7	0.28
29	2010-12-28 22:27:55	14	1.24	211.11	5.0	0.36
30	2011-01-03 03:45:00	9	1.23	201.84	4.0	0.35
31	2011-01-23 19:41:20	11	1.10	215.98	5.4	0.50
32	2011-02-03 01:42:45	16	1.06	268.57	5.8	0.33
33	2011-03-12 07:41:25	7	1.13	203.09	5.0	0.71
34	2011-04-04 21:05:55	17	1.25	240.57	1.7	0.34

Table 3.2.: Number of stations used, median SNR of the LFE's within seismograms, maximum gap in azimuthal station coverage, the distance from the determined source to the nearest station, and maximum median cross-correlation coefficient within the model for each located LFE.

The value distribution in Panel D suggests that the number of stations used does not effect the horizontal error range. With the result indicated by panel A and B one could argue

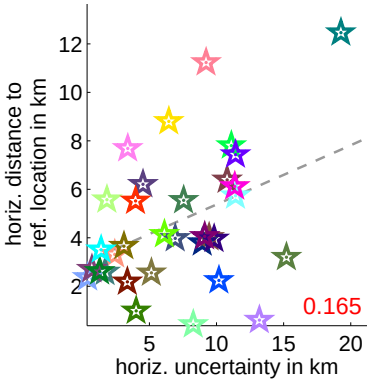

Figure 3.22.: Relationship between horizontal uncertainty and horizontal distance to the solution of Shelly and Hardebeck (2010). Stars indicate the values of the localization of individual LFE's shown in figure 3.20. Gray dashed line displays the line of best fit, the red number gives the corresponding coefficient of determination (R^2 value).

that the distribution of the stations is more important than the number of stations.

Furthermore, I want to determine if the maximum median cross-correlation coefficient is indicative of the location quality and thus panel E) in figure 3.21 plots the the maximum median cross-correlation coefficient against the horizontal uncertainty. The majority of the source locations with different horizontal uncertainty have a maximum median cross-correlation value around 0.4, which results in a low R^2 value of 0.03. Thus, the maximum median cross-correlation coefficient is not eligible as proxy for the quality of the location.

Panel F in figure 3.21 shows a clear relationship between the number of station used and the maximum median cross-correlation coefficient, which is supported by the R^2 value of 0.487. The decrease of the maximum median cross-correlation coefficient with increasing number of stations used is a result of the inaccuracy of the velocity model and or the tapering. The degrees of freedom decrease with an increasing number of stations and it becomes more difficult for the algorithm to find a grid point that optimizes the coherence between all rebroadcasted wavefields.

The low R^2 values evidence that the influence of single parameters on the quality of the location result is only marginal to non-existent. A possible explanation would be that the quality of the location result is dependent on a combination of parameters. Therefore, I determined for each located LFE a summed parameter value P_s which is calculated as $P_s = w_1 * P_1 + w_2 * P_2 + ...w_N * P_N$, where P denotes the parameters and w individual weighting factors between 0 and 1. Moreover, the parameters are normalized to values between 0 and 1 and parameters with a negative expected trend, such as the maximum gap in azimuthal coverage, are calculated as 1-P. Within a grid search I searched for a combination that optimizes the R^2 value. The best result provides weighting factors of 0.3 for the SNR, 0.9 for the gap in azimuthal coverage, 0.5 for the number of stations, and 1 for the minimum station distance. However, the resulting R^2 value of 0.098 is low and in the order of the R^2 values for the maximum gap in azimuthal coverage and nearest

station distance as single parameters. Hence, there is no evidence that a combination of the determined parameters is controlling the quality of the location result.

Other possible reasons that could affect the quality of the location result are the maximum amplitude in the seismograms which determines the position of the tapering window and a velocity model which suffers from a inhomogeneous distribution of inaccuracies.

In figure 3.22 the relationship between horizontal uncertainty and the horizontal distance to the LFE family source locations of Shelly and Hardebeck (2010) is illustrated. The figure indicates that the source locations with smaller horizontal uncertainty tend to better agree with the stacked LFE family source locations of Shelly and Hardebeck (2010). Under the assumption that both values indicate the quality of the source location, the increasing trend with a R^2 value of 0.165 is expected. However, figure 3.20 reveals that a majority of source location are at the edge of the volume marked by the error range. Thus, the trend in figure Shelly and Hardebeck (2010) can be explained by the increasing distance of the maximum cross-correlation value to the median error range position.

3.4.7. Median error range source determination of multiple LFE's

The maximum median cross-correlation value, which determines the source position, scatters in the X-direction around the fault in figure 3.20. Furthermore, figure 3.22 suggests in case of an increasing error range an increase of the distance to the LFE family source solution of Shelly and Hardebeck (2010), which could be explained by the observation that the maximum median position occurs in most cases at the edge of the determined error ranges. Moreover, the range between maximum cross-correlation values is quite small and hence it is debatable how robust the global maximum value is determining the source position or if it is over-interpreting the data.

Therefore, I introduce a different manner to determine the source position. Instead of only considering the global maximum value and hence relying on one value, I now determine the source position by taking multiple high cross-correlation values into account based on the error range estimation. The error range estimation is determined by the positions of all median cross-correlation value maxima exceeding 90% of the global maximum median cross-correlation value. Hence, the source position is now determined as the median of the error extent, rather than a maximum correlation value which varies only marginally to all values exceeding the 90% cutoff.

Figure 3.23 shows the new location results based on the median error extent source determination. Compared to figure 3.20, the locations are more tightly clustered, and centered around the SAF. The median distance to the LFE family source locations of Shelly and Hardebeck (2010) is now 1.9 km in X-direction, 1.1 km in Y-direction, and 3.7 km in depth. The horizontal differences have been decreased significantly, whereas the vertical difference has increased slightly and the locations are now on average more shallow. The determined source position of each individual LFE is denoted in table B.1 in the appendix.

The median error extent source determination has the advantage of being based on multiple values instead using only one value, thus it is expected to be more robust. The increased compactness of the new source locations as well as the decrease of the horizontal

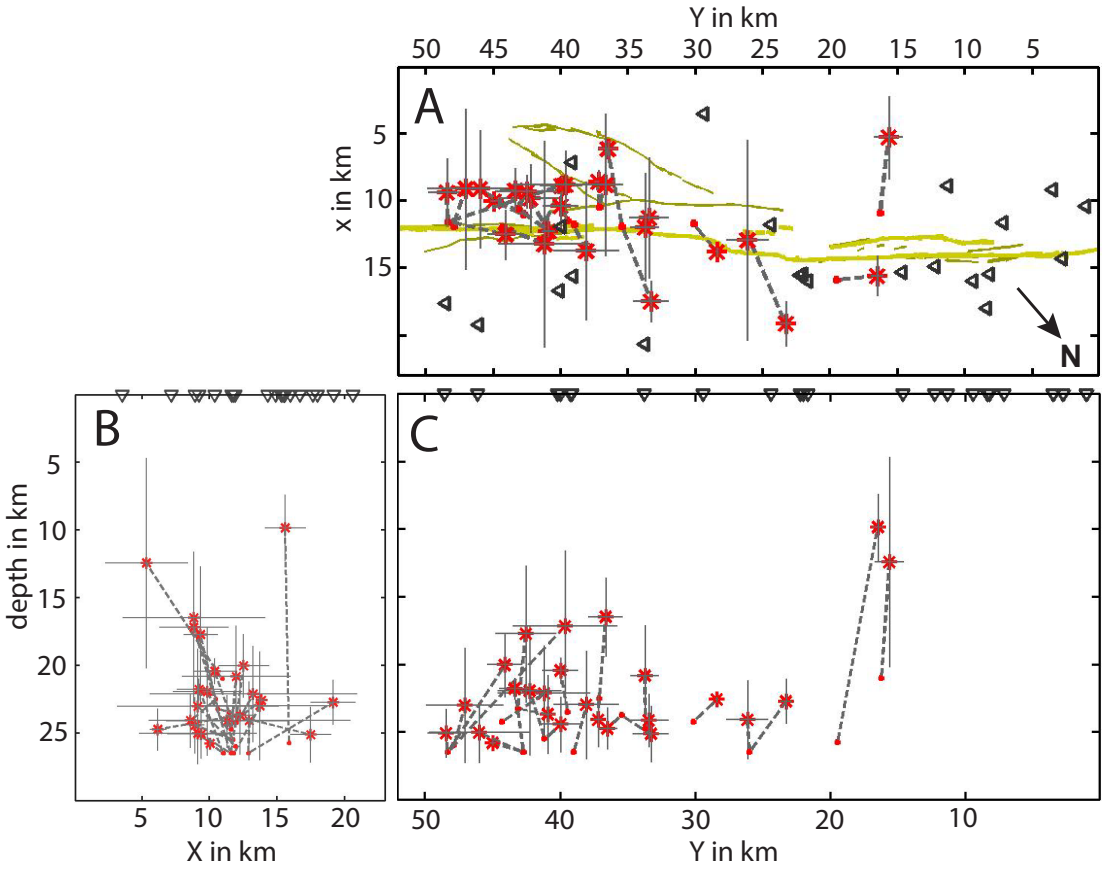

Figure 3.23.: Hypocentral location of 35 LFE's determined by the median error range using the tapered S-phase only. Panel A shows the plain view, panel B displays the vertical section in the X-axis and depth section, and panel C shows the vertical section in the Y-axis and depth section. The red stars indicate the determined source position, black lines show the estimated error range. The small red dots mark the stacked LFE family solution of Shelly and Hardebeck (2010) for reference and are connected with a gray dashed line to the source positions determined here. Black triangles denote all possible station positions and the yellow lines indicate the San Andreas Fault surface trace. Please note, that the stations and number of stations used is different for each LFE and therefore the individual station configuration of each localization is not shown here. Furthermore, the depth axis includes the thickness of the absorbing layer of 1.5km. The direction to north is indicated by the black arrow in panel A.

distance to the stacked LFE family source locations of Shelly and Hardebeck (2010) support the expectation. However, in cases where the error range is near to model boundaries the determination of the source position can be erroneous. As an example, let us consider a case in which high cross-correlation values occur in shallow depths of 15 km. Assuming a real source depth of 25 km, the error range and thus high cross-correlation values must

also occur in depths of 35 km, which is exceeding the model dimensions. In such case, the depth of the source position might be erroneous due to the extension of the model. In fact, the more shallow average source positions in figure 3.23 might be caused by this issue.

3.4.8. Localization of individual LFE family members

Shelly and Hardebeck (2010) stacked up to 400 individual LFE's to increase the SNR and to obtain a family source location. However, due to the low amplitude character of tremor and hence low cross-correlation values at individual stations, the individual source locations are not expected to be identical and it is unclear how large the differences are. As the modified TRI method is capable of locating individual LFE's, the section shows the individual source location of LFE family members, evaluated by both the maximum median cross-correlation value and the median of the error range.

Within the located 34 LFE's in section 3.4.5 and 3.4.7 12 LFE's are classified as members of the same LFE family by Shelly and Hardebeck (2010). Figure 3.24 shows once more the locations, which are determined by the maximum median cross-correlation coefficient. The source location scatter includes some outliers. However, the majority of the error range covers the LFE family source location of Shelly and Hardebeck (2010). The median distance between both source locations is 1.95 km in X-direction, 2.18 km in Y-direction, and 2.85 km in depth.

Figure 3.25 shows the source locations determined by the median of the error range. The source locations are more compact and apart from three outliers, all determined source locations are in a depth between 20 km and 26 km. The median distance between both locations is 1.25 km in X-direction, 2.25 km in Y-direction and 5.1 km vertically. Compared to the source locations determined by the maximum median cross-correlation value, the average horizontal distance decreased while the vertical distance increased as it was observed in chapter 3.4.7.

Both figures show a variation of the individual LFE source locations compared to the determined LFE family location. However, a differentiation between artificial scattering due to uncertainties within the modified TRI locations and real perturbations within the source location is impossible to distinguish. A estimation of the maximum scattering based on the error range gives a cubic volume with 15 km edge length, which may be too large for a meaningful estimation.

3.5. Chapter conclusions

In this chapter, I present a modified TRI method as a new method for tremor localization. Instead of searching for a superposition maximum amplitude at individual time snapshots as within classical TRI methods, the modified TRI method searches for phase coherence over a short time period between the rebroadcasted wavefields. Thus, the advantage of the TRI method is the independence of amplitude and the inclusion of temporal information, which makes the modified TRI method more robust and suitable for low amplitude signals and sparse station configuration as is the case for tremor localization. Moreover, in theory the method does not rely on any *a-priori* information such as phase arrival times if the signal to noise ratio is high enough.

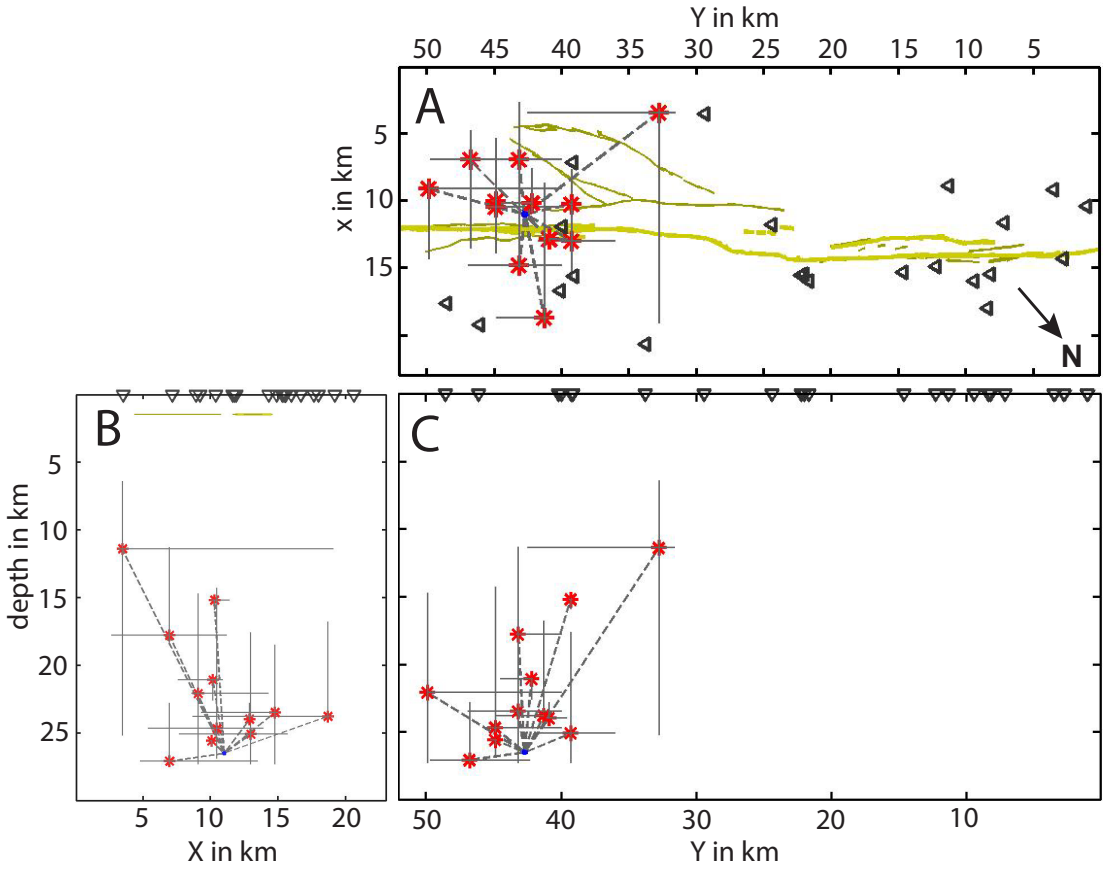

Figure 3.24.: Hypocentral location of 12 LFE family members determined by the maximum cross-correlation value. Panel A shows the plain view, panel B displays the vertical section in the X-axis and depth section, and panel C shows the vertical section in the Y-axis and depth section. The red stars indicate the determined source position, black lines show the estimated error range. The small red dots mark the stacked LFE family solution of Shelly and Hardebeck (2010) for reference and are connected with a gray dashed line to the source positions determined here. Black triangles denote all possible station positions and the yellow lines indicate the San Andreas Fault surface trace. Please note, that the stations and number of stations used is different for each LFE and therefore the individual station configuration of each localization is not shown here. Furthermore, the depth axis includes the thickness of the absorbing layer of 1.5km. The direction to north is indicated by the black arrow in panel A.

A synthetic test demonstrates the ability to reliably locate a double couple source at the defined source position with a horizontal uncertainty of 400 m and a vertical uncertainty of 800 m based on a 90% cutoff criterion. Moreover, a 2D synthetic test shows the source location differs only ± 100 m horizontally and ± 400 m vertically for signals with a SNR in the seismograms of down to 1.6. For lower SNR one has to include additional information

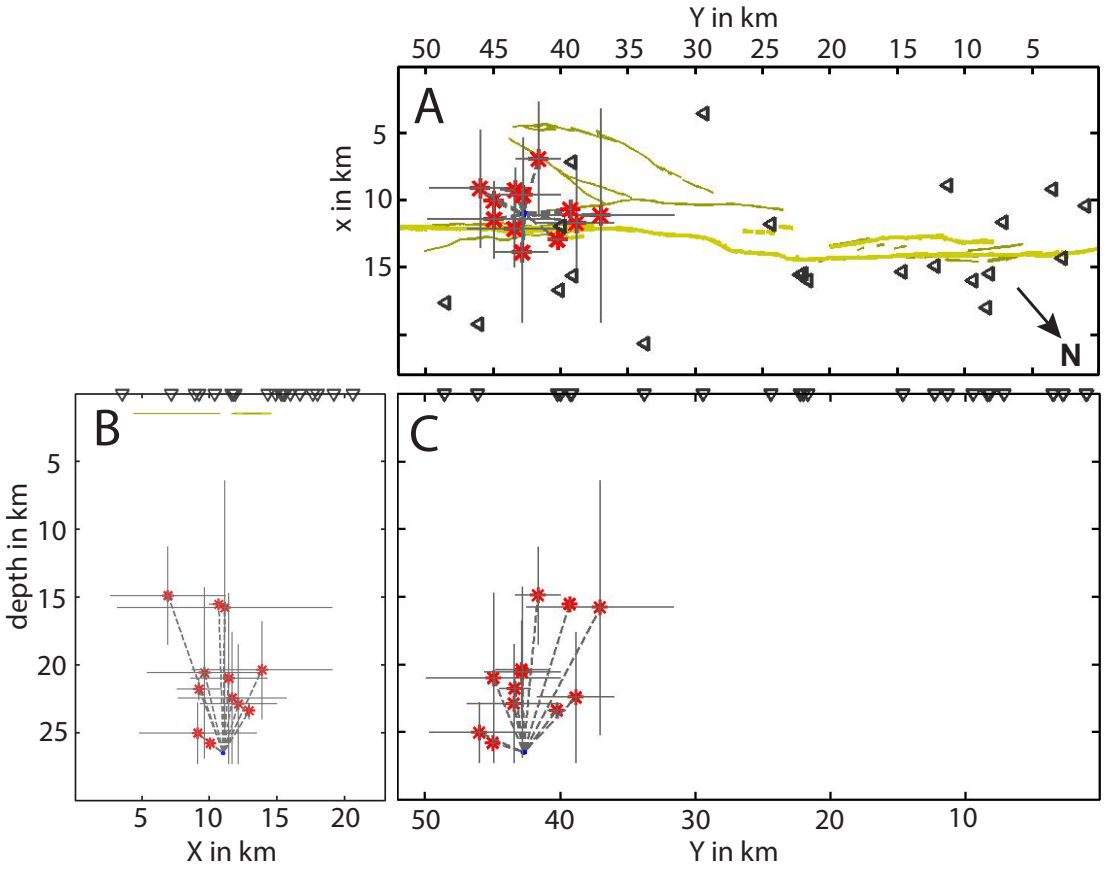

Figure 3.25.: Hypocentral location of 12 LFE family members determined by the median of the error range. Panel A shows the plain view, panel B displays the vertical section in the X-axis and depth section, and panel C shows the vertical section in the Y-axis and depth section. The red stars indicate the determined source position, black lines show the estimated error range. The small red dots mark the stacked LFE family solution of Shelly and Hardebeck (2010) for reference and are connected with a gray dashed line to the source positions determined here. Black triangles denote all possible station positions and the yellow lines indicate the San Andreas Fault surface trace. Please note, that the stations and number of stations used is different for each LFE and therefore the individual station configuration of each localization is not shown here. Furthermore, the depth axis includes the thickness of the absorbing layer of 1.5km. The direction to north is indicated by the black arrow in panel A.

such as the temporal and spatial stability of the maximum median cross-correlation value. Furthermore, perturbations of the velocity model in the order of 20% do not affect the location result. However, the tested velocity perturbations have zero mean, and could potentially average each other out.

The method successfully locates a recorded M 1.4 earthquake both in the frequency band of 0.5-2 Hz and in the frequency band of 1-5 Hz. However, the maximum median cross-correlation coefficient value decreases to 0.3 for the higher frequency band, in which tremor has its highest SNR. Furthermore, a test with only rebroadcasted S-phase pulses reveals a shift of more than one wavelength at the determined source position, evidencing inaccuracies of the velocity model and causing the low cross-correlation values. The location result can be improved significantly by tapering around the S-phase pulse with a 3 s long cosine taper in the seismogram, which reduces the uncertainty in the location result.

The larger uncertainties compared to the synthetic tests and associated with real data are due to multiple reasons. First, in my analysis I use the 3D P-velocity model of Thurber et al. (2006), which is interpolated to 0.1 km grid spacing from a more sparse distribution of velocity values on the order of 2 - 20 km between the values. Taking into account the low resolution of structures within the original velocity model and the frequency band of 2-8 Hz used, it is unlikely that complex travel paths of the coda can not be reconstructed. Moreover, I derive from the P-wave model a S-wave velocity model and a density model by assuming a Poisson ratio of 1.75 and use an experimental determined relationship between v_p and density ρ from Brocher (2005). Considering the branches of the SAF in the center of the model volume causing highly clastic rock with a wide range of v_p/v_s ratios and the different geological units on both sides of the fault, both conversions are associated with a high degree of uncertainty. Furthermore, the calculation of wave propagation is done under the assumption of an isotropic and elastic medium, which represents an idealized case. And finally, noise within the seismograms influence the location result as well.

Therefore, the localization of low amplitude tremor is accompanied with large uncertainties. To obtain feasible results, I apply the tapering techniques to LFE events. Thus, the modified TRI method locates an individual LFE within a tremor episode with an uncertainty of approximate 8 km horizontally and 8.5 km in depth. By comparison, the method of Wech and Creager (2008) provides an estimation of the tremor episode location in figure 2.11 with an horizontal uncertainty range of 30 km. Other methods which located individual LFE's have location errors on the order of 10 km or more (Payero et al., 2008). In addition, the determined source positions are in good agreement with the LFE family source position determined by Shelly and Hardebeck (2010), who stacked up to 400 individual LFE's to improve the SNR and obtain precise LFE family locations. The difference between both location is 0.4 km horizontally and 2 km in depth. In total I locate 34 individual LFE's with an average uncertainty for the individual determined LFE source locations of 5 km in X-direction, 2.6 km in Y-direction, and 4.8 km in depth.

Furthermore, I determine the influence of individual parameters to the location result. I find only a very weak impact of the maximum in azimuthal coverage and the distance from the determined source to the nearest station on the horizontal uncertainty of the determined location. The number of stations and the median SNR in the seismograms do not show a explicit trend indicating any significant influence on the location result.

Moreover, the value of the maximum median cross-correlation coefficient is not a proxy on how well a source location is determined. However, I find a clear relationship between the value of the maximum median cross-correlation value and the number of stations used for rebroadcasting the recorded seismograms. The maximum median cross-correlation value decreases with an increased number of stations, which is a result of inaccuracies of the velocity model due to the decrease of freedom when using an increased number of stations.

Due to the uncertainties associated with the velocity model, anisotropy, and noise in the seismograms, the range between local maxima of cross-correlation values is in the order of 0.05 and hence not a definitive indicator of a particular gridpoint marking the source location.. Thus, determining the source position by searching for the highest median cross-correlation coefficient and relying on only one value may over-interpret the data. Therefore, I introduce a different manner to determine the source position in the modified TRI method, which is based on the 90% cutoff criterion of the error estimation and hence on multiple maxima: the source position is defined by the median of the error extent instead of the maximum median cross-correlation value. The technique improves the robustness of the location result by making it more conservative, and provides a more compact source location result. Furthermore, the determined source positions are in better agreement with the stacked LFE family source locations of Shelly and Hardebeck (2010) with an average horizontal distance of 2 km. However, the technique introduces a systematic bias at source positions near model boundaries, which is likely the reason why the depths are in general more shallow compared to the source positions determined by the maximum median cross-correlation value and by Shelly and Hardebeck (2010). A detailed analysis of the effect is subject of future work.

Finally, I show the determined source position of 12 individual LFE's, which are classified as one LFE family and therefore located at the same position by Shelly and Hardebeck (2010). The source locations of the modified TRI method show increased scatter, however, it is impossible to differentiate between perturbations of the source position and inadequateness of the method.

In summary, the modified TRI method locates individual low amplitude LFE's with higher precision compared to other methods which also locate individual LFE's and in theory without the knowledge of *a priori* information. However, the inaccuracies of the velocity model demand the the application of a cosine tapering window. Moreover, the rebroadcasting of individual recorded seismograms is computational demanding and hence the localization is computational time consuming. The median error extent source location is a promising approach, in fact, preliminary tests suggest a successful application to untapered LFE's. However, the right choice for the cutoff value and analysis of the potential bias are subject of forthcoming work.

4. Thesis summary and perspective

Tremor is characterized by long-duration, low-amplitude, and slowly emergent phase arrivals. While classic earthquake detection and location algorithms exploit the short-term amplitude change at phase arrivals, the lack of distinct phase arrivals makes tremor detection and localization a difficult task. I introduce a new semi-automated method for tremor detection in chapter 2 and present a new method for tremor localization in chapter 3.

The tremor detection is based on a neural network approach and the method identifies and distinguishes tremor, earthquakes, and noise based on frequency content and horizontal to vertical component products. To increase computational efficiency, the data volume is reduced first using a waveform envelope cross-correlation. The method does not rely on *a priori* information such as event templates and is capable of identifying tremor bursts of variable duration, assuming some variation in tremor amplitude within the length of the noise window (420 sec). Moreover, the sensitivity of the method can be adjusted by a set of normalization factors, F_{mean} and F_{std}.

The fundamental advance of the method is that it does not rely on master templates and is not based on any assumptions about a minimum signal length. Removing such restrictions permits the detection of a wider range of event types than present methods, thereby increasing the potential for discovering tremor at different depths within the fault zone.

The performance of the method is tested with a three week long test data set, indicating a tremor detection accuracy of nearly 80% for the SOM and post processing steps by comparison to manual picks. I expect a similar detection accuracy for continuously recorded dataset from May 2010 to July 2011, in which the method detects 2606 tremor detections occurring in windows totaling over 55 h. A comparison of the SOM earthquake detections with the Advanced National Seismic System (ANSS) catalog shows a detection accuracy of approximately 90%.

Furthermore, the influence of SNR and number of stations used is determined in the test data set period. The event detection is based on a minimum of 3 stations, however, I find an optimum detection performance with approximately 10 stations for the particular

network configuration. Analysis of the influence of individual stations shows that KIT11, PKD, FROB, and VARB are the most valuable stations during the test dataset period. I find a detection completeness of 96% for tremor events with a SNR above 3, decreasing to approximately 80% for tremor signals with a SNR value of 2 or higher.

The method is tested against the tremor detection method of Wech and Creager (2008), indicating both a higher sensitivity and a better accuracy. However, the method of Wech and Creager (2008) provides a automated detection whereas the SOM needs a calibration of the normalizing factors for each dataset.

The SOM method is in general very flexible and could be adjusted by supplementing further features and/or by changing the detection sensitivity. Additional features such as polarity might be useful when tremor is polarized as observed in Cascadia (Wech and Creager, 2007). Moreover, taking into account the amplitude of the frequency band of surface waves may help to identify and distinguish between triggered and ambient tremor. Due to the calibration of the method, a parameter analysis is mandatory to determine an optimum normalizing values for each feature. Furthermore, a sensitivity test of individual parameters is necessary in case of a potential additional features, and a multi dimensional parameter analysis is not trivial. Saltelli et al. (2008) describes numerous methods and strategies, which has been developed to fulfill the task. However, a implementation of a clever parameter sensitivity analysis is a remaining task.

The tremor localization is based on time-reversal imaging techniques. I present a modified TRI method which searches for phase coherence over a short time period instead of the maximum amplitude of a superpositioned wavefield. The advantage of the modified TRI method is the independence of amplitude and the inclusion of temporal information, which makes the modified TRI method more robust. Moreover, in theory the modified TRI method does not rely on any *a priori* information such as phase arrival times given a high enough signal to noise ratio.

I show using synthetic tests that the modified TRI method is capable of locating a double couple source at the modeled source position with an uncertainty of 400 m horizontally and 800 m vertically. Moreover, the test indicates that the modified TRI method can locate signals with a SNR down to 1.6.

The modified TRI method successfully locates a recorded M 1.4 earthquake. However, rebroadcasted S-phase pulses reveal a shift of more than one wavelength at the determined source position, evidencing inaccuracies of the velocity model and causing low median cross-correlation values around 0.3. Thus, the location result has large uncertainties of for example 13 km in the X-direction, which can be decreased significantly by tapering around the S-phase pulse with a 3 s long cosine taper in the seismogram reducing the uncertainty to 3.7 km in X-direction.

The low amplitude character of tremor adds to the problem of the inaccurate velocity model. In order to locate tremor, I apply the tapering technique to a 34 individual LFE events within tremor episodes. The location results are associated with an average uncertainty of 5 km in X-direction, 2.6 km in Y-direction, and 4.8 km in depth. Furthermore, I use Shelly and Hardebeck (2010) LFE family locations as a reference to show that

locations are reasonable with a median difference between both locations of 2.7 km in X-direction, 1.9 km in Y-direction, and 2.6 km in depth.

Furthermore, I determine the influence of individual parameters to the location result. The maximum azimuthal coverage and the determined source and the nearest station only weakly influences the horizontal uncertainty. The number of stations used and the median SNR in the seismograms do not show a systematic impact on the horizontal uncertainty. Moreover, the value of the maximum median cross-correlation coefficient can not be used as a proxy on how well a source location is determined, however, I find a decreasing relationship between the number of stations used and the value of the maximum median cross-correlation value.

The low maximum median cross-correlation coefficient and the small range of coefficient values result from a combination of factors, including uncertainties of the velocity model, anisotropy, and noise in the seismograms. Thus, determining the source position by searching for the highest median cross-correlation coefficient and relying on only one value may over-interpret the data. Therefore, I introduce a additional source determination manner based on the 90% cutoff criterion of the error estimation. The source position is defined by the median of the error extent, which is based on the position of multiple maxima. The technique improves the robustness of the location result and the locations agree better with the stacked LFE family locations of Shelly and Hardebeck (2010) with an average horizontal distance of 2 km. However, source positions near the model boundaries might be subject to a bias.

Some remaining issues retain open and are interesting subject of forthcoming work, such as the impact of a potential bias and the right choice of the cutoff value of the median error extent source determination. In fact, preliminary tests suggest a successful application of the median extent source determination to untapered LFE's. Furthermore, a weighting scheme for different stations and a S-wave velocity model derived by a flexible v_p/v_s ratio may improve the location results.

Bibliography

Advanced National Seismic System (2012). Available at: http://quake.geo.berkeley.edu/anss [17 Jan 2012].

Allen, R. (1982). Automatic phase pickers: Their present use and future prospects. *Bull. Seismol. Soc. Am.*, 72(6B):S225–S242.

Anderson, B. E., Griffa, M., Larmat, C., Ulrich, T. J., and Johnson, P. A. (2008). Time reversal. *Acoustics Today*, 4(1):5–16.

Anderson, B. E., Griffa, M., Ulrich, T. J., and Johnson, P. A. (2011). Time reversal reconstruction of finite sized sources in elastic media. *The Journal of the Acoustical Society of America*, 130(4):EL219–EL225.

Aviles, C. A., Scholz, C. H., and Boatwright, J. (1987). Fractal analysis applied to characteristic segments of the san andreas fault. *Journal of Geophysical Research: Solid Earth*, 92(B1):331–344.

Bakun, W. H. and Lindh, A. G. (1985). The parkfield, california, earthquake prediction experiment. *Science*, 229(4714):619–624.

Beroza, G. and Ide, S. (2011). Slow earthquakes and nonvolcanic tremor. *Annual Review of Earth and Planetary Sciences*, 39:271–296.

Bohlen, T. (2002). Parallel 3-d viscoelastic finite difference seismic modelling. *Computers & Geosciences*, 28(8):887 – 899.

Brocher, T. M. (2005). Empirical relations between elastic wavespeeds and density in the earth's crust. *Bulletin of the Seismological Society of America*, 95(6):2081–2092.

Brown, J., Beroza, G., Ide, S., Ohta, K., Shelly, D., Schwartz, S., Rabbel, W., Thorwart, M., and Kao, H. (2009). Deep low-frequency earthquakes in tremor localize to the plate interface in multiple subduction zones. *Geophysical Research Letters*, 36(19):L19306.

Brown, J., Beroza, G., and Shelly, D. (2008). An autocorrelation method to detect low frequency earthquakes within tremor. *Geophys. Res. Lett.*, 35:L16305.

Brudzinski, M. and Allen, R. (2007). Segmentation in episodic tremor and slip all along cascadia. *Geology*, 35(10):907–910.

Brum, J., Catheline, S., Benech, N., and Negreira, C. (2008). Shear elasticity estimation from surface wave: The time reversal approach. *The Journal of the Acoustical Society of America*, 124(6):3377–3380.

Cochran, E. S., Li, Y.-G., and Vidale, J. E. (2006). Anisotropy in the shallow crust observed around the san andreas fault before and after the 2004 m 6.0 parkfield earthquake. *Bulletin of the Seismological Society of America*, 96(4B):S364–S375.

Courant, R., Friedrichs, K., and Lewy, H. (1967). On the partial difference equations of mathematical physics. *IBM Journal of Research and Development*, 11(2):215–234.

Davies, D. and Bouldin, D. (1979). A cluster separation measure. *IEEE T. Pattern. Anal.*, PAMI-1 , Issue:2(2):224–227.

DeMets, C. and Dixon, T. H. (1999). New kinematic models for pacific-north america motion from 3 ma to present, i: Evidence for steady motion and biases in the nuvel-1a model. *Geophysical Research Letters*, 26(13):1921–1924.

Dougherty, M. E. and Stephen, R. A. (1988). Seismic energy partitioning and scattering in laterally heterogeneous ocean crust. *pure and applied geophysics*, 128(1-2):195–229.

Fink, M., Montaldo, G., and Tanter, M. (2003). Time-reversal acoustics in biomedical engineering. *Annual review of biomedical engineering*, 5(1):465–497.

Fletcher, J. B. and Baker, L. M. (2010). Analysis of nonvolcanic tremor on the san andreas fault near parkfield, ca using u. s. geological survey parkfield seismic array. *Journal of Geophysical Research: Solid Earth*, 115(B10):n/a–n/a.

Ghosh, A., Vidale, J., Peng, Z., Creager, K., and Houston, H. (2009). Complex nonvolcanic tremor near parkfield, california, triggered by the great 2004 sumatra earthquake. *J. Geophys. Res.*, 114:B00A15.

Gomberg, J., Rubinstein, J. L., Peng, Z., Creager, K. C., Vidale, J. E., and Bodin, P. (2008). Widespread triggering of nonvolcanic tremor in california. *Science*, 319(5860):173.

Harris, R. A. and Archuleta, R. J. (1988). Slip budget and potential for a m7 earthquake in central california. *Geophysical Research Letters*, 15(11):1215–1218.

Hickman, S., Zoback, M., and Ellsworth, W. (2004). Introduction to special section: Preparing for the san andreas fault observatory at depth. *Geophysical Research Letters*, 31(12):L12S01.

Horstmann, T., Harrington, R. M., and Cochran, E. S. (2013). Semi-automated tremor detection using a combined cross-correlation and neural network approach. *Journal of Geophysical Research: Solid Earth to appear*.

Ide, S., Beroza, G. C., Shelly, D. R., and Uchide, T. (2007a). A scaling law for slow earthquakes. *Nature*, 447(7140):76–79.

Ide, S., Shelly, D. R., and Beroza, G. C. (2007b). Mechanism of deep low frequency earthquakes: Further evidence that deep non-volcanic tremor is generated by shear slip on the plate interface. *Geophysical Research Letters*, 34(3):L03308.

Jepsen, D. and Kennett, B. (1990). Three-component analysis of regional seismograms. *Bull. Seismol. Soc. Am.*, 80(6B):2032.

Kanamori, H. (2003). 72 earthquake prediction: An overview. In William H.K. Lee, Hiroo Kanamori, P. C. J. and Kisslinger, C., editors, *International Handbook of Earthquake and Engineering Seismology*, volume 81, Part B of *International Geophysics*, pages 1205 – 1216. Academic Press.

Kao, H. and Shan, S. (2004). The source-scanning algorithm: Mapping the distribution of seismic sources in time and space. *Geophys. J. Int.*, 157(2):589–594.

Katsumata, A. and Kamaya, N. (2003). Low-frequency continuous tremor around the moho discontinuity away from volcanoes in the southwest japan. *Geophys. Res. Lett*, 30(1):1020.

Kissling, E., Kradolfer, U., and Maurer, H. (1995). Velest user's guide-short introduction. *Institute of Geophysics and Swiss Seismological Service*, 25.

Köhler, A., Ohrnberger, M., and Scherbaum, F. (2009). Unsupervised feature selection and general pattern discovery using self-organizing maps for gaining insights into the nature of seismic wavefields. *Computers & Geosciences*, 35(9):1757 – 1767.

Köhler, A., Ohrnberger, M., and Scherbaum, F. (2010). Unsupervised pattern recognition in continuous seismic wavefield records using self-organizing maps. *Geophys. J. Int.*, 182, Issue 3:1619–1630.

Kohonen, T. (2001). *Self-Organising Maps*, volume 30. Springer.

Komatitsch, D. and Martin, R. (2007). An unsplit convolutional perfectly matched layer improved at grazing incidence for the seismic wave equation. *GEOPHYSICS*, 72(5):SM155–SM167.

Käufl, J. (2012). Refined locations of the permit experiments, cholame, california. Bachelor's thesis, Karlsruhe Institute of Technology (KIT).

La Rocca, M., Creager, K. C., Galluzzo, D., Malone, S., Vidale, J. E., Sweet, J. R., and Wech, A. G. (2009). Cascadia tremor located near plate interface constrained by s minus p wave times. *Science*, 323(5914):620–623.

La Rocca, M., Galluzzo, D., Malone, S., McCausland, W., Saccorotti, G., and Del Pezzo, E. (2008). Testing small-aperture array analysis on well-located earthquakes, and application to the location of deep tremor. *Bulletin of the Seismological Society of America*, 98(2):620–635.

La Rocca, M., McCausland, W., Galluzzo, D., Malone, S., Saccorotti, G., and Del Pezzo, E. (2005). Array measurements of deep tremor signals in the cascadia subduction zone. *Geophysical Research Letters*, 32(21):n/a–n/a.

Lahr, J. (1999). Hypoellipse: A computer program for determining local earthquake hypocentral parameters, magnitude and first motion pattern. *US Geological Survey Open-File Report*, pages 99–23.

Larmat, C., Montagner, J.-P., Fink, M., Capdeville, Y., Tourin, A., and Clévédé, E. (2006). Time-reversal imaging of seismic sources and application to the great sumatra earthquake. *Geophysical Research Letters*, 33(19):n/a–n/a.

Larmat, C. S., Guyer, R. A., and Johnson, P. A. (2009). Tremor source location using time reversal: Selecting the appropriate imaging field. *Geophysical Research Letters*, 36(22):n/a–n/a.

Lewis, M. A. and Ben-Zion, Y. (2010). Diversity of fault zone damage and trapping structures in the parkfield section of the san andreas fault from comprehensive analysis of near fault seismograms. *Geophysical Journal International*, 183(3):1579–1595.

Li, Y.-G., Leary, P., Aki, K., and Malin, P. (1990). Seismic trapped modes in the oroville and san andreas fault zones. *Science*, 249(4970):763–766.

Liu, Y., Zhang, H., Thurber, C., and Roecker, S. (2008). Shear wave anisotropy in the crust around the san andreas fault near parkfield: spatial and temporal analysis. *Geophysical Journal International*, 172(3):957–970.

Lokmer, I., O'Brien, G. S., Stich, D., and Bean, C. J. (2009). Time reversal imaging of synthetic volcanic tremor sources. *Geophysical Research Letters*, 36(12):n/a–n/a.

Loveless, J. P. and Meade, B. J. (2011). Stress modulation on the san andreas fault by interseismic fault system interactions. *Geology*, 39(11):1035–1038.

Martin, R. (1994). Spectral subtraction based on minimum statistics. *Proc. Eur. Signal Processing Conf.*, pages 1182–1185.

Martin, R. (2001). Noise power spectral density estimation based on optimal smoothing and minimum statistics. *IEEE T. Speech. Audi. P.*, 9(5):504–512.

McBride, J. H. and Brown, L. D. (1986). Reanalysis of the cocorp deep seismic reflection profile across the san andreas fault, parkfield, california. *Bulletin of the Seismological Society of America*, 76(6):1668–1686.

McCausland, W., Malone, S., and Johnson, D. (2005). Temporal and spatial occurrence of deep non-volcanic tremor: From washington to northern california. *Geophys. Res. Lett.*, 32(24):L24311.

Miller, M. M., Melbourne, T., Johnson, D. J., and Sumner, W. Q. (2002). Periodic slow earthquakes from the cascadia subduction zone. *Science*, 295(5564):2423.

Miyazawa, M. and Brodsky, E. E. (2008). Deep low-frequency tremor that correlates with passing surface waves. *Journal of Geophysical Research: Solid Earth*, 113(B1):B01307.

Nadeau, R. and Dolenc, D. (2005). Nonvolcanic tremors deep beneath the san andreas fault. *Science*, 307(5708):389.

Nadeau, R. M. and Guilhem, A. (2009). Nonvolcanic tremor evolution and the san simeon and parkfield, california, earthquakes. *Science*, 325(5937):191–193.

Obara, K. (2002). Nonvolcanic deep tremor associated with subduction in southwest japan. *Science*, 296(5573):1679.

Obara, K., Hirose, H., Yamamizu, F., and Kasahara, K. (2004). Episodic slow slip events accompanied by non-volcanic tremors in southwest japan subduction zone. *Geophys. Res. Lett.*, 31(23):L23602.

Payero, J., Kostoglodov, V., Shapiro, N., Mikumo, T., Iglesias, A., Pérez-Campos, X., and Clayton, R. (2008). Nonvolcanic tremor observed in the mexican subduction zone. *Geophys. Res. Lett.*, 35(7):L07305.

Peng, Z. and Chao, K. (2008). Non-volcanic tremor beneath the central range in taiwan triggered by the 2001 mw 7.8 kunlun earthquake. *Geophys. J. Int.*, 175(2):825–829.

Peng, Z., Vidale, J., Creager, K., Rubinstein, J., Gomberg, J., and Bodin, P. (2008). Strong tremor near parkfield, ca, excited by the 2002 denali fault earthquake. *Geophys. Res. Lett.*, 35(23):L23305.

Peng, Z., Vidale, J. E., Wech, A. G., Nadeau, R. M., and Creager, K. C. (2009). Remote triggering of tremor along the san andreas fault in central california. *J. Geophys. Res.*, 114:B00A06.

Peterson, C. and Christensen, D. (2009). Possible relationship between nonvolcanic tremor and the 1998–2001 slow slip event, south central alaska. *J. Geophys. Res.*, 114(B6):B06302.

Pyle, D. (1999). *Data preparation for data mining*, volume 1. Morgan Kaufmann.

Rogers, G. and Dragert, H. (2003). Episodic tremor and slip on the cascadia subduction zone: The chatter of silent slip. *Science*, 300(5627):1942.

Rolandone, F., Bürgmann, R., Agnew, D. C., Johanson, I. A., Templeton, D. C., d'Alessio, M. A., Titus, S. J., DeMets, C., and Tikoff, B. (2008). Aseismic slip and fault-normal strain along the central creeping section of the san andreas fault. *Geophysical Research Letters*, 35(14):L14305.

Rubinstein, J., Shelly, D., and Ellsworth, W. (2010). Non-volcanic tremor: A window into the roots of fault zones. In Cloetingh, S. and Negendank, J., editors, *New Frontiers in Integrated Solid Earth Sciences*, International Year of Planet Earth, pages 287–314. Springer Netherlands.

Ryberg, T., Haberland, C., Fuis, G., Ellsworth, W., and Shelly, D. (2010). Locating non-volcanic tremor along the san andreas fault using a multiple array source imaging technique. *Geophys. J. Int.*, 183(3):1485–1500.

Saltelli, A., Ratto, M., Andres, T., Campolongo, F., Cariboni, J., Gatelli, D., Saisana, M., and Tarantola, S. (2008). *Global sensitivity analysis: the primer*. Wiley Online Library.

Santos, S. D. and Prevorovsky, Z. (2011). Imaging of human tooth using ultrasound based chirp-coded nonlinear time reversal acoustics. *Ultrasonics*, 51(6):667 – 674.

Schulz, S. S. and Wallace, R. E. (1997). The san andreas fault. Available at: http://pubs.usgs.gov/gip/earthq3/where.html [28 Aug 2013].

Schwartz, S. and Rokosky, J. (2007). Slow slip events and seismic tremor at circum-pacific subduction zones. *REVIEWS OF GEOPHYSICS-RICHMOND VIRGINIA THEN WASHINGTON-*, 45(3).

Shelly, D. (2010). Migrating tremors illuminate complex deformation beneath the seismogenic san andreas fault. *Nature*, 463(7281):648–652.

Shelly, D., Beroza, G., and Ide, S. (2007). Non-volcanic tremor and low-frequency earthquake swarms. *Nature*, 446(7133):305–307.

Shelly, D., Beroza, G., Ide, S., and Nakamula, S. (2006). Low-frequency earthquakes in shikoku, japan, and their relationship to episodic tremor and slip. *Nature*, 442(7099):188–191.

Shelly, D. and Hardebeck, J. (2010). Precise tremor source locations and amplitude variations along the lower-crustal central san andreas fault. *Geophys. Res. Lett.*, 37(14):L14301.

Sieh, K., Stuiver, M., and Brillinger, D. (1989). A more precise chronology of earthquakes produced by the san andreas fault in southern california. *Journal of Geophysical Research: Solid Earth*, 94(B1):603–623.

Smith, E. F. and Gomberg, J. (2009). A search in strainmeter data for slow slip associated with triggered and ambient tremor near parkfield, california. *Journal of Geophysical Research: Solid Earth*, 114(B12):B00A14.

Solum, J. G., Hickman, S. H., Lockner, D. A., Moore, D. E., van der Pluijm, B. A., Schleicher, A. M., and Evans, J. P. (2006). Mineralogical characterization of protolith and fault rocks from the safod main hole. *Geophysical Research Letters*, 33(21):L21314.

Steinbrugge, K. V., Zacher, E. G., Tocher, D., Whitten, C. A., and Claire, C. N. (1960). Creep on the san andreas fault. *Bulletin of the Seismological Society of America*, 50(3):389–415.

Stockwell, R., Mansinha, L., and Lowe, R. (1996). Localization of the complex spectrum: the s transform. *IEEE T. Signal. Proces.*, 44(4):998 –1001.

Sutin, A., Libbey, B., Fillinger, L., and Sarvazyan, A. (2009). Wideband nonlinear time reversal seismo-acoustic method for landmine detection. *The Journal of the Acoustical Society of America*, 125(4):1906–1910.

Thurber, C., Zhang, H., Waldhauser, F., Hardebeck, J., Michael, A., and Eberhart-Phillips, D. (2006). Three-dimensional compressional wavespeed model, earthquake relocations, and focal mechanisms for the parkfield, california, region. *Bulletin of the Seismological Society of America*, 96(4B):S38–S49.

Titus, S. J., DeMets, C., and Tikoff, B. (2005). New slip rate estimates for the creeping segment of the san andreas fault, california. *Geology*, 33(3):205–208.

Tong, X., Sandwell, D. T., and Smith-Konter, B. (2013). High-resolution interseismic velocity data along the san andreas fault from gps and insar. *Journal of Geophysical Research: Solid Earth*, 118(1):369–389.

Ulrich, T. J., Johnson, P. A., and Guyer, R. A. (2007). Interaction dynamics of elastic waves with a complex nonlinear scatterer through the use of a time reversal mirror. *Phys. Rev. Lett.*, 98:104301.

Ulrich, T. J., Johnson, P. A., and Sutin, A. (2006). Imaging nonlinear scatterers applying the time reversal mirror. *The Journal of the Acoustical Society of America*, 119(3):1514–1518.

Unsworth, M. J., Malin, P. E., Egbert, G. D., and Booker, J. R. (1997). Internal structure of the san andreas fault at parkfield, california. *Geology*, 25(4):359–362.

van der Elst, N. and Brodsky, E. (2010). Connecting near-field and far-field earthquake triggering to dynamic strain. *J. Geophys. Res.*, 115:B07311.

Vesanto, J. (2000). Neural network tool for data mining: Som toolbox. In *Proceedings of symposium on tool environments and development methods for intelligent systems (TOOLMET2000)*, pages 184–196.

Vesanto, J. and Alhoniemi, E. (2000). Clustering of the self-organizing map. *IEEE T. Neural. Networ.*, 11(3):586–600.

Wallace, R. E. (1990). *The San Andreas fault system, California*. US Government Printing Office Washington, DC.

Walter, J., Schwartz, S., Protti, J., and Gonzalez, V. (2011). Persistent tremor within the northern costa rica seismogenic zone. *Geophys. Res. Lett.*, 38(1):L01307.

Wang, T., Cochran, E., Agnew, D., and Oglesby, D. (2013). Infrequent triggering of tremor along the san jacinto fault near anza, california. *BSSA*. in press.

Wech, A. and Creager, K. (2007). Cascadia tremor polarization evidence for plate interface slip. *Geophys. Res. Lett.*, 34(22):L22306.

Wech, A. and Creager, K. (2008). Automated detection and location of cascadia tremor. *Geophys. Res. Lett.*, 35(20):L20302.

Weldon, R., Scharer, K., Fumal, T., and Biasi, G. (2004). Wrightwood and the earthquake cycle: What a long recurrence record tells us about how faults work. *GSA today*, 14(9):4–10.

White, J. (1964). Motion product seismograms. *Geophysics*, 29:288.

Zhang, J., Gerstoft, P., Shearer, P. M., Yao, H., Vidale, J. E., Houston, H., and Ghosh, A. (2011). Cascadia tremor spectra: Low corner frequencies and earthquake-like high-frequency falloff. *Geochemistry, Geophysics, Geosystems*, 12(10):Q10007.

Appendix

A. Localization of a M1.4 earthquake: additional figures

Section 3.4.3 describes the localization of a M1.4 earthquake in two different frequency bands. Additionally to the material presented in section 3.4.3 I show here in figure A.1 the waveforms used for rebroadcasting in the frequency band of 1-5 Hz and the curl field functions at the determined source position in figure A.2.

B. Table of location result for multiple LFE's

In section 3.4.7 I locate 34 LFE's based on the median error extent. The determined source location of LFE's in the local grid coordinate system X,Y, and Z, and the corresponding latitude and longitude values are given in table B.1.

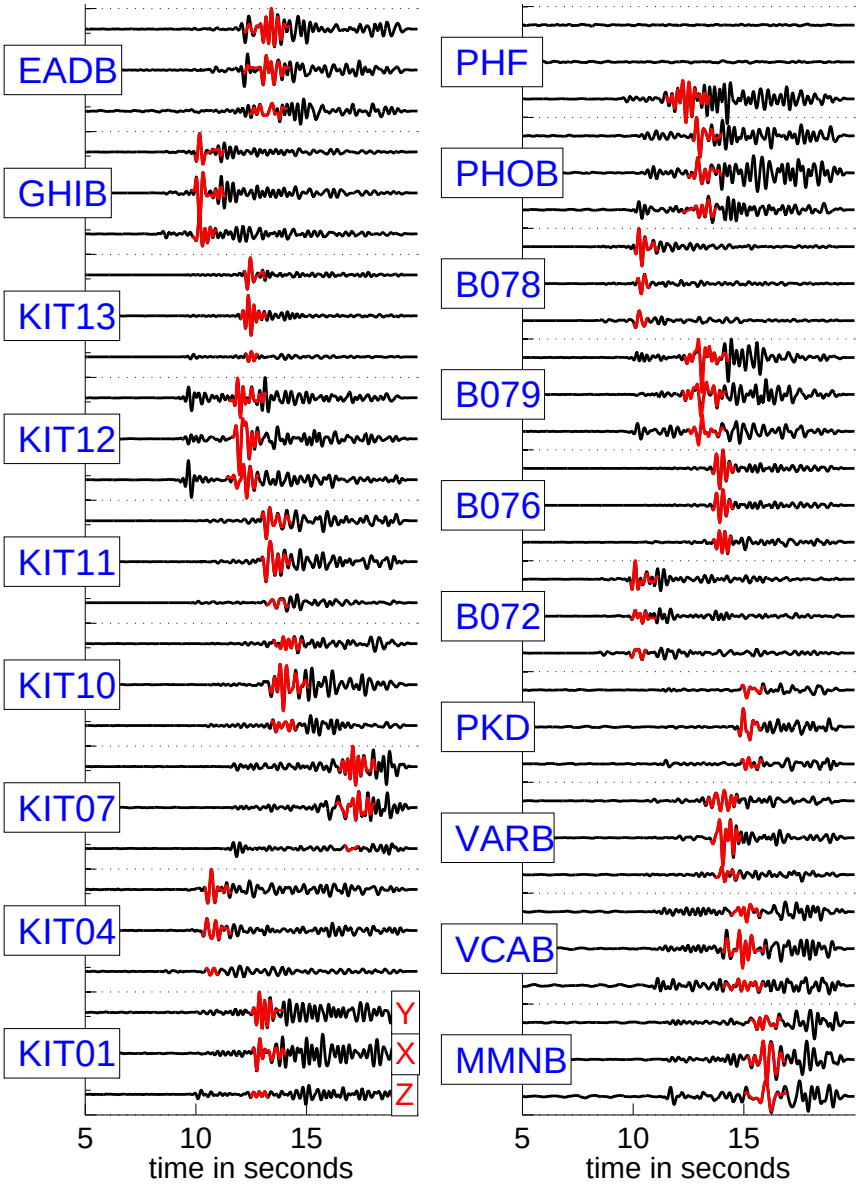

Figure A.1.: Waveforms of a M1.4 earthquake recorded at 23th of May, 2010, filtered between 1 and 5 Hz. Complete waveforms shown in black, the tapered S-phase signals used in the waveform rebroadcasting shown in red.

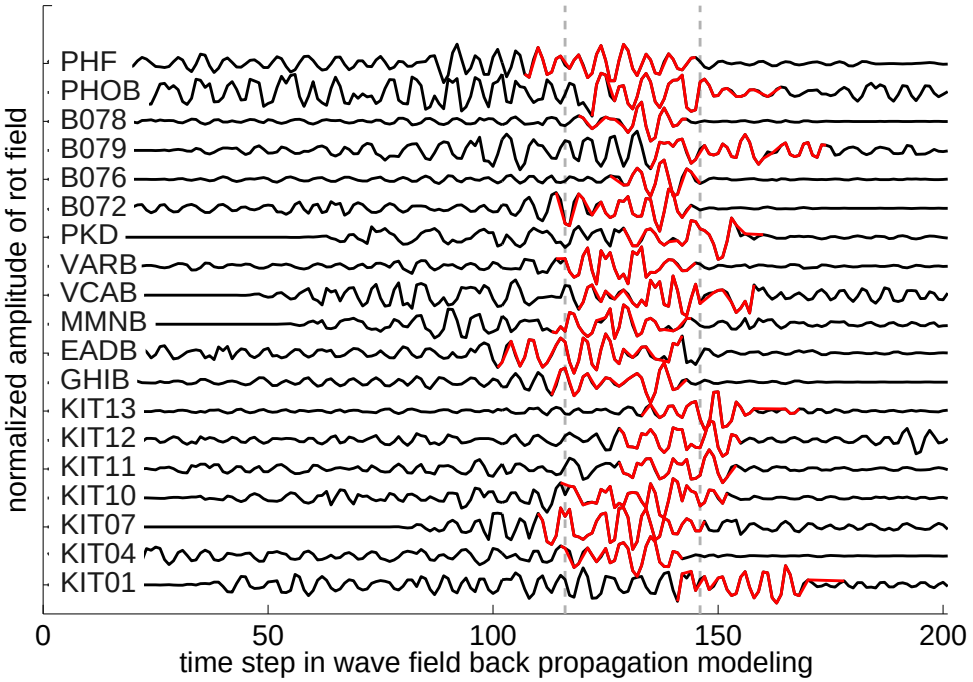

Figure A.2.: Functions of the curl field at gridpoint X=14.8km, Y=23.6km and 7.6km depth for the seismograms shown in figure A.1. The gray dashed line denotes the position of the time window with the maximum median cross-correlation coefficient. Red indicates the position of the separate rebroadcasted tapered S-phase.

	start of time window	X (km)	Y (km)	Z (km)	Latitude (deg. N)	Longitude (deg. W)	hor. diff. (km)	vert. diff. (km)
1	2010-07-01 17:42:50	13.75±5.15	38.10±2.4	23.00±4	35.713	-120.245	2.13	-3.50
2	2010-07-01 17:42:50	13.75±5.15	38.10±2.4	23.00±4	35.713	-120.245	2.13	-3.50
3	2010-07-02 04:42:45	12.95±7.45	26.15±1.55	24.10±2.9	35.789	-120.339	0.15	-2.40
4	2010-07-02 13:59:20	6.20±0.6	36.50±0.7	24.75±1.55	35.679	-120.320	5.83	1.00
5	2010-07-03 08:21:15	15.25±3.55	39.00±1.3	20.15±1.75	35.715	-120.226	6.22	-4.10
6	2010-07-04 11:08:35	11.30±4.5	33.45±1.45	24.15±1.95	35.730	-120.300	0.42	-0.60
7	2010-08-04 10:32:05	9.85±2.55	42.25±2.35	21.95±4.75	35.662	-120.248	2.21	-3.55
8	2010-08-04 10:40:00	10.05±0.05	45.00±0.2	25.80±0.2	35.644	-120.227	2.48	-0.70
9	2010-08-06 00:35:25	12.55±1.85	44.10±1.3	20.05±2.35	35.665	-120.212	4.34	-6.45
10	2010-08-06 00:35:45	9.15±5.95	47.05±2.85	23.05±4.25	35.625	-120.220	2.92	-2.95
11	2010-09-02 10:31:40	9.15±4.35	46.00±3.7	25.05±2.25	35.632	-120.227	3.78	-1.45
12	2010-09-02 17:32:40	8.60±0.8	37.20±0.3	24.10±2	35.689	-120.295	1.88	1.60
13	2010-09-02 19:27:40	12.00±4	33.75±1.05	20.85±3.75	35.732	-120.292	0.37	-3.90
14	2010-09-10 02:29:05	12.95±0.05	40.25±0.65	23.40±0.6	35.693	-120.237	3.13	-3.10
15	2010-10-09 08:52:50	13.90±5.2	42.85±1.95	20.40±3.6	35.681	-120.210	2.87	-6.10
16	2010-10-12 12:51:45	13.85±0.35	28.40±0.1	22.60±0.2	35.779	-120.315	2.74	-1.65
17	2010-10-12 21:07:45	11.15±7.95	37.05±5.45	15.80±9.4	35.705	-120.275	5.68	-10.70
18	2010-10-12 21:07:50	10.70±0.7	39.30±0.1	15.55±0.35	35.687	-120.262	3.44	-10.95
19	2010-10-22 14:31:30	19.15±1.65	23.30±0.4	22.75±1.65	35.845	-120.307	6.81	-3.75
20	2010-10-26 12:17:15	8.85±5.25	36.65±1.25	16.50±2.9	35.694	-120.297	1.70	-6.00
21	2010-11-07 02:45:45	8.85±2.55	39.65±3.85	17.20±5.6	35.673	-120.275	9.10	-9.30
22	2010-11-16 08:54:10	12.15±2.85	43.45±3.45	22.90±4.4	35.667	-120.220	1.33	-3.60
23	2010-11-17 10:51:25	17.50±1.5	33.30±1.3	25.15±2.05	35.767	-120.249	5.96	1.40
24	2010-11-17 10:57:55	8.95±0.65	39.95±1.55	24.45±2.05	35.672	-120.272	3.07	-1.05
25	2010-11-24 11:26:15	15.60±1.5	16.50±0.4	9.85±2.45	35.871	-120.386	3.00	-15.90
26	2010-12-01 12:36:10	9.65±4.25	42.80±2.8	20.60±6.3	35.657	-120.246	1.38	-5.90
27	2010-12-01 12:39:15	11.70±4	38.85±2.85	22.45±4.85	35.696	-120.257	3.93	-4.05
28	2010-12-28 14:46:35	12.30±1.1	40.90±0.5	23.70±2.9	35.685	-120.237	2.78	0.45
29	2010-12-28 22:27:55	9.35±1.25	42.55±2.25	17.75±5.05	35.657	-120.250	1.45	-5.50
30	2011-01-03 03:45:00	5.35±3.05	15.65±1.05	12.45±7.75	35.816	-120.478	5.63	-8.55
31	2011-01-23 19:41:20	9.25±1.65	43.35±1.15	21.80±0.8	35.651	-120.245	1.89	-4.70
32	2011-02-03 01:42:45	9.40±2.5	48.45±1.35	25.10±1.8	35.617	-120.207	2.19	-1.40
33	2011-03-12 07:41:25	11.45±2.85	44.95±4.95	21.00±6.3	35.653	-120.215	2.27	-5.50
34	2011-04-04 21:05:55	6.95±4.25	41.65±1.65	14.90±3.6	35.649	-120.277	4.22	-11.60

Table B.1.: Determined source location of LFE's based on the median error extent in the local grid coordinate system X,Y, and Z, and the corresponding latitude and longitude values. Additionally the difference to the source locations of Shelly and Hardebeck (2010) are given.

Acknowledgments

Foremost, I would like to express my sincere gratitude to Rebecca Harrington for giving me the possibility to write this thesis and her continuous support of my PhD study and research. She always had an open door to listen to my problems and was very patient especially with my writing in English. She supported me with her motivation, enthusiasm, and immense knowledge and her guidance helped me in all the time of research and writing of this thesis. I could not imagine having a better advisor and mentor for my PhD study.

I am deeply grateful to Friedemann Wenzel for supporting my work and to Thomas Bohlen for his suggestions to the modified TRI method. In this context I also want to thank Elisabeth Cochran for the continuous support, discussions, and her suggestions on various occasions.

A special thanks goes to Joachim Ritter and all the people within his working group. The ability to present and discuss new results was very helpful for me and giving trail presentation has improved my presentation skills thanks to their comment and advices. I will miss the weekly 'Schnitzel' at lunch.

I want to express my thanks to Andreas Köhler and Tobias Baumann for fruitful discussions on the SOM method, David Shelly for providing me reference source locations for LFE's, and Arthur F. McGarr for useful comments on the tremor detection manuscript.

I also want to thank the working group of Thomas Bohlen for discussions on the modified TRI method and in particular Simone who provided me help with the FD code. Moreover, I am thankful for all other GPI institute members supporting me in administrative and technical questions.

Further thanks go to Christian, Johannes, Toni and Michael for joining me playing dart during breaks. They were pleasant opponents by letting me win from time to time. Furthermore, it was a pleasure for me sharing the room with Friederike and Johannes and going to lunch with Tobias, Corinna, Friederike, Johannes, Toni, Michael, Jens, and Michael, giving the distraction needed every now and then. I also want to thank Steffi and Katrin for their support and being patient with me, when work was keeping me late in the office.

Finally, I want to express my profound gratitude from my heart to my mother and sister for their love and continuous support.